Electromechanical Switches Fabricated by

Electrophoretic Deposition of Single Wall Carbon Nanotube Films

A Dissertation
SUBMITTED TO THE FACULTY OF
UNIVERSITY OF MINNESOTA
BY

Jun Young Lim

IN PARTIAL FULFILLMENT OF THE REQUIREMENTS
FOR THE DEGREE OF
DOCTOR OF PHILOSOPHY

Stephen A. Campbell, Adviser

August. 2015

Acknowledgements

I would like to thank to my advisor Professor Stephen A. Campbell, for supporting me while pursuing my PhD. He provided me with insightful discussions and extensive guidance about the research. I also appreciate his encouragement and assistance during the past five years.

I also want to thank Prof. Stadler, Prof. Talghader, and Prof. Siegel, for being members of my defense committee and reviewing the dissertation. I highly appreciate their feedback and discussion.

I thank all of my group members, Liyuan Zhang, Brian Benton, Mandip J. Sibakoti, Sehyun Hwang, Tim Bontrager, Dr. Min-Woo Jang, Dr. Maryam Jalali, Dr. Sang Ho Song, Dr. Sreejith Karthikeyan, Dr. Brijesh Kumar and Dr. Forest Johnson. With their friendship, help and insightful discussion, I enjoy my school life and research. Special regards goes to Min-Woo and Maryam who have supported me when I first joined the research group. They showed me how to perform fabrication and characterize devices. Also special thanks to Sang Ho who gave me extensive assistant including many ideas in my research area.

I would also like to thank to all of MNC and CHARFAC staff for their assistance and kindness for my research over the past few years. I could not fabricate and characterize the device for the project without their assistance.

Finally, I am grateful to my parents, wife, and son. My parents have provided me with unconditional love and care. My wife and son have been a great support and have shown love and faith in me. With their support, I could completely focus on my study and research.

Dedication

I dedicate this dissertation to my wife, son, daughter, and parents.

Abstract

Power dissipation is a critical problem of CMOS devices especially for mobile applications. Many efforts have been made to solve the problem, but there are still major issues associated with scaling the device size. Micro electromechanical (MEMS) and nano electromechanical (NEMS) devices are one candidate to solve the problems because of their excellent standby leakage. However, the switches have a tradeoff between low operating power and high device speed. Suspended beams with low mass density and good mechanical properties provide a way to optimize the device.

Carbon nanotubes (CNTs) have the low mass density and excellent mechanical properties to enable high performance MEMS/NEMS devices. However, the high temperature required for the direct synthesis for CNTs makes it difficult for them to be compatible with a substrate containing transistors. Therefore, continuous film deposition techniques are investigated with low temperature (< 300 °C).

Electrophoretic deposition (EPD) is a simple and versatile processing method to deposit carbon nanotubes on the substrate at room temperature. The movement of the charged CNTs in suspension occurs by an applied electric field. The deposited CNT film thickness can be controlled through the applied voltage and process time. We demonstrate the use of an EPD process to deposit various thicknesses of CNT films. Film thicknesses are studied as a function of, deposition time, electric field strength, and suspension concentration. The deposition mechanism of the EPD process for carbon nanotube layers was explained with experimental data. We determined the film mass density and electrical/optical properties of SWCNT films. Rutherford backscattering

spectroscopy was used to determine the film mass density. Films created in this manner had a mass density that varies with thickness from 0.12 to 0.54 g/cm^3 and a resistivity of 2.14×10^{-3} Ω·cm. For the mechanical property measurements, we describe a technique to fabricate free-standing thin films using modified Langmuir-Blodgett method. Then we extracted the Young's modulus of the film from the load-displacement data from nanoindentation using the appropriate modeling. The Young's modulus had a range of 4.72 to 5.67 GPa, independent of deposited thickness.

We fabricated two-terminal fixed beam switches with SWCNT thin films using the EPD process. Device pull-in voltages under 1V were achieved by decreasing the air-gap. The pull-in voltages were compared with the calculated results using the device geometry and extracted Young's modulus from nanoindentation. Generally good agreement was observed. Also, we found a range of 2.4 to 3.5 MHz resonant frequency. However, we encountered several problems with the device including a gradual turn-on, hysteresis between pull-in and pull-out voltage, changes in the pull-in voltages with repeated on-off cycling, and early failure due to moisture absorption during testing in the air. Mechanisms for these observations are postulated. Further work is needed to improve device performance and reliability.

Table of Contents

List of Tables

List of Figures

Chapter 1.

Introduction

1.1. Overview

This Chapter first introduces the motivation for electromechanical devices. Then, the operation and problems of micro electromechanical system (MEMS) devices are discussed. As a possible candidate to solve the problem of MEMS, carbon nanotubes (CNTs) can be used for structural materials in the MEMS/NEMS devices due to their remarkable properties. Next, fundamental aspects of CNTs including synthesis, characteristics and thin film formation are described. Finally, we outline the following Chapters.

1.2. Motivation

1.2.1. Power dissipation problem in CMOS

While scaling down the device size, power dissipation becomes the primary issue of the CMOS device, especially for the mobile applications, devices must have very low power consumption. Power dissipation of CMOS devices can be categorized into dynamic and standby. Dynamic power dissipation is primarily due to the charging and discharging the capacitance during switch operation of CMOS devices. The standby dissipation is caused by junction, gate and subthreshold leakage. Figure 1 (a) depicts the

power consumption as a function of time. When gate length or device geometry is reduced, both types of power consumption increase. However, standby power dissipation is increasing much faster than dynamic power dissipation. Thus, the off-state power consumption becomes the most critical problem for sub-50 nm devices.

Much research has been done to find a solution to these power consumption problems. Gate leakage, one of standby leakages, is mitigated through the use of high-k oxide and metal gate [18]. Also, recently commercialized FinFET devices which have substrate leakage and gate leakage can reduce power consumption by lower the drain induced barrier lowering (DIBL) effect which threshold voltage decreases with increasing drain voltage for the short channel device and the subthreshold slope [19, 20]. However, because these devices are still field effect transistors, power dissipation problems that are inherent to the device remain unaddressed. Thus, devices with new operational concepts are required to solve the power dissipation problem.

Micro electromechanical (MEMS) or nano electromechanical (NEMS) devices can be one of candidates to solve the power dissipation problem because of their almost zero standby leakage in the off-state. MEMS/NEMS devices can be compatible with the conventional CMOS fabrication process technology. The active power dissipation of MEMS/NEMS is expressed by [21]

$$\mathrm{P} = \frac{1}{2} C V_P^2 f_s \tag{1.1}$$

where V_P is the pull-in voltage and f_S is the switching rate. Since the dynamic power consumption on the square of the operating voltage, low voltage operation is required. In addition, Equation 1.1 only considers an abrupt turn on condition. Power leakage also

occurs when the turn-on is gradual as shown in Figure 1(b). Therefore, a rapid transition is also required to reduce power leakage.

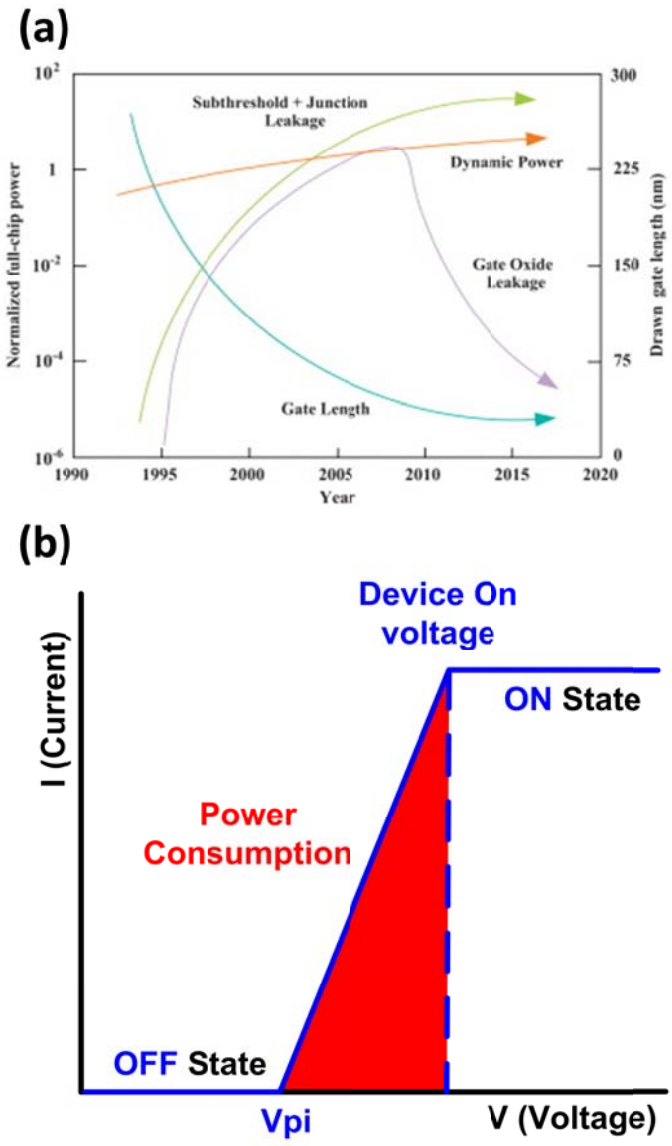

Figure 1.1 (a) Power dissipation as a function of time; Reproduced from [9] (b) Power consumption with gradual turn-on device

In summary, MEMS devices are a candidate to solve the power dissipation problem of CMOS devices, because they have very low (almost zero) standby leakage. Moreover, active and transition power consumptions can be reduced when MEMS devices operate with low power and as abrupt turn-on switch.

1.2.2. Operation principle of MEMS actuator

The electromechanical actuators are operated due to a potential difference between a free-standing movable beam and bottom electrode. The potential gap induces an external electrostatic force. There are two types of forces between free-standing beam and the electrode: attractive and repulsive forces. When attractive forces overcome the repulsive forces, the suspended beam moves down to contact the bottom electrode. When repulsive forces exceed attractive forces, the movable beam moves back to the original position. Ideally this condition occurs when the applied voltage difference is removed.

The device is on-state when both electrodes contacts together and current flows from one electrode to another. In the off-state, no current flow between two electrodes due to the gap. Thus, MEMS switches can be almost zero leakage as required for applications with low power consumption.

The required attractive force which changes the device status from ‘off’ to ‘on’ is supplied by providing a potential in excess of the pull-in voltage (V_{PI}). The pull-in voltage is affected by contact area, beam geometry, Young’s modulus of movable beam, gap between the electrodes, electrode surface roughness and the species of interacting atoms, etc [22]. In contrast, the pull-out voltage (V_{PO}) is defined when beam returns back

to original position upon reducing the applied voltage. Figure 1.2 shows the off-state and on-state of device by force variation. In general, $V_{PI} > V_{PO}$. This is due to the difference in the dependence of distance for the various forces. Some of the attractive forces are short-range in nature and so only effective when the beam in near the point of contact. In the extreme case the suspended beam contacts the electrode surface and does not return back again, even after the applied voltage is zero. In that case one can say that $V_{PO} < 0$, but the nature of the electrostatic attraction makes it independent of sign. This effect, called, stiction, renders the device unusable. Usually, low beam stiffness and large contact area cause stiction. To avoid this problem, high Young's Modulus materials are needed, however that creates a high pull-in voltage.

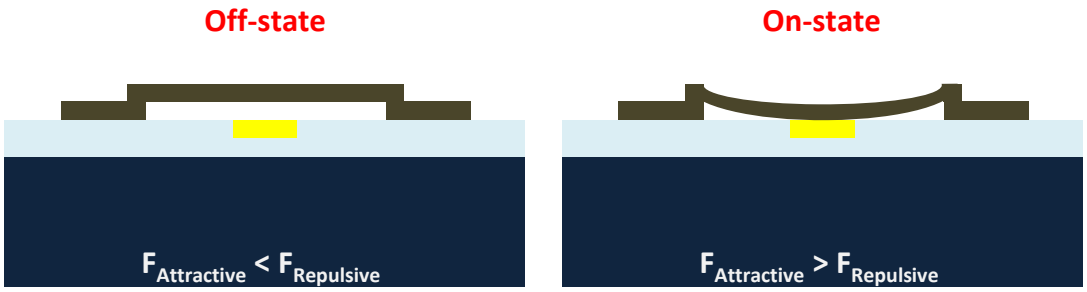

Figure 1.2 (a) MEMS switch for operation

1.2.3 MEMS device tradeoff between speed and low actuation voltage

In general, the pull-in voltage and switching speed of MEMS/NEMS switches have a proportional relationship to each other. The Pull in voltage of an electrostatic MEMS cantilever is expressed as [2]

$$V_{PI} = \sqrt{\frac{128}{27}\frac{\mathrm{E}t^3}{\varepsilon_o W l^3}(g_o)^3} \tag{1.2}$$

where E is Young's Modulus, t is the thickness of the beam, W is the contact width, l is the beam length, and g_o is the air gap between beam and bottom electrode. In addition, the switching speed of device is proportional to the resonance frequency [2]

$$f_o = 1.0279\left(\frac{t}{l^2}\right)\sqrt{\frac{E}{\rho}} \tag{1.3}$$

where ρ is mass density of the movable beam.

The above two equations have a common term, $t\sqrt{\frac{E}{l^3}}$, which creates a tradeoff between switching speed and actuation voltage. Thus, it is difficult to make high speed and low actuation voltage simultaneously. The equations have some independent parameters: the air-gap distance and the beam material thickness and density. This means that small air-gap and a thin, low mass density material are needed to make a fast switching speed and low operating voltage device.

1.3. Carbon nanotubes

Since Iijima firstly reported the carbon nanotubes (CNTs) [23, 24], substantial research into their use in many applications has been pursued because of their unique intrinsic properties [25]. A carbon nanotube which has a honeycomb structure can be described as sheets of graphene rolled into the cylinder. The CNTs can be divided into single walled CNTs (SWCNTs) and multi walled CNTs (MWCNTs) according to the number of layers of graphene in the roll. The SWCNT can be described by a vector,

known as the chiral vector, $\vec{C} = m\vec{a_1} + n\vec{a_2}$ where (m, n) and $(\vec{a_1}, \vec{a_2})$ are a pair of integer numbers and the 2D unit vectors, respectively. SWCNT are categorized into three classes according to the arrangement of carbon atoms around the nanotube diameter: armchair (m=n), zigzag (m=0 or n=0) and chiral SWCNT. SWCNTs have metallic behavior when the difference of m and n is a multiple of three (*m-n=3k* where k is nonzero integer). Otherwise, SWCNTs will have semiconducting properties. Typically, SWCNTs are 1 to 2 nm in diameter and few micrometers of length depending on the growth conditions.

1.3.1. Direct growth techniques

There are three methods to synthesize the carbon nanotubes by direct growth techniques: arc discharge, laser ablation and chemical vapor deposition (CVD) [25]. For CNT synthesis, these techniques need a catalyst, carbon source and energy [26]. In the first, the arc discharge technique, CNTs are synthesized by plasma discharge between two electrodes in an inert gas chamber [27, 28]. The second, laser ablation, uses a high power laser beam incident on a graphite target to vaporize the carbon and condense carbon at a water cooled collector as CNTs [29]. These two techniques produce high quality CNTs using solid-state carbon precursors and large amount of energy. The third technique, CVD, uses hydrocarbon gas and a metal catalyst as seed layer in a furnace held at ~900 ^{o}C [30]. After synthesis of CNTs, purification steps and post-synthesis treatments are required to remove the unwanted impurities [31, 32].

The ideal CNTs with direct growth techniques have excellent mechanical and electrical properties including low mass density (1.4 g/cm^3), a large Young's modulus (1 to 2 TPa), a tensile strength over 60 GPa [33, 34], a mobility up to 100,000 cm^2/V-sec at room temperature [35], and a current-carrying capacity of over 10^{10} A/cm^2 [36]. These remarkable characteristics of CNTs lead them to use in a variety of applications such as composite material [37-40], films [41, 42], microelectronics [43-49], energy storage [50-53], environment [54-56], and biotechnology [57-61].

1.3.2. Thin film deposition techniques using CNTs

The direct growth methods present several obstacles to compatibility with many substrates such as high growth temperature (> 900 ^{o}C). Also, they require post treatment steps which include acid treatment to remove metallic/carbon impurities and the annealing process to purify the raw materials. These limitations can be mitigated by forming a thin CNT film using a solution-based process at room temperature. The solution based film deposition methods have several advantages compared with direct synthesis: conventional silicon and polymer substrate compatibility and the use of standard lithography and etch processes to produce arbitrary patterns at any location on wafer.

The CNT film deposition methods with solution base can be divided into drop/spin coating [62-66], spraying [67], dip coating [68], roll-to-roll [69], layer-by-layer (LbL) [70] and electrophoretic deposition (EPD) [71, 72]. For the drop casting and spin coating techniques, a small amount of dispersed CNT suspension is dropped on the

substrate, then the substrate is allowed to dry in air (drop casting [62-64]) or it is rotated at high speed (spin coating [65, 66]). Drop casting is the easiest techniques to coat the substrate, and spin coating is good for thinner depositions. However, it is difficult to make a dense film with these methods.

In spray coating [67] the CNT suspension is directly sprayed onto a heated substrate using commercial air brush pistol. Even though the heating temperature is selected to accelerate the drying of the droplets, it is still difficult to avoid agglomeration.

In the dip coating method [68] the substrate is immersed into the dispersed CNT suspension and placed to dry in air. It is frequently used to fabricate transparent and conductive films on various substrates. However, both sides of substrate can be coated with this method.

In the roll-to roll process [69] a controlled amount of dispersed CNT solution is coated on a substrate by a coating rod. For drying the deposited film, a heated bar is used. This method is used in industry and is good for extremely large areas. However, position to position control of thickness is still challenging.

The layer-by-layer method uses altering layers of positively charged and negatively charged CNTs [70, 73]. The substrate is repetitively immersed into the prepared oppositely charged suspension sequentially. The deposited mass can be controlled by the number of immersions. Our group previously demonstrated layer by layer processes to deposit film with randomly distributed or aligned SWCNTs [74]. However, this technique has several problems. The LBL method is extremely slow,

typically 4 to 8 hours to deposit a 100 nm thick film. Moreover, the positively charged CNT suspensions are extremely difficult to control and reproduce.

Lastly, EPD technique uses the movement of negatively charged CNTs dispersed in a suspension under an applied electric field [71, 72, 75]. The deposited mass is controlled by the applied voltage and process time [76]. We chose the EPD method to deposit the SWCNT films for this project. We will explain the electrophoretically deposited SWCNT film in Chapter 2 in detail.

1.4. Research goal

The research endeavors to develop the technology needed to ultimately fabricate low pull in voltage (under 1V) and high frequency (over 1GHz) NEMS device using SWCNT films. The research is divided to three steps: SWCNT film deposition with EPD, SWCNT film characterization, and device fabrication. The SWCNT film deposition is demonstrated using electrophoretic deposition process. This is a much faster and simpler process than the difficult to control LBL process used previously. We suggest the CNT deposition mechanism on substrate and control factors to keep the same thickness films. Next, electrophoretically deposited SWCNT films are characterized to find film properties including density, electrical, optical and mechanical properties. Finally, two terminal switches are fabricated with various air gaps to decrease the operating voltage. Then, the produced devices are characterized with HP4156 to measure the pull-in voltage.

1.5. Literature review: Previous MEMS devices using CNTs

In the literature, many studies have reported MEMS/NEMS switches using carbon nanotubes. Some of these used single CNTs either deposited randomly or placed by hand. Rueckes *eq*. developed electromechanical On/Off switch using a 50 nm thick nanotube rope [6]. The device consisted of upper and lower nanotubes on the SiO_2/Si substrate as shown in Figure 1.3 (a). The device switches from 'off' to 'on' state at 2.5V as illustrated in Figure 1.3(b). Lee *et al.* implemented three-terminal nanorelay with a multi walled carbon nanotube [7]. Figure 1.4 depicts the fabricated device and I-V characteristics of device. The operating voltage starts from 3V depending on the gap. Cha *et al*.

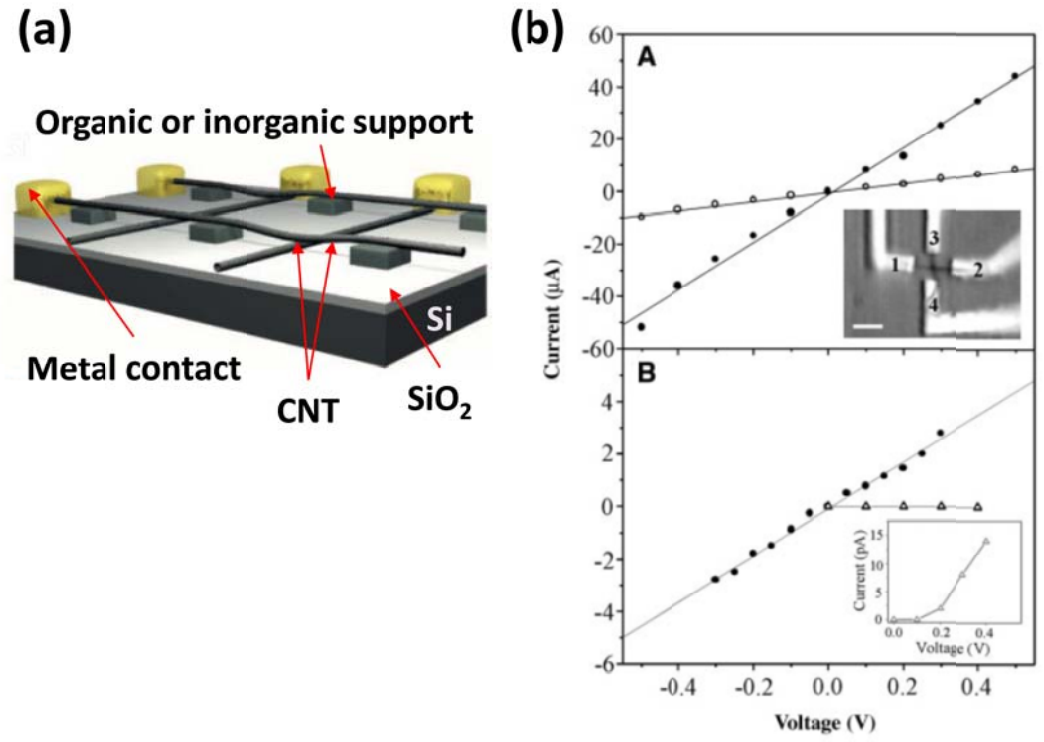

Figure 1.3 (a) Schematic of a suspended crossbar array (b) I-V characteristic of device: A. I-V curve of upper and lower CNT B. I-V curve of 'on' and 'off' state; Reproduced form [6]

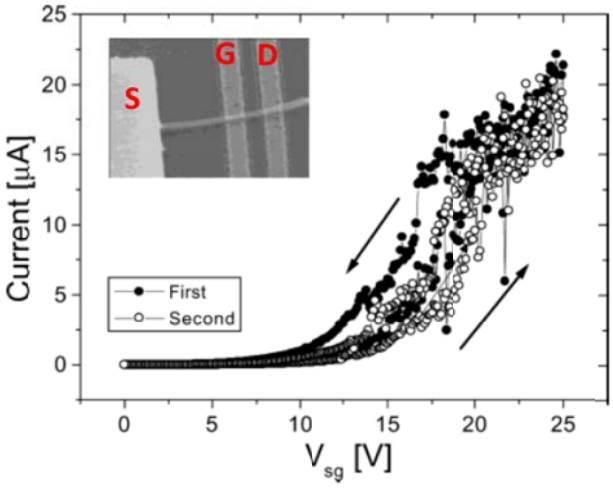

Figure 1.4 I-V characteristic of nanotube relay initially suspended almost 80nm from source and drain region; Reproduced from [7]

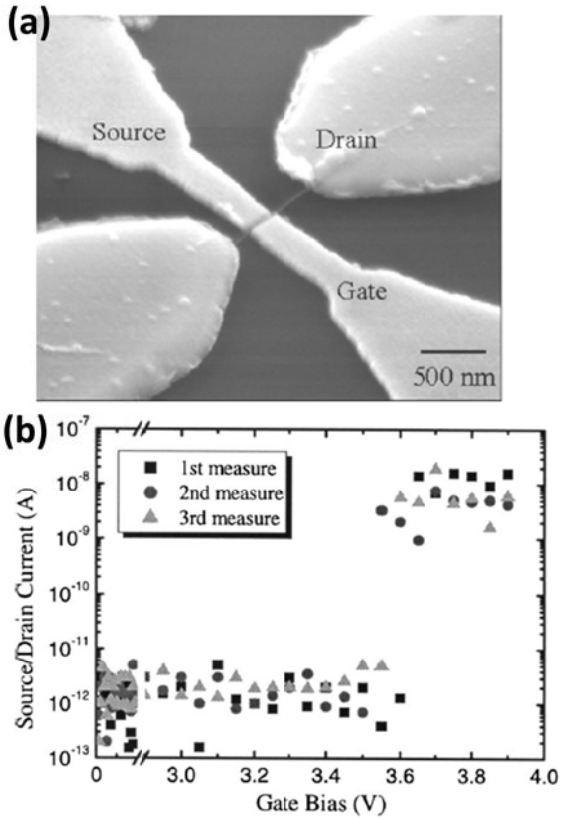

Figure 1.5 (a) SEM image of fabricated device (b) I-V characteristic of the device; Reproduced from [13]

demonstrated a nanoelectromechanical switch using a suspended carbon nanotube as shown in Figure 1.5(a) [13]. Figure 1.5 (b) illustrates the I-V curve of fabricated device, and the pull-in voltage of device 3.6 to 3.8 V. Kaul *et al.* implemented two terminal switch with laterally grown single walled carbon nanotubes as shown in Figure 1.6 [5]. The device pull-in voltage is almost 2.5 V.

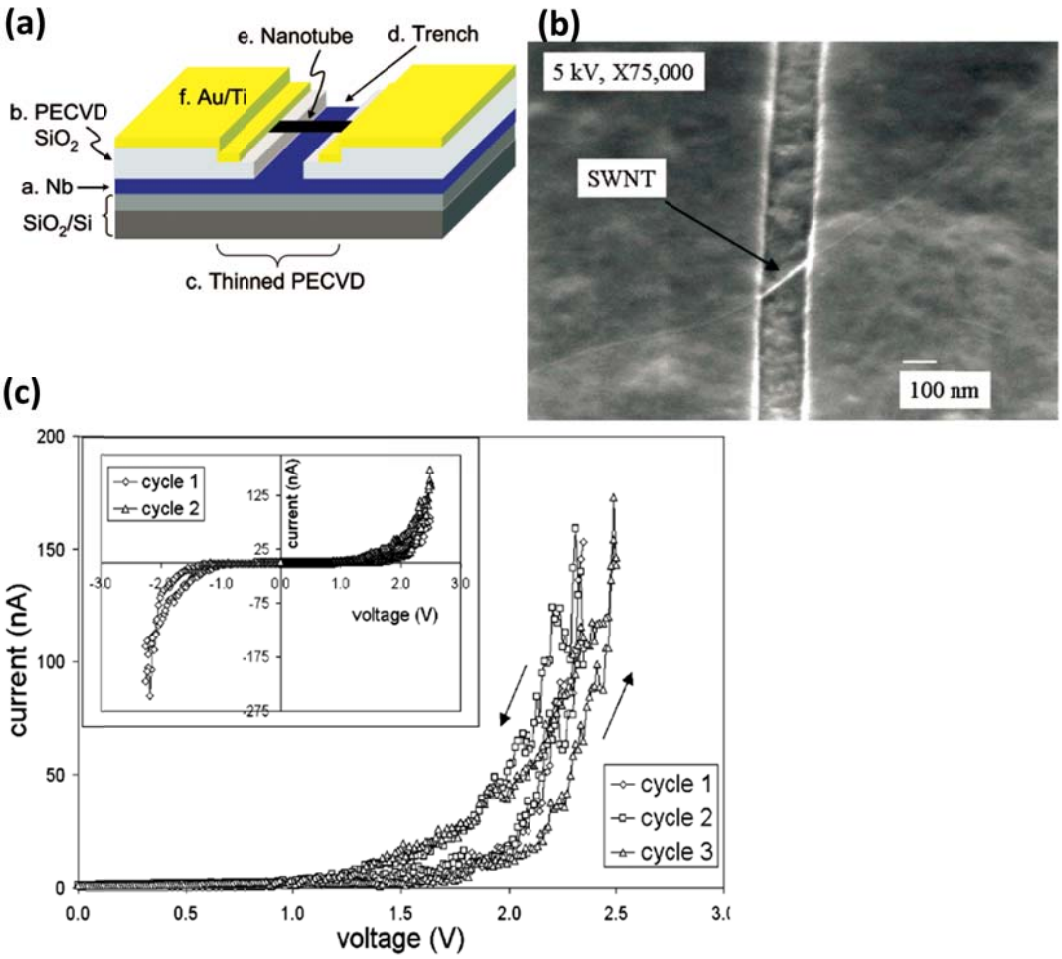

Figure 1.6 (a) Schematic of 2-terminal switch using SWCNT which is grown from patterned Fe in a CVD furnace (b) SEM image of produced device (c) I-V characteristic of device; Reproduced from [5]

The second category of devices, pioneered by our group, used films comprised primarily of CNTs. These films were patterned lithographically. Jang *et al.* demonstrated 3 terminal NEMS switches using single-walled carbon nanotube (SWCNT) with layer-by-layer deposition method (shown in Figure 1.7) [15]. The device was operating when two gates have enough voltage to attract the cantilever like a NAND device.

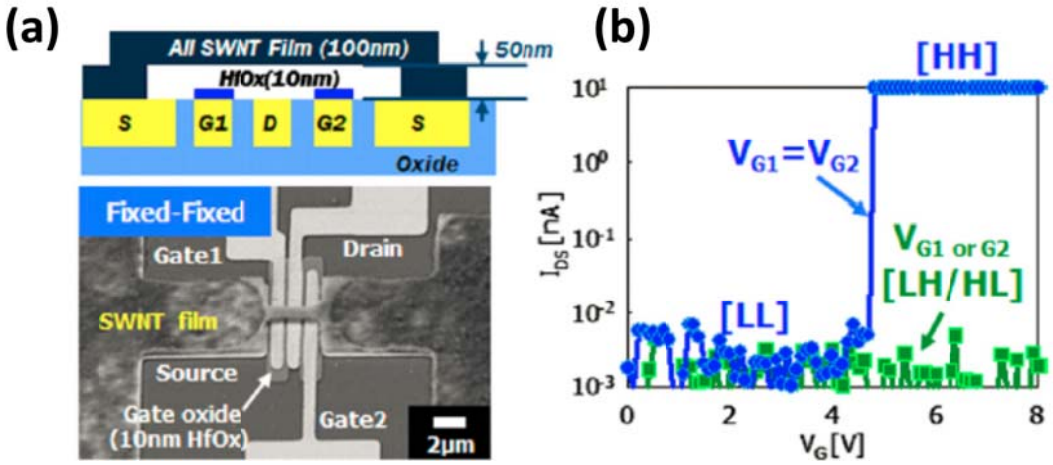

Figure 1.7 (a) Schematic and SEM image of 3-terminal NEMS switch (b) I-V characteristics of the device. Devices have high output when two inputs are high like NAND devices; Reproduced from [15]

1.6. Thesis overview

CMOS devices have severe power dissipation problems, especially during the off-state. MEMS/NEMS can become a candidate to solve the power consumption problem due to their excellent standby leakage. However, MEMS/NEMS switch have intrinsic problems to satisfy both the high frequency and low operating voltage. Thus, it is required to use materials which have low mass density and high mechanical properties

for suspended beam. Chapter 2 reviews the fundamentals of electrophoretic deposition of carbon nanotube films, and explains the deposition kinetics with the experimental result of EPD process. Chapter 3 demonstrates the characteristics of the SWCNT films: density, electrical, optical and mechanical properties. Moreover, modeling is introduced with fabrication techniques for very thin films. Chapter 4 describes the fabrication process and characteristics of the MEMS/NEMS switch using electrophoretically deposited SWCNT films. Chapter 5 summarizes the research results and provides recommendations for the future research.

Chapter 2.

Electrophoretic Deposition of Single Wall Carbon Nanotube Films

2.1. Overview

This chapter begins with a discussion of the theoretical explanations for the mechanism of electrophoretic deposition (EPD) when it is used to form thin carbon nanotube (CNT) films. Also, the role of surfactant in suspension for EPD process is described. Then, the CNT film deposition process is introduced with the preparation of single wall CNT (SWCNT) suspension. The deposited film thickness is measured as a function of time, applied electric field and suspension concentration. Through the experimental result, the SWCNT film deposition mechanism in an EPD process is examined. Finally, the fabrication method which can be extended to flexible device or MEMS/NEMS device is developed by removing the metal seed layer and a sacrificial layer under the SWCNT film.

2.2. Theoretical review of stable suspension and electrophoretic deposition

EPD is a simple coating technique based on electrodeposition [77]. Traditionally, EPD has been employed in ceramic and composite material coatings [78]. Recently, EPD has been used in several processing areas: nanoparticle deposition, thin film, textile structures and bio materials [72, 79]. EPD processing has many advantages: high

versatility with a wide range of substrate and materials, cost effectiveness, simple processing equipment, high deposition rate, large area coating, complex shape deposition and nanostructure fabrication. The deposited amount of materials can be precisely controlled by the processing parameters. These benefits lead to use of EPD processing in a wide range of applications such as MEMS/NEMS devices, optical devices, biomaterials, fuel cells, flexible electronics and printable/nano electronic devices.

A stable suspension is required for EPD process to prevent particles aggregation before deposition. An explanation of the stable suspension preparation for EPD and fundamental concepts and deposition mechanisms of EPD would be explained in the next few sections.

2.2.1. Preparing a stable suspension

2.2.1.1. Fundamental of colloidal stability in suspension

Particles in suspension can readily agglomerate before reaching the electrode where they deposit to form a thin film. Thus, a stable suspension (i.e. one with a very long agglomeration time) is essential for an effective EPD process. In colloidal chemistry the stability of a suspension is determined by the zeta potential (ξ), the potential difference between the suspension and stationary layer of fluid attached to the dispersed particle. Particles with a high zeta potential produce a repulsive force that impedes particle agglomeration in suspension. Particles with low zeta potential, however, tend to aggregate each other to form precipitates. Therefore, one route to a stable suspension is to generate particles with a high zeta potential.

In considering a charged particle in suspension, one must also take into account the response of the solution to the field. There is a net charge near the particle surface in a suspension when charged particles exist in liquid solution. Figure 2.1 describes the electrical double layer (EDL) and potential variance. The charged particle in the suspension is enclosed with the oppositely charged ions. Therefore, the EDL is divided by two distinguishable regions: inner region and outer region. The inner region (Stern layer) is the packed counter ion region near the charged particle. The outer region (diffuse layer), where both negatively and positively charged ions exist, has a lower density of ions than the inner layer.

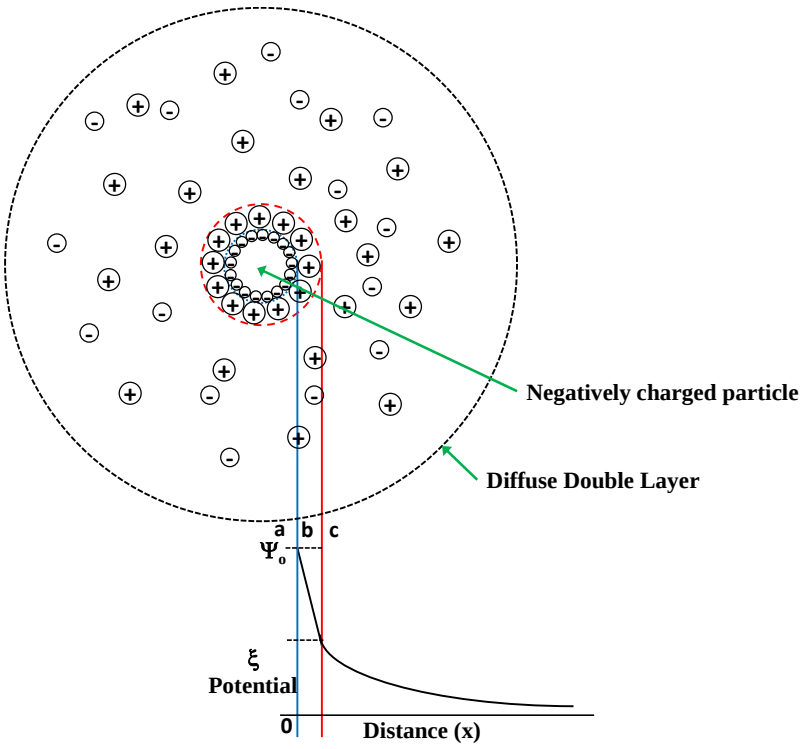

Figure 2.1 Schematic of the electrical double-layer and potential drop from surface of charged particle to outer layer: (a) charged particle (b) stern layer (c) diffuse layer

One of the most significant steps for EPD process is preparing a stable suspension where particles are well dispersed in the liquid medium during processing and move towards the electrode without disruption from the other particles. Particles can agglomerate during the processing when attractive van der Waals force overcomes the repulsive electrostatic force. They could also be deposited on the electrode substrate under an applied electric field.

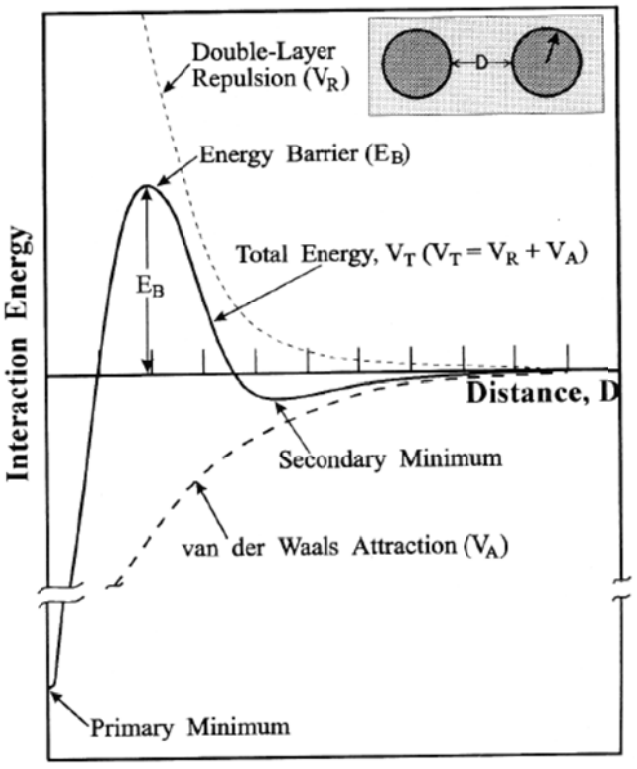

Figure 2.2 Schematic of the interaction energy between two particles in suspension based on DLVO theory; Reproduced from [4]

Derjaguin and Landau and Verwey and Overbeek developed the DLVO theory which explains the interaction between particles in a liquid [79-82]. The DLVO theory explains the interaction energy as a function of distance between two particles with attraction energy (Van der Waals attraction, V_A) and double layer repulsion (V_R). The total interaction energy ($V_T = V_A + V_R$) is shown in Figure 2.2. The inter-particle gap is almost zero near the primary minimum in the interaction energy curve. The repulsion energy plays a dominant role for particle interaction by increasing the distance of particles. The dominant attractive energy near the secondary minimum produces a suspension of particles bound together by a weak, net attractive energy.

2.2.1.2. Fundamental concepts for stable solution

Increasing the repulsive force between particles is necessary to prevent particle agglomeration because of the dominant Van der Waals force between the particles. There are two fundamental concepts to stabilize the suspension: electrostatic stabilization and polymeric stabilization.

Electrostatic stabilization can be achieved by introducing repulsive charged ionic group in the suspension. The particles are surrounded by oppositely charged ions to form electrical double layers. The thickness of double layer is determined by the ionic strength which depends on the molar concentration and charge of ion in the dispersed suspension. Polymeric stabilization uses the surfactant to increase the mutual force of repulsion to stabilize the suspension. A hydrophobic tail of surfactant is adsorbed on the hydrophobic surface of particle, while the ionized hydrophilic head react with water. Then, the

dispersed particles have mutual force of repulsion with each other to prevent agglomeration due to the surrounding surfactant. Figure 2.3 shows three possible adsorption types between dispersed CNTs and surfactant in suspension.

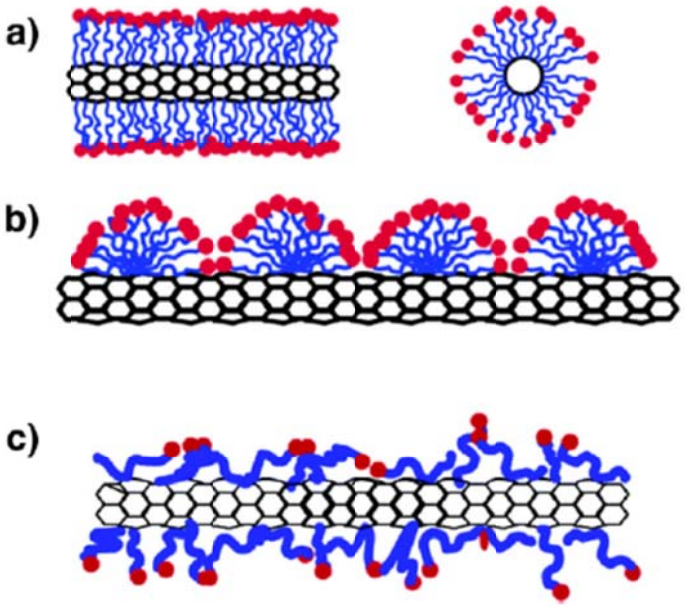

Figure 2.3 Schematic of polymeric stabilization of carbon nanotube (a) Cylindrical adsorption of surfactant (b) hemi-micellar adsorption of surfactant (c) random adsorption of surfactant; Reproduced from [10]

2.2.2. Fundamental concept of EPD

EPD consists of two steps: electrophoresis and deposition [71]. During the electrophoresis step, charged particles in an aqueous solution are attracted to the oppositely charged electrode under an externally applied electric field. In the next deposition step, particles accumulate near the electrode surface and form a film [72].

EPD can be classified into cathodic and anodic EPD depending on the charge of particles in suspension. In the cathodic EPD, positively charged particles in an aqueous solution move to the negatively charged electrode. In the anodic EPD, however, negatively charged particles are attracted to the positively charged anode. Figure 2.4 depicts the deposition process.

Each step of EPD process is concerned with proper theories. Firstly, the kinetics of electrophoresis process will be discussed followed by the description of the deposition mechanism.

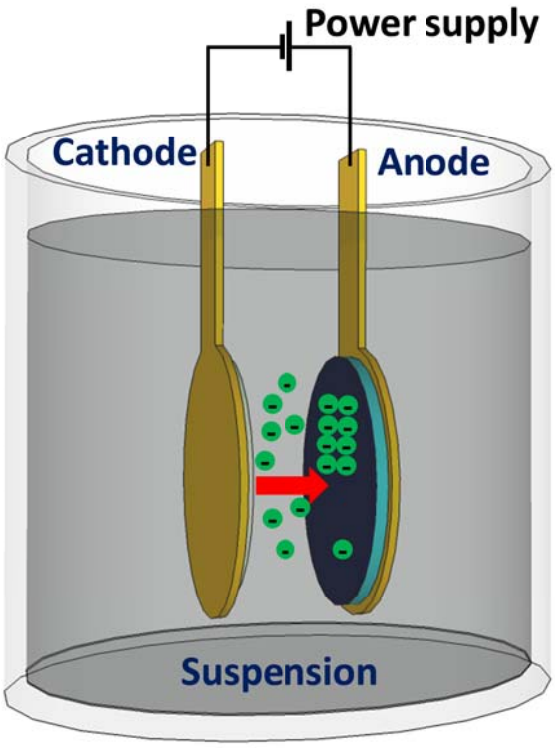

Figure 2.4 Schematic of EPD of negatively charged materials

2.2.2.1. Kinetic mechanism

The first kinetic mechanism of EPD was driven by Hamaker using by a simple mass conservation principle [76]. The deposited mass (m, g/cm^2) is expressed in below [76]:

$$\mathrm{m} = C_S \mu A E t \tag{2.1}$$

where C, μ, S, E, and t are concentration of particles in suspension (g/cm^3), electrophoretic mobility (cm^2/Vs), deposition area of electrode substrate (cm^2), field strength (V/m) and deposition time (s), respectively. While this simple equation is sometimes used to describe the process, it is not sufficient to explain a realistic EPD process due to the variation of suspension concentration and electric field during actual deposition processing.

Next, Sakar and Nicholson developed exponential empirical relation to solve the problems of the previous Harmaker's equation. In this empirical equation the deposited mass is expressed by [4]

$$m(t) = m_0(1 - e^{-kt}) \tag{2.2}$$

where m_0 and k are initial weight of the powder in suspension and kinetic parameter. The kinetic parameter is defined as k=*Afu/V* where *f*, *u* and *V* are efficiency factor, average velocity of the particles in suspension and the volume of the suspension which is considered to be a constant. The efficiency factor, which is equal to or less than unity, is the fraction of the particles near the electrode actually becoming incorporated into the film rather than agglomerated. Thus, if all particles take part in the deposition process, *f* = 1. Typically high efficient factors are found in colloidally stable suspension. Exponential

equation matched well with the Hamaker's equation for short time depositions because there is negligible concentration variation in the suspension. However for my typical processes, as the deposited mass increases the particle concentration in the suspension drops. In this condition, the applied electric field between electrodes drops (assuming high resistivity deposited films) due to the series resistance of the deposited layers, especially when using a constant voltage source.

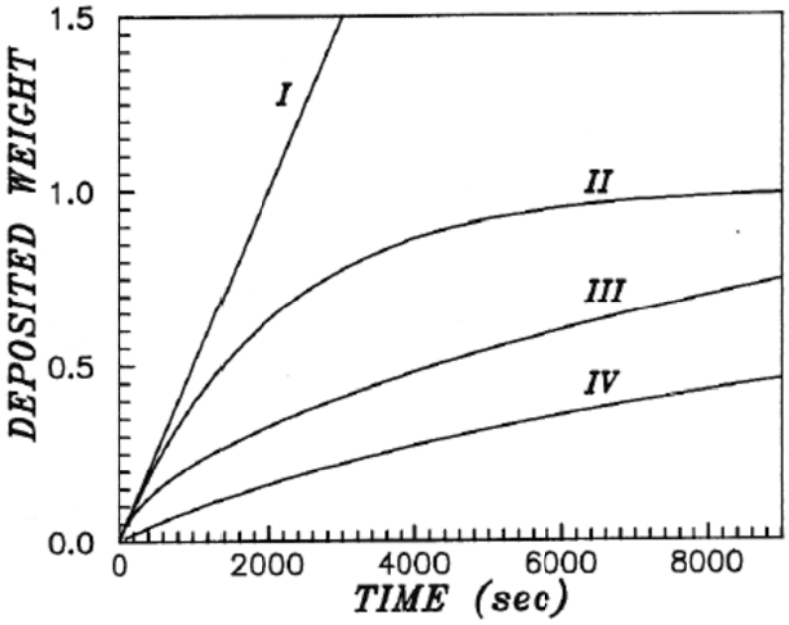

Figure 2.5 Schematic of the kinetic of EPD process with four conditions: (I) constant current/constant concentration (II) constant current/variable concentration (III) constant voltage/constant concentration (IV) constant voltage/variable concentration; Reproduced from [4]

Sakar and Nicholson categorized the mass deposited as a function of time for different process conditions: constant current, constant voltage, constant concentration

and variable concentration in the exponential equation. Figure 2.5 depict the schematic of categorized EPD process, and table 2.1 represents Figure 2.5 in more detail.

Table 2.1 Explanation of the kinetics of EPD process from Figure 2.5.

Category	Source	Concentration	Features
I	Current	Constant	Deposited mass varies linearly with time
II	Current	Variable	Deposited mass varies exponentially with time due to decrease in concentration
III	Voltage	Constant	Deposited mass varies exponentially with time due to increase in the electric resistance of the deposited layer.
IV	Voltage	Variable	Deposited mass varies exponentially with time due to decrease in concentration and increase in the electric resistance of the deposit layer.

2.2.2.2. Deposition mechanisms of EPD

The exact deposition mechanisms are still a matter of discussion in the literature, both in the particle arrangement and in the aggregation of particles on the electrode. The arrangement and aggregation of particles follow the surface chemistry and the particle self-interaction and the particle and electrode surface interaction. The deposition mechanisms can be categorized into four theories by the phenomenon of the particle accumulation: 1) Fluctuation by particle accumulation, 2) particle charge neutralization, 3) electrochemical particle coagulation, and 4) distortion and thinning of electrical double layer (EDL).

The first, and perhaps simplest, fluctuation mechanism by particle accumulation is proposed by Hamaker and Verwey [83]. They explained that the applied electric field

attracts the particles to the electrode and these incoming particles deposit on the electrode after overcoming the inter-particle repulsion.

The particle charge neutralization mechanism is suggested by Grillon *et al.* with powder deposition [84]. When particles come in contact with the substrate, they undergo charge neutralization and become static. This mechanism is feasible for monolayer deposition (initial stage deposition from the diluted suspension), however it is invalid with thick films especially if they are highly resistive or if the pH of the solution changes during the electrochemical reaction near the electrode.

The electrochemical particle coagulation mechanism was introduced by Koelmans[85]. They suggest that the increase of electrolyte concentration near depositing electrode lowers the zeta potential and induces flocculation of particles. The concentration change causes the reduction of the repulsive forces between particles on the substrate resulting in particle coagulation. This mechanism is valid for an electrode reaction which generates OH^-, for example, a suspension containing water. However, if the concentration of electrolytes in suspension is constant, the mechanism is invalid [77].

Finally, distortion and thinning of electrical double layer is suggested by Sakar and Nicholson as described in Figure 2.6. They explained the deposition mechanism with an oxide particle/lyosphere system. Firstly, the applied field causes a distortion of the double layer envelop, so positively charged particles move towards the negatively charged electrode. This leads to thinner heads on the side of the particle nearer the cathode and wider tails extending toward the anode. The head region keeps thinning after they contact the substrate. The incoming particles also have a thin leading double layer at

the head. Lastly, the double layer around the tail of the particles become sufficiently thin, so other attracted particles can approach close enough for the London Van der Waals attractive force to cause coagulation.

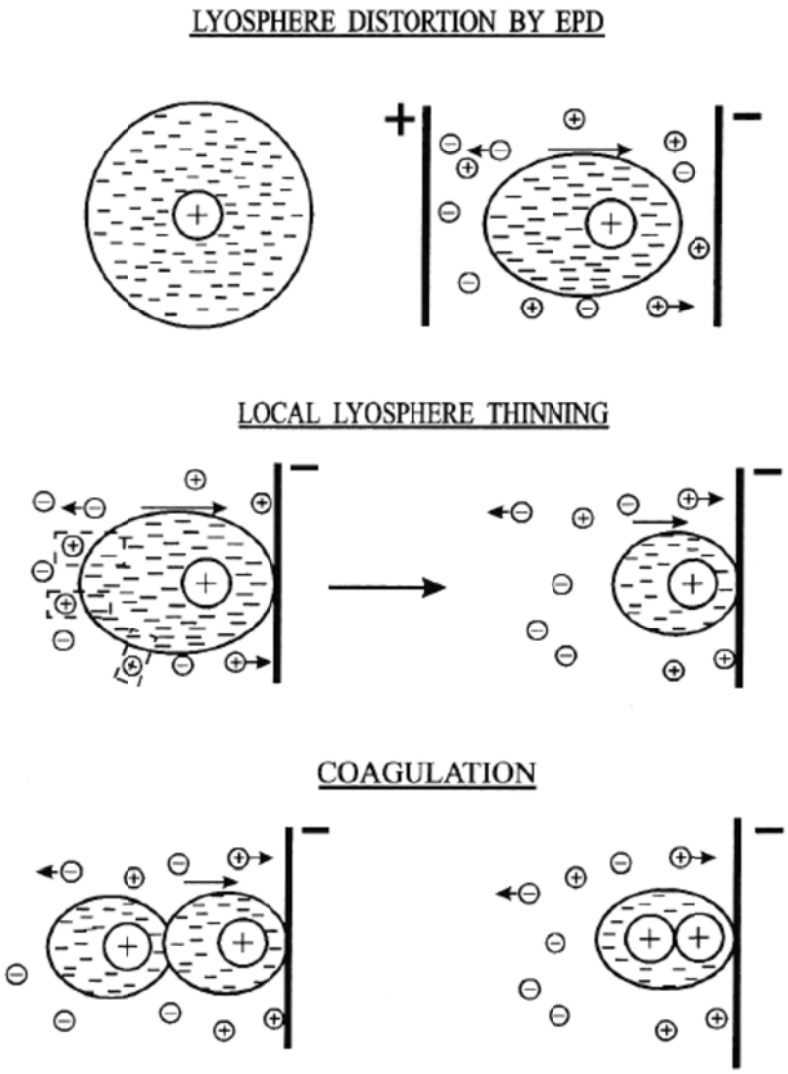

Figure 2.6 Schematic of deposition mechanism by distortion and thinning of electrical double layer (EDL); Reproduced from [4]

2.3. SWCNT film using electrophoretic deposition

Electrophoretic deposition is a simple and versatile processing technique for the production of thin carbon nanotube films [13]. EPD uses the movement of charged particles dispersed in suspension under an applied electric field [14]. EPD enables deposition of thin and thick films, as well as composite coatings with complex shapes and surface patterns [15]. Possible applications of CNT films include CNT reinforced composite films and structures, field emission devices, MEMS/NEMS switch, sensors [86], energy storage (fuel cell) [87], and photovoltaic devices [88].

Preparing a suspension which has a high zeta potential on the particles and low ionic conductivity is necessary for EPD deposition (Van der Biest and Vandeperre [79]). As-produced carbon nanotubes are intrinsically inert and contain various metal particles and carbon impurities [28, 89-91]. Also, they often agglomerate or entangle each other to make bundles. Therefore, purification process to remove residual metal and carbon impurities and dispersion the CNTs in solution are essential before preparing suspension for EPD. A typical strategy uses chemical oxidation and annealing to purify the raw material. A mixture of nitric acids (HNO_3) and sulphuric acids (H_2SO_4) are used for acid treatment process. These acids reduce the length of CNTs and introduce carboxylic groups (-COOH) on the surface as shown in Figure 2.7 [12]. These acidic groups make a negative surface charge in suspension and enable stable carbon nanotube suspension during EPD process due to electrostatic repulsion among the CNTs [92].

As mentioned before, a dispersion of CNTs in solution is a necessary precondition for preparing a stable suspension. Polymer based surfactants and ultra-sonication for hours can be used to debundle the CNTs by steric hindrance or electrostatic repulsion. A mechanism of isolation is depicted in Figure 2.8. CNTs initially form a bundle in suspension (Figure 2.8 (a)). Ultra-sonication forms a gap at the end of the bundle and the surfactants get adsorbed on the separated surfaces (Figure 2.8 (b)). Lastly, CNTs are separated from the bundle (Figure 2.8 (c)).

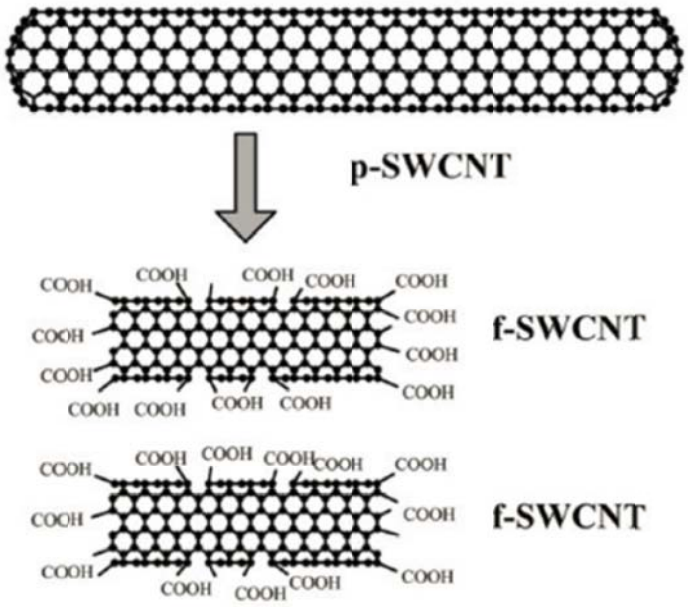

Figure 2.7 Schematic of a functionalization of pristine SWCNT by acid treatment; Reproduced from [12]

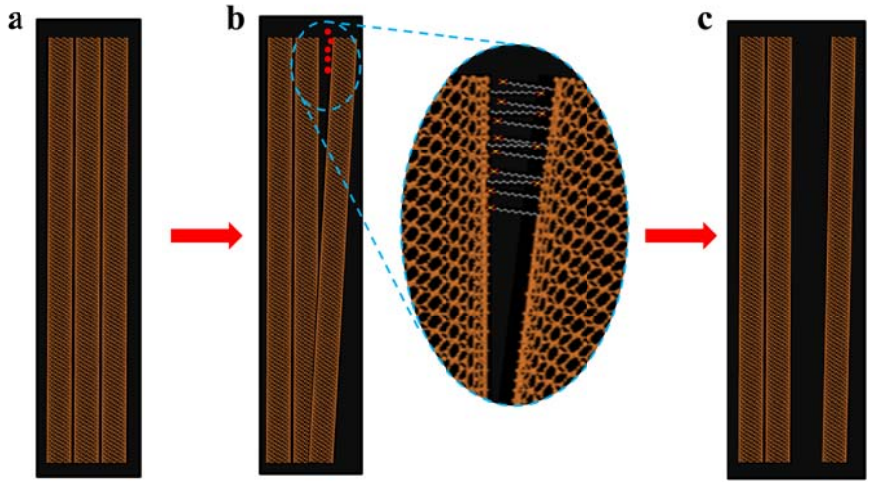

Figure 2.8 CNT dispersion mechanism using surfactant and ultrasonication (a) pristine CNT bundle in suspension (b) sonication and surfactant adsorption on the surface of CNTs (c) detached CNT from the bundle

Duan *et al*. report the dispersion of carbon nanotubes with a sodium dodecyl sulfate (SDS) surfactant using molecular mechanics (MM) simulation [11]. They implement a MM simulation with different concentrations of surfactant in suspension as shown in Figure 2.9. The binding energy tends to decreases with the increase of surfactant concentration in Figure 2.9 (e). Adsorbed SDS surfactants on the surface of CNT have different bond shapes according to the number of the SDS molecules. For low SDS surfactant concentrations, the surfactants are randomly adsorbed on the surface of CNT (Figure 2.9 (a)). The binding energy in this condition increases linearly with the number of surfactants. The adsorption morphology tends to follow a cylindrical micelle as shown in Figures 2.9 (b), (c), and (d), for increasing number of surfactant molecules. While the binding energy decreases with the increase of surfactant concentration in

region (b), it depends on the number of surfactant in region (c). The binding energy is constant over the certain SDS concentration.

Du *et al.* first applied this technique to CNTs, demonstrating the deposition of multi-walled CNTs (MWCNTs) using an ethanol/acetone suspension [93]. They showed higher packing density of CNTs from CNT/distilled water than from CNT/ethanol suspensions. Kim and Lee deposited SWCNTs on silica spheres using EPD processing [94]. Pei *et al.* studied similar films [95], but they presented a limited amount of material characterization. The characterization has focused primarily on the electrical and optical properties of these films. Cho *et al*. deposited MWCNT film on the stainless steel substrates and characterized the film [71]. They explained the kinetics of EPD including the effects of the applied electric field and deposition time. Jung *et al*. deposited aligned SWCNT film for field emission devices [96]. Roth *et al*. deposited 10nm thick carbon nanotube layers on borosilicate glass and PET substrates [97]. Rigueur *et al.* studied the mechanical properties of free-standing multi-walled carbon nanotube films using EPD techniques [98]. Boccaccini *et al.* reported a comprehensive study on electrophoretic deposition of carbon nanotubes as mentioned in Table 2.2 [72].

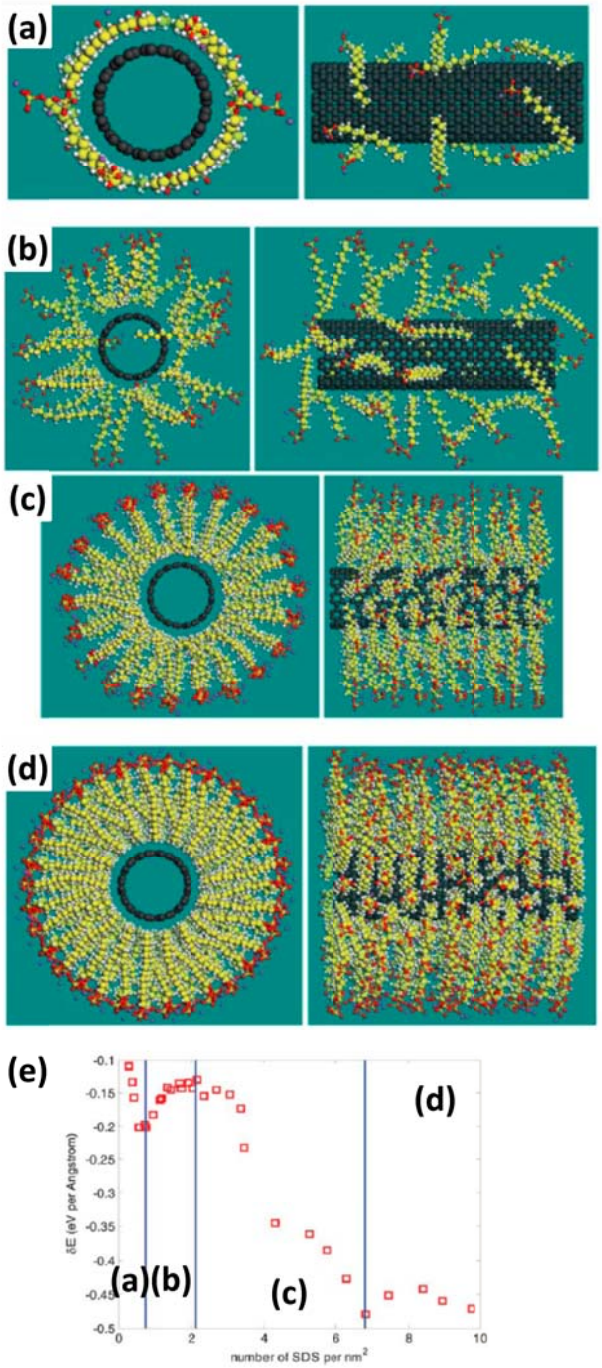

Figure 2.9 Aggregation morphologies of SDS surfactant on the surface of CNT. (a) 0.57 SDS surfactant per nm^2 (b) 1.67 SDS surfactant per nm^2 (c) 5.25 SDS surfactant per nm^2 (d) 9.73 SDS surfactant per nm^2 (e) Binding energy as a function of SDS concentration; Reproduced from [11]

Table 2.2 Overview of EPD parameters for CNTs deposition; Reproduced from [72]

Electrode properties	***EPD parameters***			***Ref***
	Constant voltage	***Deposition time***	***Electrodes gap***	
Stainless steel (1 × 1 × 0.2 cm^3)	*5–50 V*	*0.5–10 min*	*20 mm*	*[99]*
Aminopropoxysilane (APS) pretreated Optically Transparent Electrodes (OTEs)	*500 & 50 V*	*1 min & 2 min*	*6 mm*	*[100]*
Carbon Fibre paper Electrodes (CFE) (2.25 × 2.25 × 0.6 cm3)	*~ 40 V*		*5 mm*	*[101]*
Aluminium electrodes	*45 V*		*50 mm*	*[102]*
Metal electrodes	*45 V*		*50 mm*	*[93]*
Titanium (1 × 1 cm^2) electrodes				*[103]*
Cathode: Glass plate (1 cm × 0.5 cm) with ITO coating *Anode: Glass plate (1 cm × 0.5 cm) with aluminium coating*	*100–200 V*		*18, 11, 3, & 1 mm*	*[104]*
Silicon wafer (cathode) and stainless steel mesh as an anode	*30–600 V*		*20 mm*	*[105]*
Stainless steel mesh (cathode) and a gated triode structure formed on a glass substrate (anode)	*30–200 V*			*[106]*
Indium tin oxide (ITO) coated glass				*[107]*
Conducting glass electrodes, optically transparent electrode (OTE)	*100 V*		*5 mm*	*[108]*
Conducting glass electrodes, optically transparent electrode (OTE)	*<100 V & >100 V*	*2–3 min*	*5 mm*	*[109]*
Polyimide film coated with titanium (cathode) and stainless steel (anode)	*100 V*	*1–2 min*		*[110]*
Stainless steel	*20 V*		*10 mm*	*[111]*
Patterned metal substrates	*10–50 V*			*[112]*
Patterned dielectric substrate with 1 lm thick polysilane film coating	*2000 V/cm*	*A few min*		*[100]*
Nickel and stainless steel substrates or metal-plated glass plate	*200–300 V*	*2 min*	*20 mm*	*[42]*
Nickel substrates (10 × 10 mm^2) etched with 20% HNO_3 for 10min	*20 V*	*5 min*		*[113]*

2.3.1. Experimental Details[1]

Commercial SWCNTs with an average diameter of 1.4 nm (Carbon Solution Inc.) were used for EPD processing. We treated SWCNTs with nitric acid to remove impurities such as amorphous carbon and catalyst contamination [114]. SWCNTs at a concentration of 1 mg/ml were used in deionized (DI) water with 1 wt % of the sodium dodecyl sulfate (SDS) surfactant. Pristine SWCNTs form agglomerates in DI water due to their strong hydrophobic properties. Therefore, the preparation of a stable dispersion of SWCNTs in a liquid solution is a necessary prerequisite for using the EPD method. SDS, one of the most widely used surfactants, is used to promote a mutually repulsive force to stabilize the SWCNT dispersion [115]. The surfactant molecules consist of two parts: a hydrophobic tail and a hydrophilic head. While the ionized hydrophilic head reacts with water, the hydrophobic tail adsorbs physically on the hydrophobic surface of the SWCNT bundle. Then, the dispersed SWCNTs have negative surface charges in the DI water. These negative charges surrounding SWCNTs in suspension increase the repulsive double layer force to prevent SWCNT agglomeration [116, 117].

The mixture was sonicated for one hour. Then the solution was centrifuged at 3500 RPM for one hour to remove any precipitates or agglomerates. Figure 2.10 (a) shows the mixture procedure to prepare the SWCNT suspension. The upper 90% of the solution was separated for the deposition. Sonication and centrifugation was done prior to each deposition. The deposition was carried out in room temperature. The finished

[1] Results in Section 2.3 are taken from [8] J. Lim, M. Jalali, and S. A. Campbell, "Properties of electrophoretically deposited single wall carbon nanotube films," *Thin Solid Films,* vol. 589, pp. 278-285, 8/31/ 2015.

SWCNT suspension along with the above process is shown in Figure 2.10 (b). A schematic of the overall setup for electrophoretic deposition is presented in Figure 2.10 (c).

Prior to SWCNT deposition, four inch silicon wafers were prepared as follows. A 300 nm thick layer of SiO_2 was grown thermally on the wafers by oxidizing at 1000 ^oC in a wet ambient for two hours. Next, a sacrificial layer of amorphous silicon (a-Si) was deposited by plasma enhanced chemical vapor deposition using a Plasmatherm 340. The process used 5 %/95 % of SiH_4/He at 10 mTorr. The plasma power was 200 W and the substrate temperature was 150 ^oC. Typical deposition rates with this recipe were about 5nm/min. The film stress was typically about 1 GPa compressive. In some cases, anchor holes were etched in the film to later create free-standing CNT films.

A thin layer of nickel (Ni) was sputtered on the substrate to act as the anode during the CNT deposition. The Ni layer was deposited using an AJA ATC 2000 sputtering system. After loading wafers into the system it was evacuated to 2×10^{-6} Torr. The Ni was dc sputtered at 5 mTorr of Ar at 250 watts. This produced a deposition rate of 10 nm/min. The Ni thickness used was 30 nm.

The cathodes used in the electrophoretic deposition cell were made of 4" diameter Ni plates. For EPD the two electrodes were held parallel in the suspension with approximately 1" of separation. A dc power supply was used to provide a constant voltage. The effects of deposition bias and deposition time were studied. After the deposition, the coated wafers were removed slowly from solution and dried horizontally in air for one hour.

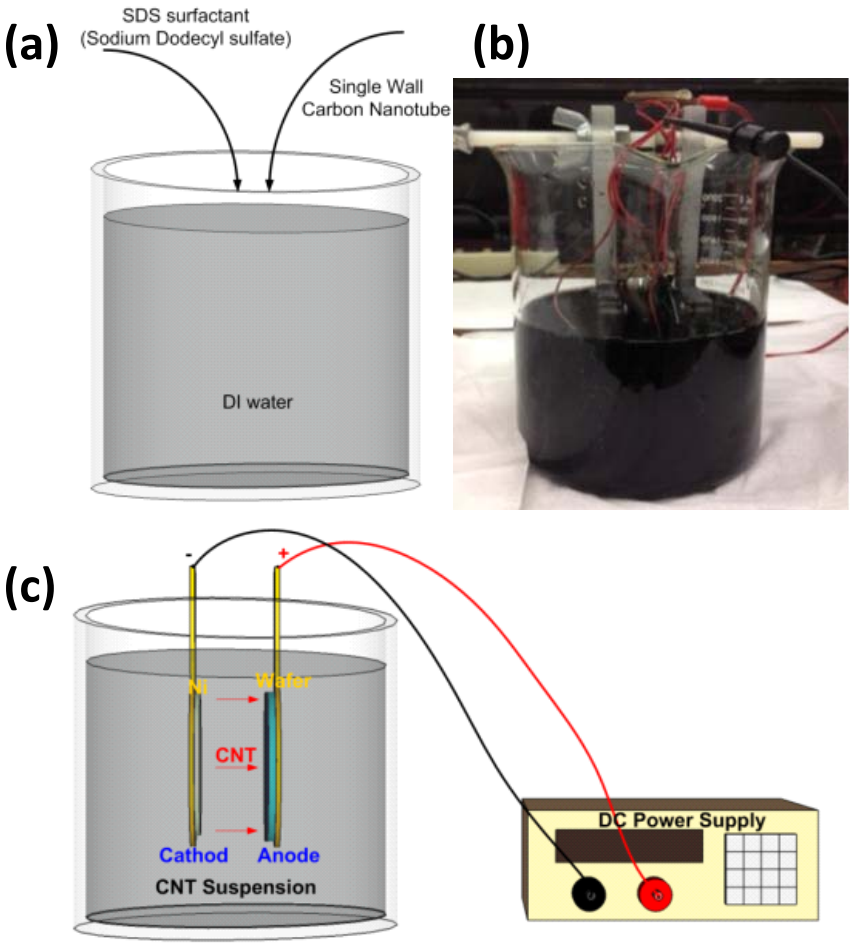

Figure 2.10 Schematic of Electrophoretic Deposition of Carbon Nanotubes (a) Prepare SWCNT suspension by adding SDS surfactants (b) Experiment image of EPD: immersed wafer in SWCNT suspension (c) Overall set up and deposition process; Reproduced from [8]

Following the deposition, the Ni anode layer was removed by a wet-etching process in a solution of $FeCl_3$ which is known not to damage the CNT during etching process [118-121]. CNTs are typically purified using an oxidative treatment such as nitric

acid or H_2O_2. To reduce CNT damage due to this treatment, the chlorine based etchant HCl, is used to remove residual metals in CNTs [118] [119]. $FeCl_3$ will release Cl- ions in a manner similar to HCl, but these ions do not damage the CNTs [120]. Thus, CNT structures will be inert during $FeCl_3$ etching. At room temperature, the observed etch rate of the Ni layer in 8 % $FeCl_3$ was 30 nm/min. The SWCNT layers were found to be sufficiently porous that the Ni could be removed underneath the SWCNTs. The absence of Ni after the etching was confirmed by energy dispersive spectroscopy (EDS). The EDS measurement is not the most accurate method to determine the concentration of some materials when there is an overlap of the corresponding peaks. We used four materials (Si, SiO2, Ni and CNT) for the EDS experiment. The peak energy of Si, O2, Ni, and C are 1.740 for K, 0.523 for K, 7.477 for K and 0.851 for L, and 0.277 for K , respectively. Therefore, the materials could be easily distinguished due to the large separation of the peak energies. The resolution of EDS is typically ~1%, so it is unable to detect trace amounts of Ni, but similar arguments could be made about Auger and XPS. After Ni etching the SWCNT film appeared to adhere to the a-Si, presumably due to surface tension.

The SWCNT film could then be patterned by plasma etching in a STS model 320 reactive ion etcher. 100 sccm of O_2 produced a system pressure of 50 mTorr. 100 W of plasma power produced an etch rate of 30 nm/min. Etched films were measured with a Tencor P-16 profilometer to determine the film thickness and surface texture. We used the average of multiple measurements to improve the accuracy.

Finally, free-standing beam structures were realized by etching the a-Si sacrificial layer of patterned SWCNT film in an STS model 320 plasma etch system. 200 sccm of SF_6 produced a system pressure of 300 mTorr. At 300 W RF power the etch rate of a-Si was 350 nm/min. We will show the fabricated free-standing SWCNT film and their characterization in a later section.

2.3.2. Results and Discussion

The SWCNT film thickness is determined by the deposition time and electric field. This section studies the effects of time and voltage with other test environments fixed. Since a fresh suspension is not generally prepared for each sample, one must take into account the deposition sequence. Figure 2.11 shows the EDP thickness of SWCNTs as a function of bias time for a constant 30 V deposition potential. We observe that there are two regimes: a zero-time deposition which occurs without applying bias, and exponential deposition regime. The zero-time offset is believed to be due to diffusive deposition occurring between the immersion of the wafer to SWCNT solution and the initial application of the bias. This depletes the solution near the surface of the wafer, creating a field that limits the film thickness. Films deposited in this initial regime are observed to be non-uniform. In the second regime, the deposited films are far more uniform and film thickness is found to depend on electric field and deposition time. The bottom SEM images with 1s, 15s, and 75s of deposition time represent the region I, II and III of the upper graph in Figure 2.11. We observe that the SWCNT films have more

bundles with increased deposition time. As a result, the deposition time affects the film porosity and density, as discussed in more detail later.

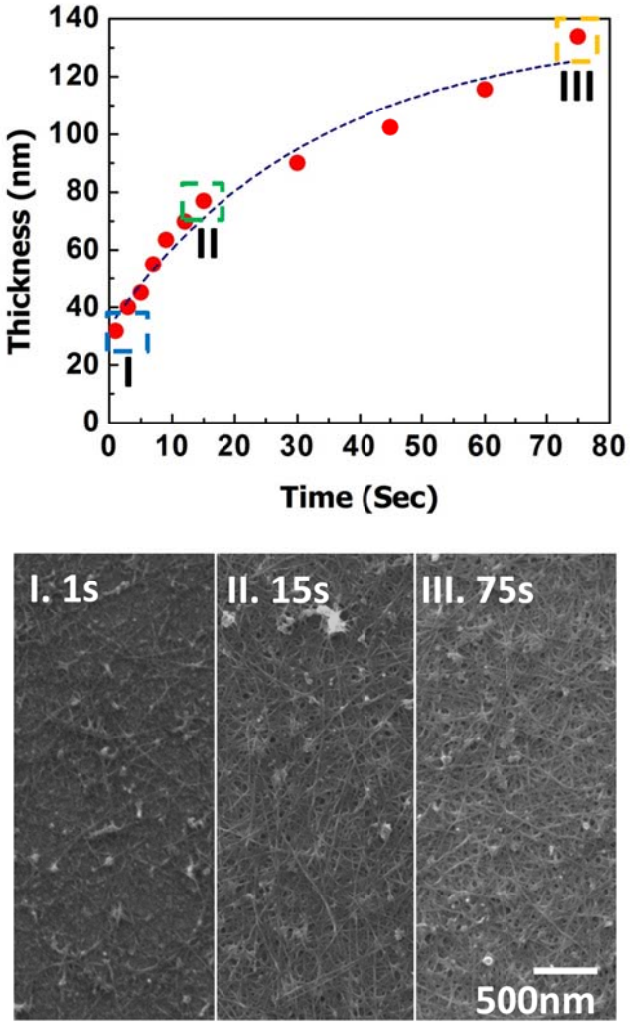

Figure 2.11 Schematic of deposited SWCNT film thickness by time with 30 V of applied bias. The dashed line shows a fit of the data to the exponential equation of Sarkar and Nicholson. SEM images (1s, 15s and 75s of deposition time) represent the region I, II, and III in above graph. II, and III in above graph; Reproduced from [8]

EPD consists of a two-step process: electrophoresis and deposition. During electrophoresis step, the dispersed negative charged particles in the suspension are accelerated toward the positively charged electrode by an applied electric field. The adsorbed particles coagulate to form a film on the electrode surface [4, 122]. Thus, we should consider each step to understand the mechanism of EPD.

The kinetics of the process was derived in a classic paper by Hamaker using a simple mass conservation principle [76]. Cho *et al.* demonstrated the EPD mechanism for thick CNT films used with Hamaker' equation [71]. We find that the Hamaker's equation explains our long depositions, finding that the deposited weight is proportional to the electric field and concentration. However, the Hamaker's explanation cannot be used to explain our thin film deposition data. We find that the variation concentration equation from Sarkar and Nicholson is more suitable for our films as shown in figure 2.11. This exponential equation is explained in the previous chapter in detail.

During deposition, we used constant-voltage EPD. In spite of the fixed potential, we observed that the current decays with deposition time. Two mechanisms may be responsible. The first is the accumulation of SWCNTs on the substrate leads to an increase in resistance, decreasing the current during the EPD process [4]. The second explanation is the decreasing SWCNTs concentration in suspension with increasing deposition time as shown in figure 2.12 (a). The second step of the EPD mechanism, deposition, is still disputed. The aggregation of particles on the electrode surface depends on the surface chemistry of particles and on particle-particle and particle-substrate interactions. The interactions in liquid solution are well described by DLVO theory [79].

During EPD processing, the interaction energy curve is shifted due to the externally applied electric field. Particles start to agglomerate when the applied energy overcomes the mutual repulsion force. This deposition phenomenon is explained using the theory of the electrical double layer (EDL) distortion and thinning as proposed by Sarkar and Nicholson [4, 77]. This mechanism suggests that charge particles moving through the suspension attract oppositely charged species that partially screen them. When an electric field is applied, the oppositely charged shell is distorted, thinning ahead and thickening behind, due to fluid dynamics [123].

We find that k=0.03 sec^{-1} provides a good fit to the data. Assuming f=1, the average velocity of particle during deposition which is calculated using k value is 0.37 cm/s. The particle velocity is the product of electrophoretic mobility (μ) and of electric field (30 V/inch), thus the electrophoretic mobility of particles is calculated to be 0.031 cm^2/V-sec. Chowdhury *et al.* investigated the electrophoretic mobility of SWCNTs in aqueous media and found typical values of $1.5x10^{-4}$ cm^2/V-sec at a pH of 7 [124], about a factor of 50 smaller than our result. This difference is due to the electric field variation during deposition. The deposited mass raises the electrical resistance of the substrate and thus reduces the electric field. Thus, we need some other method to calculate the accurate electrophoretic mobility and explain the EPD mechanism. We will come back to this in a later section.

If deposition time is enough long to be considered in the steady-state regime, our result could be explained with the Hamaker's equation as mentioned above. We extrapolate back from the constant deposition rate in this equation to zero time to find an

effective thickness offset (T_{offset}) which includes the deposition during short period of time. Then, the thickness in steady-state region can be expressed as

$$T = T_{offset} + 0.93\ nm/\sec * t \tag{2.3}$$

where t is the applied time.

Since the initial electrophoretic deposition should have a voltage dependence, we measured the film thickness for applied voltages from 10 to 40 V and fixed deposition time. Figure 2.12 (b) shows that the deposited thickness depends linearly on the electric field. This result is well explained with Hamaker's equation. Also, it illustrates that the deposited mass saturates over 30 V of applied voltage. The observation may simply reflect an increase in the time the system spends in the exponential regime as the voltage is increased. Thus, T_{offset} may depend on the applied voltage. The offset may also depend on the SWCNT concentration in the suspension. To study this, we measured concentration effect on film thickness. Figure 2.12 (a) shows that the deposition rate decreases with repeated 75 sec, 30 V depositions with a fixed suspension. The observed reduction is believed to be due to the decrease of the SWCNT concentration in the suspension [83]. Concentration also affects to the deposited film thickness according to Hamaker equation. Moreover, this diminishing may follow a decrease of deposition time in the exponential regime. In summary, the deposition voltage and suspension concentration affect the offset to the exponential regime.

The structure of the SWCNT films produced at 30 V for 45 sec was observed by SEM (JEOL-6500) and AFM. Figure 2.13 (a) shows a randomly oriented network of SWCNTs on Ni deposited wafer substrates. The micrograph suggests that the film is

comprised of bundles, typically 10 to 20 nm in diameter. Small agglomerates, 30 to 60 nm in diameter, are also seen. AFM measurements indicate an RMS roughness of 22 nm for a 102 nm thick film.

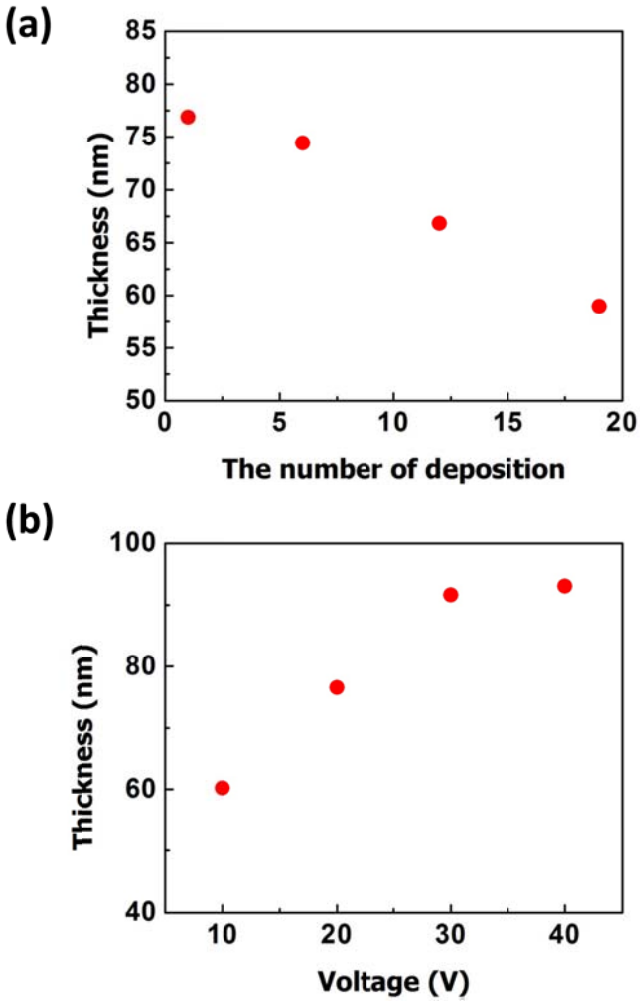

Figure 2.12 (a) SWCNT film thickness with repeated depositions under fixed deposition voltage and time (b) SWCNT film thickness as a function of applied voltage with a fixed deposition time; Reproduced from [8]

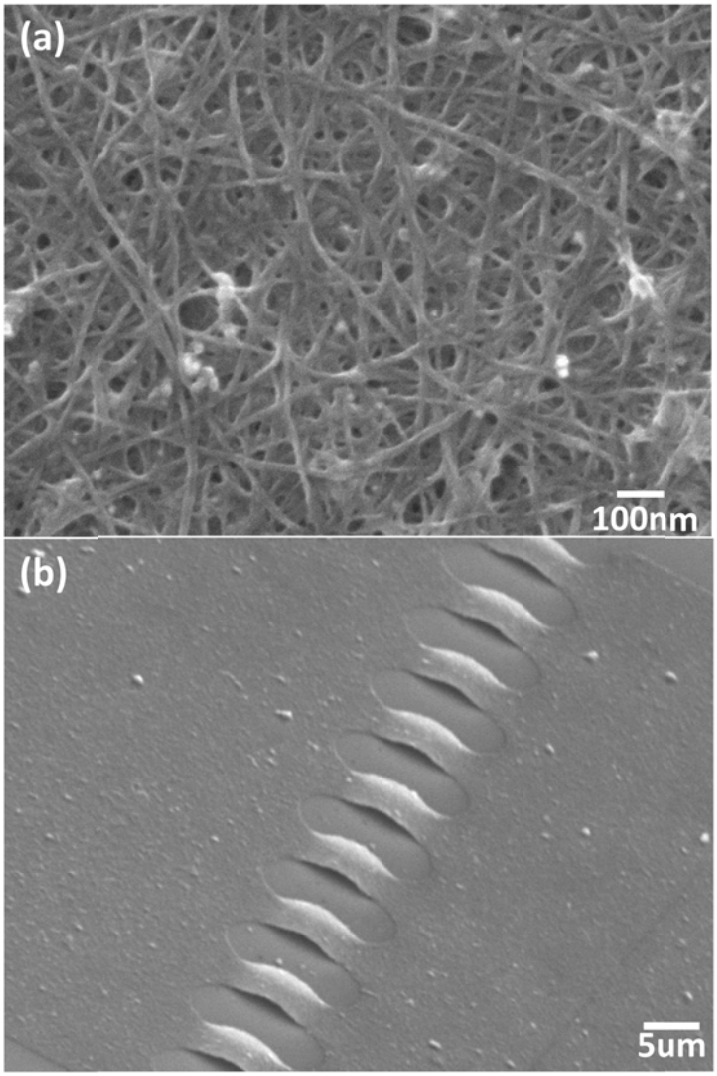

Figure 2.13 (a) SEM image of randomly distributed SWCNTs deposited at 30 V for 45 sec (b) SEM image of free-standing SWCNT beams; Reproduced from [8]

Finally, we used the Ni etch and a-Si removal processes as described in the previous section to create free-standing fixed-fixed beam structures using the SWCNT films as shown in Figure 2.13 (b).

2.4. Summary

This chapter provided a theoretical review of the EPD process and explained routes to stable suspensions. The role of the surfactant was described with particle dispersion and simulation results. Based on these explanations, the electrophoretic deposition process was suggested with a detailed explanation. Experimental results were then presented. Few tens to hundreds of nm thick thin single wall carbon nanotube films were produced within a short period of times using an EPD process at room temperature. The deposited SWCNT film thickness was in good agreement with the Hamaker or the exponential equation from Sakar and Nicholson with an initial offset value. The initial deposition regime depends on the applied constant voltage during EPD process and the SWCNT concentration in suspension. The deposited film thicknesses were controlled by maintaining the process voltage and time. Lastly, free-standing structures of thin SWCNT films were fabricated by removing the Ni layer and a-Si sacrificial layer under the SWCNT film. The EPD process to deposit CNT film can be extended to flexible devices or many other MEMS devices that are few tens of nm thick or free-standing SWCNT films by etching the metal layer and the sacrificial layer.

Chapter 3.

Characterization of EPD SWCNT Films:
Density, Electrical, Optical and Mechanical Properties

3.1. Overview

This chapter discusses several characterization techniques to determine SWCNT film properties including mass density, electrical, optical, and mechanical properties. The film mass density is determined by Rutherford backscattering spectroscopy (RBS). The electrical properties are measured with patterned SWCNT film using an HP4156 parameter analyzer. The optical properties are determined with transferred SWCNT film on transparent glass slides using a spectrometer. Finally, the mechanical properties of films are determined by two methods: straightforward nanoindentation of films on a substrate and calculation and by direct nanoindentation measurement of free-standing thin films.

3.2. Density of SWCNT film

Density is a key factor in the design of MEMS/NEMS devices such as resonators and actuators [125]. Rutherford backscattering spectrometry can be used to obtain the SWCNT film mass density [126].

3.2.1. Basic of RBS

Rutherford backscattering spectrometry (RBS) uses ions with a known energy incident on a sample. One measures the energy of the backscattered ions. The RBS system consists of a helium ion generator, an ion accelerator, and a detector. He^- are generated in the ion generator, and are then accelerated to 1 MeV in the ion accelerator. During the acceleration, two or three electrons are stripped from the He^- ions and eventually the He^- ions form He^+ or He^{2+} ions, respectively. The He ions are incident on the sample and the backscattered ions from target sample are detected by detector [1].

The backscattering yield Y (in counts for channel) is expressed as [1]

$$Y = \sigma \Omega Q N_s \tag{3.1}$$

where σ, Ω, Q, and N_s are the average scattering cross-section, detector solid angle, the number of ions incident on the sample, and sample areal density (atoms/cm^2), respectively. $N_s = Nd$ for thin film where N is the density (atoms/cm^3) and d is the film thickness. The film thickness can be measured with other techniques such as profilometry, AFM, and ellipsometry. The backscatter yield (Y), detector solid angle (Ω), and the number of ions incident on the target (Q) are determined through the RBS measurement. The number of incident ions is calculated by the time integration of the ion current, but secondary sample electron emission must be overcome or compensated. The average scattering cross section (σ) is written as [1]

$$\sigma = \frac{1}{\Omega} \int \frac{d\sigma}{d\Omega} d\Omega \tag{3.2}$$

The differentiated of scattering cross section is expressed as [1]

$$\frac{d\sigma}{d\Omega} = \left(\frac{e^2 Z_1 Z_2}{2E_0 sin^2\theta}\right)^2 \frac{[\sqrt{(1-(Rsin\theta)^2} + cos\theta]^2}{\sqrt{(1-(Rsin\theta)^2}} \quad (3.3)$$

where θ, Z_1 and Z_2 are scattering angle, the atomic number of the beam ion, and the atomic number of target, respectively. In conclusion, the film density can be calculated using Equation 3.1. Figure 3.1 describe the collision and backscattering between incident ions and sample targets.

For analyzing the measurement data of RBS system, two concepts should be considered. The first is the effect of the relative masses. The response of materials such as nitrogen (N) and oxygen (O) that are lighter than the substrate material (usually silicon), appear superimposed on the background substrate data as shown in Figure 3.2 (a). Moreover, the film thickness affects the position of substrate as illustrated in figure 3.2 (b). The moved channel or energy substrate region is due to the energy loss produced by ions traveling through the film.

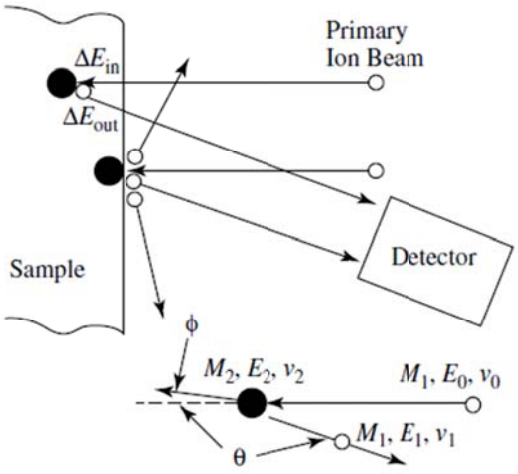

Figure 3.1 Schematic of Rutherford backscattering spectrometry; Reproduced from [1]

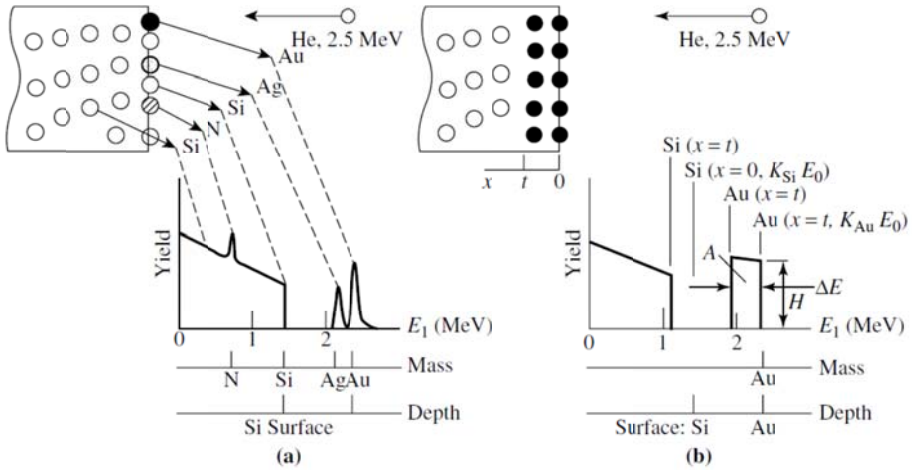

Figure 3.2 (a) Schematic of measured spectrum of different materials (b) schematic of RBS spectrum for Au film on Si; Reproduced from [1]

3.2.2. Measurement result and discussion[2]

For the density measurement, we prepared the samples with a SWCNT film deposited using the EPD process. We used RBS before etching the Ni seed layer. Figure 3.3 (a) illustrates the RBS result. The continuous feature from channel 100 to about 370 represents the single crystal silicon wafer. The trace from 100 to 330 and the feature from 185 to 225 are due to the Si and O_2 respectively in the 300 nm thick SiO_2 layer. The major peak near 510 is due to Ni. Carbon nanotubes are the rolled honeycomb structure of carbon. The atomic number of carbon, 6, is lighter than atomic number Si substrate, 14. Therefore, the RBS yield of carbon is positioned on the background of substrate as shown in Figure 3.3 (a). The peak of interest here around 155 is due to the CNT film.

[2] Results in Section 3.2 are taken from [8] ibid.

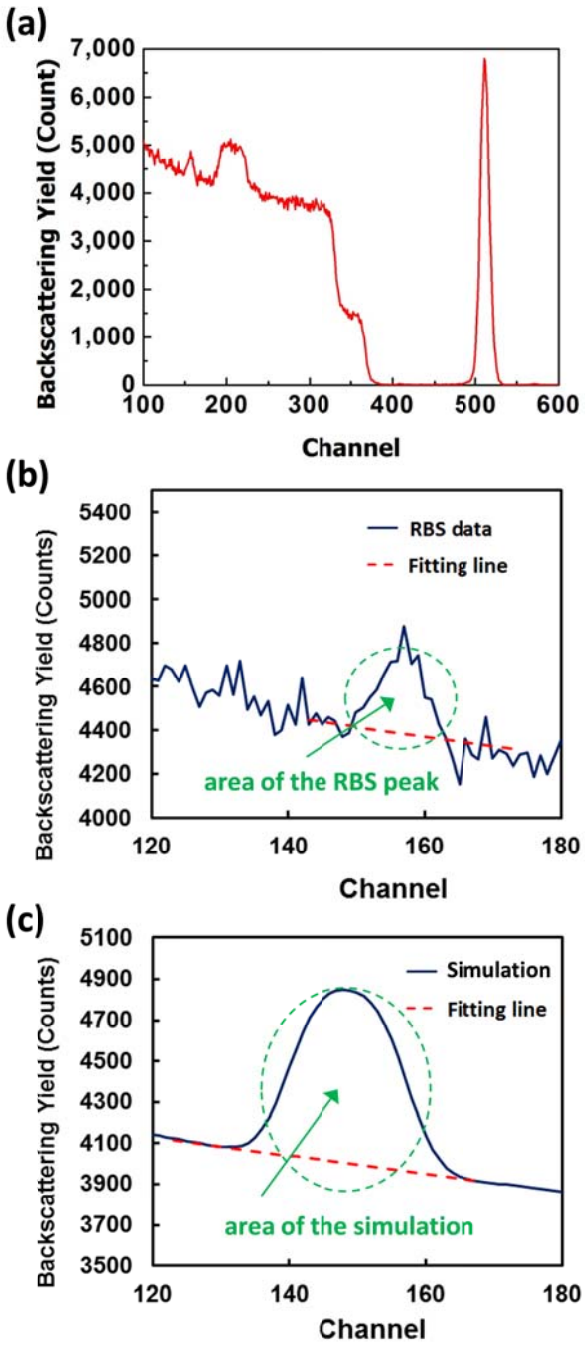

Figure 3.3 (a) Yield-channel graph of RBS measurement after SWCNT film deposition; Reproduced from [8] (b) Area of CNT film area in Yield-channel curve (c) Area of simulation result with same environment

The mass density of the SWCNT film is calculated using Equation 3.1. Substrate parameters, including density (N_s), thickness (d), atomic number (Z) and mass (m), are well known for materials such as Ni, SiO_2 and Si. The backscatter yield (Y), detector solid angle (Ω), and the number of ions incident on the target (Q) are controlled or determined during the RBS measurement. If the film thickness is known from a profilometer measurement, the density can be determined as

$$\rho_{film} = \rho_C \frac{A_{film}}{A_C} \tag{3.4}$$

where ρ_{film} and ρ_C are the mass densities of the SWCNT film and bulk carbon (2.267 gm/cm^3) respectively, A_{film} is the area of the RBS peak due to the deposited CNT film as depicted in Figure 3.3 (b), and A_C is the simulated area of bulk carbon with the same thickness as the CNT film as illustrated in Figure 3.3 (c). It is worth mentioning that the carbon atoms contained in SDS surfactant do not significantly affect the density of the CNT film calculated in this manner. There is no direct accurate measurement of the fraction of the SDS surfactant that is incorporated in the film, however one can make a simple estimate. Experimental results suggest that the limiting case is that the SDS surfactants are fully adsorbed on the surface of CNT bundles in suspension and that the deposited film has the same proportion of SDS as the solution. Under this situation the effect of the SDS is only 5% of the total density. Therefore the effect of the SDS surfactant is not considered when calculating CNT density.

The result of this analysis is shown in Figure 3.4. The density was found to be independent of deposition voltage and suspension usage. Instead it depended only on film thickness [127]. We believe that this effect is caused by increasing the number of bundles

and the increasing film uniformity as shown in Figure 2.12 (a). Large diameter bundles increase the film density because of the high packing densities in bundles.

For very thin films, the density varies linearly with thickness, reaching a value of 0.12 gm/cm^3 for a 28 nm thick film. The rate of density increase slows at larger values of thickness. If the measured results are extrapolated, the film thickness would saturate at about 0.6 gm/cm^3 for a 200 nm film. The film density is ultimately limited by that of closely packed CNTs [11]. If one assumes that the film is consisted of carbon bundles (10 to 20 nm of diameter) and the minimum distance between individual CNTs is the same as sum of the interplanar stacking distance of graphene sheet (0.34 nm) and length of SDS surfactant (1nm), then the density of an ideally packed CNT film is 1.01 ~ 1.13 gm/cm^3 depending on the bundle diameter, in good agreement with the extrapolated limit of the data in Figure 3.4. The measured film density is much smaller than the ideally packed density. We expect that the film porosity is one possible reason for the difference. The SEM image shows that the deposited SWCNT film has many porous areas as shown in Figure 2.12(a).

As mentioned above, the rate of EDP should follow Hamaker's equation when deposition time is sufficient to be in the linear regime. Then, Hamaker's equation can be expressed in a differential form as

$$\frac{dm}{dt} = C\mu AE \tag{3.5}$$

If we confine our analysis to the deposition region in which the density is proportional to the thickness (30 to 100 nm), this can be rewritten as

$$\frac{dx}{dt} = \frac{C\mu E}{\rho_o + x\frac{d\rho}{dx}} \tag{3.6}$$

where ρ_o is the zero thickness density and x is the film thickness. If we take E to be the average field between the plates (30 V/inch) and fit our data, the electrophoretic mobility (μ) is found to be 0.045×10^{-4} cm^2/V-sec. However, this calculation substantially underestimates the deposition field since most of the space between the electrodes is electrostatically shielded. A simple estimate of the space charge region near the anode is set by the thickness of the initial diffusive deposition. That is, the film that forms due to the initial diffusion depletes the region near the plate. The thickness of such a film is about 30 nm (Fig. 2). From Figure 4 (b), this corresponds to a deposited mass of 1.8×10^{-6} g/cm^2. For a suspension concentration of 1 mg/cm^3, this would require a depleted solution width of 1.8×10^{-3} cm. If we assume that the voltage drop occurs primarily in these depleted regions, and half of the voltage is dropped at each electrode, the mobility

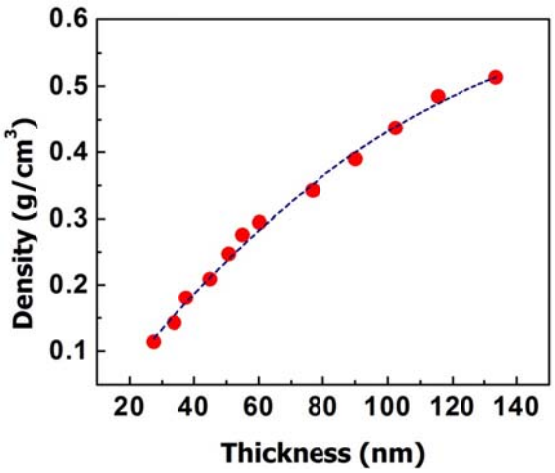

Figure 3.4 SWCNT film density-thickness curve; Reproduced from [8]

is calculated to be ~6x10^{-5} cm^2/V-sec. This result is almost half of the typical values of 1.5x10^{-4} cm^2/V-sec from Chowdhury *et al.* [124], but given the simplicity of the space charge region estimation and the approximation that no voltage is dropped in the quasi neutral region of the EDP system, this is an acceptable result.

To verify the calculated density of SWCNT film, the RBS measured data were compared with the simulation results. Figure 3.5 shows the plot of the results of experiment and simulation simultaneously with different mass densities. The energy difference between the measured and simulated data is caused by energy loss due to wrong density value of the top carbon layer as illustrated in Figure 3.5 (a). Figure 3.5 (b) demonstrates the curve of simulated and measured results with calculated SWCNT film density value from Equation 3.4.

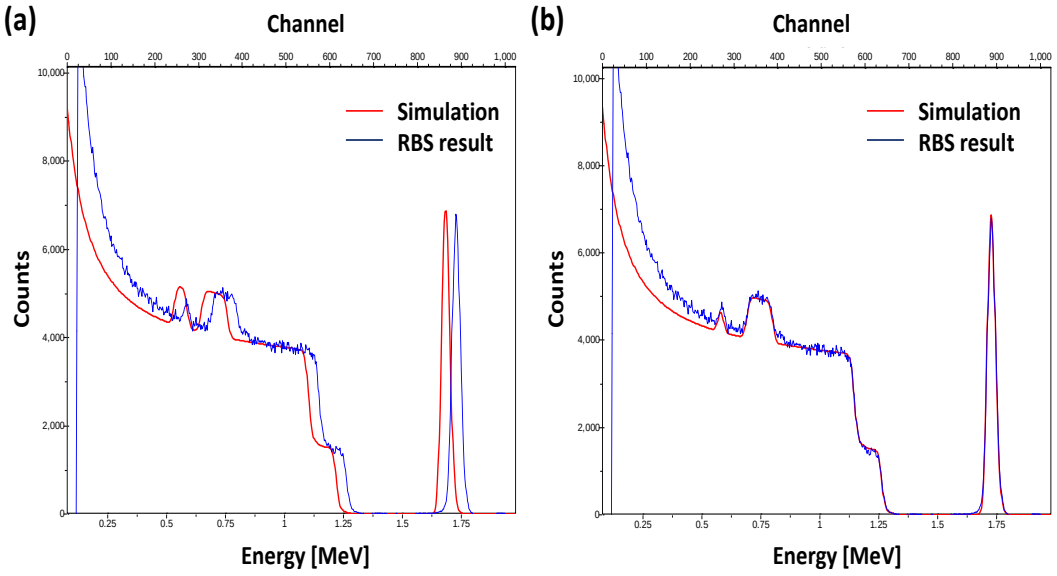

Figure 3.5 Schematic of counts-channel curve of RBS result and simulation data
(a) Simulation result with carbon film (2.267 gm/cm^3) (b) simulation result with modified density for carbon nanotube film.

3.3. Electrical and optical properties of SWCNT film[3]

The electrical properties of the films were determined by creating long, narrow (1000 μm by 10 μm) patterned strips and measuring their I-V characteristics. To prepare the samples, we deposited SiO_2 and a Ni seed layer on a Si wafer. After SWCNT deposition on the substrate using the EPD process, we etched the Ni seed layer. The complete removal of Ni was verified by EDS. The pattern was generated using photolithography and the dry etching process described in the previous section. The electrical properties of film were found from the linear current-voltage characteristics. The measured results are converted to resistivity using the device geometry and film thickness. The resistivity is found to depend primarily on film thickness. A linear relationship is found between conductivity and thickness as shown in Figure 3.6 (a). This is assumed to be due to increasing film density with increasing thickness.

The SWCNT source material used for this experiment includes both metallic and semiconducting SWCNTs, set by the individual CNT chirality [128]. Theoretically, metallic CNTs have very high mobility and 1000 times better maximum current density than copper [129]. More density may increase the paths consisting of metallic CNTs in the film.

To obtain the optical properties of the SWCNT film, the electroplated SWCNT films were directly transferred to a glass slide and the transmittance in the visible range was measured using a spectrometer. Figure 3.6 (b) depicts the average transmittance

[3] [3] Results in Section 3.3 are taken from [8] ibid..

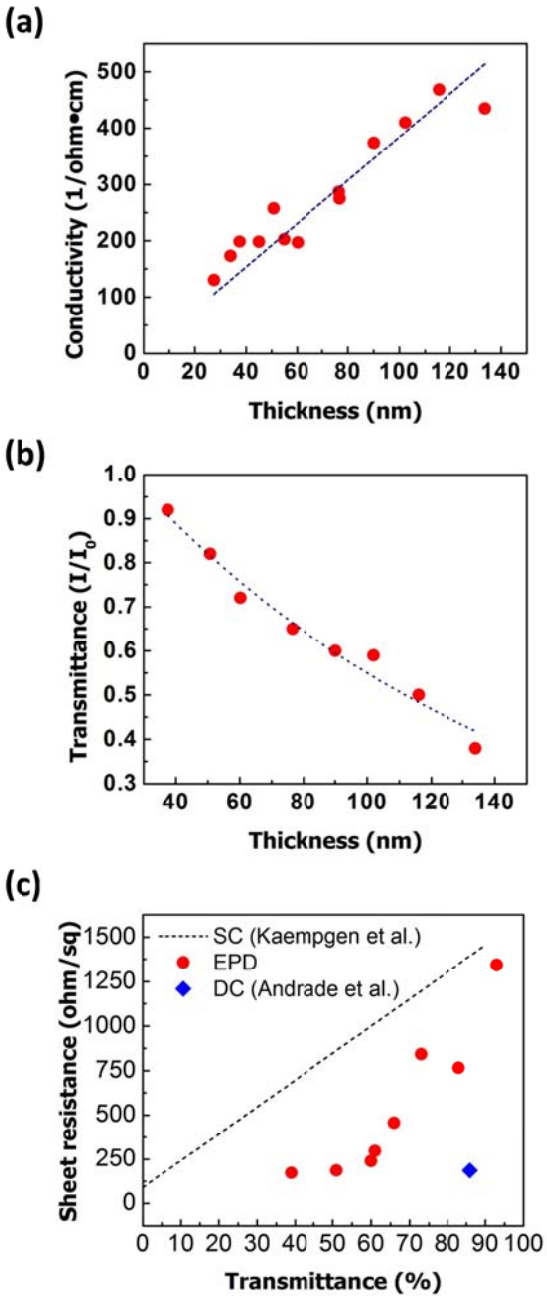

Figure 3.6 (a) SWCNT film conductivity-thickness curve (b) Average transmittance in the visible range (400 to 700 nm) vs film thickness (c) Sheet resistance versus transmittance of SWCNT films in contrast to a SWCNT film using dip coating (DC) method [14] and fit to experimental data from spray coating (SC) method [17]; Reproduced from [8].

result from 400 nm to 700 nm of wavelength. The transmittance of SWCNT film has an exponential decay with thickness/density.

Figure 3.6 (c) presents the performance of the SWCNT films characterized by the electrical sheet resistance and the optical transmittance measured at a wavelength of 550 nm. The results shown here are better than the spray coating data from Kaempgen *et al*. [17]. Lima *et al*. reported the result using EPD method which follows the same trends with spray coating method [97]. The data point for a dip coated SWCNT film reported by Andrade *et al*. had the best performance (186 Ω/square at 86 % of transparency) [14], but controlling film thickness in dip coating is difficult, especially in very thin films where surface tension effects can lead to discontinuous films.

A CNT film can be used as the transparent conducting electrode for solar cell or LED applications. This would be particularly interesting for flexible devices [130]. Our films have 238 ohm/square of sheet resistance and 60 % transmittance for a 100 nm thick film. This may be suitable for its usage in some solar applications [131].

3.4. Mechanical properties of SWCNT films

A basic MEMS actuator uses a thin suspended film above a lower electrode. For this application, it is required to know the Young's modulus of the membrane to predict the pull-in voltage [132]. Nanoindentation has been used to characterize the mechanical properties of films due to its ability to control indentation depth on the nanoscale, high spatial resolution and its ease of use [133]. Nanoindentation measures the force and displacement while a probe tip is indenting to the sample. Figure 3.7 shows the schematic

of nanoindentaion. The displacement sensor has three parallel plates for capacitance measurement. Top and bottom plates are fixed in the system, while the middle plate which is adhered to the tip is moving in the vertical direction. The position of probe tip is precisely controlled by the voltage difference across the plates.

Two different methods were used to determine the Young's modulus using nanoindentation system. One is the direct measurement for a film on a rigid substrate. It assumes a homogeneous film. The other uses the deflection of free-standing membrane and uses modelling to extract the Young's modulus.

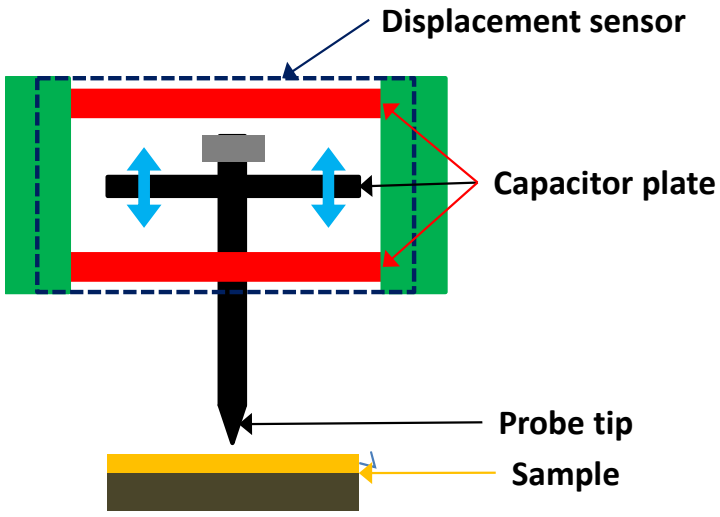

Figure 3.7 Schematic of nanoindentation system

3.4.1. Straightforward nanoindentation for SWCNT film[4]

The mechanical properties of the films were studied using nanoindentation. In this technique, a load is applied through a Berkovich tip and the displacement is measured as a function of loading. The unloading curve provides a measure of elastic modulus through the slope S as

$$S = \frac{2}{\sqrt{\pi}} E \sqrt{A_c} \tag{3.7}$$

where E is the Young's modulus and A_C is the contact area. The latter is given by $A_C = 24.5h_c^2$ where h_C is the linear intercept of the initial unloading curve on the displacement axis [133]. The displacement was limited to no more than 10% of the film thickness to minimize substrate effects [134]. A single-wall carbon nanotube has a 1 TPa axial modulus due to their strong carbon-carbon bonds [135]. We made SWCNT film using EPD process, and the deposited film has randomly oriented CNTs. These randomly positioned CNTs have much weaker CNT-CNT forces and so should give softer mechanical properties. The Young's modulus of the SWCNT films was found to be 5.2 ±0.5 GPa for films between 75 and 135 nm thick, as shown in Figure 3.8. These results are consistent with reports by other groups on films make using different deposition mechanisms. Multi-wall carbon nanotube films have reported values from 7.7 to 157.8 GPa [15]. Aligned-SWCNT films have reported 9 to 57 GPa (depending on the diameter of CNTs) in the radial direction [136]. In most films, the Young's modulus is correlated with density [137]. However, we do not observe this result in our SWCNT films. We suspect that the presence of the SDS surfactant, which stabilizes the SWCNT suspension

[4] Results in Section 3.4.1 are taken from [8] ibid.

for the EPD process, significantly decreases the Young's modulus of the films. After deposition, the surfactants adsorbed on the surface of the SWCNTs remain between the SWCNTs with non-covalent bonding [138]. Thus, weak bonding between SWCNTs and surfactants play the dominant role in determining the mechanical properties of the film.

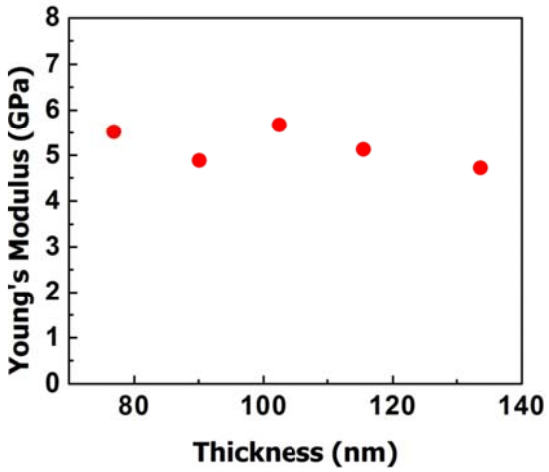

Figure 3.8 Young's modulus measured with triboindenter versus SWCNT film thickness; Reproduced from [8]

3.4.2. Young's modulus of free-standing circular film under point load[5]

For the Young's modulus measurement, the nanoindentation system is used to collect the deflection data of free-standing thin (few tens to hundreds thick) films. Modeling can then be used to extract the mechanical properties of these films [139]. This

[5] Results in Section 3.4.2 are taken from [3] S. A. C. Junyoung Lim, "Electromechanical Switches Fabricated by Electrophoretic Deposition of Single Wall Carbon Nanotube Films," *In processing,* 2015..

requires a model of the mechanical behavior of the film. The next sections will discuss candidate models that could be used for the Young's modulus extraction and techniques for making the sample. First, the models for a free-standing circular membrane under point load are introduced. Then the fabrication technique for a free-standing structure is developed using a modified Langmuir-Blodgett method. Finally, the Young's modulus of a SWCNT film is determined using the nonlinear model and a fabricated sample.

3.4.2.1. Models for mechanical properties using load-displacement data

Timoshenko reported many models to calculate the mechanical properties of films with different shapes and the load type [140]. In spite of many efforts to find a single solution, there are many models according to the load type and the characteristics of membrane. Relevant characteristics include thickness, prestrain, shape and Young's modulus. Models are summarized in Table 3.1 categorized with load type, membrane shape and membrane behavior during indentation (linear or nonlinear).

Komaragiri *et al.* developed models for the determination of the mechanical properties of free-standing circular thin films with both point and pressure loads based on the simplified Reissner theory [141, 142]. They considered an isotropic elastic circular film with applied load and small strains. They categorized three regions following two dimensionless parameters: a function of prestretch and film thickness and a function of load and film thickness.

Table 3.1 Overview of categorized models

	Linear bending		Nonlinear bending or stretching	
Shape / Load	Circular	Rectangular	Circular	Rectangular
Point	[140, 143-145]	[140, 146, 147]	[140, 144, 148-150]	[149]
Pressure	[140, 149, 151, 152]	[140, 146, 147, 149]	[144, 149, 151, 153-156]	[149, 157-162]

They find that the linear plate model can be used for the case of negligible stretching compared to deformation. The linear plate model is expressed by [142]

$$\frac{w}{a} = \frac{3(1-\nu^2)}{4\pi}\left(\frac{Pa}{Eh^3}\right) \tag{3.8}$$

where a, w, υ, E, h, and P are the circular radii, the deflection, Poisson ratio, Young's modulus, film thickness and the applied load, respectively. Corresponding to the classical plate theory, the linear plate theory ignores nonlinear kinematics. In other words, loads are enough small to expect small deflections.

The prestretched membrane model is used for small loads. The prestretch membrane model is given by [142]

$$\beta(r) = \left(\frac{6Pa(1-\nu^2)}{\pi h^3}\right)\frac{1}{\kappa}\left\{\frac{I_1(\kappa r)}{I_1(\kappa)}\left[I_1(\kappa r) - \frac{1}{\kappa}\right] - \left[K_1(\kappa r) - \frac{1}{\kappa r}\right]\right\} \tag{3.9}$$

$$\mathrm{w(r)} = \int_r^a \sin\beta(s)ds \tag{3.10}$$

where κ is expressed by [142]

$$\kappa = 12\varepsilon_0(1+\nu)\left(\frac{a}{h}\right)^2 \tag{3.11}$$

and β, r, I_1 and K_1 are the angle of rotation, distance from a center of the circle, the modified Bessel's function of the first and second term, respectively. Deflection of the film is determined using a numerical analysis of Equation 3.10 and Equation 3.9. This model is applicable when loads are enough small to avoid large deflections and the generated stiffness by prestrain is greater than or equal to the bending stiffness.

Lastly, the nonlinear membrane model is used for very thin films where membrane behavior dominates prestretch. The nonlinear model is written as [142]

$$\frac{w}{a} = \left(\frac{3P}{\pi Eah}\right)^{1/3} \tag{3.11}$$

where a, w, E, h and P are the circular radii, the deflection, Young's modulus, film thickness and the applied load, respectively. This model is suitable when bending stiffness is negligible comparing with the stiffness that is generated by stretching arising from large deflection.

3.4.2.2. Fabrication of free-standing circular SWCNT film

A substrate was prepared by thermally growing a 300 nm thick layer of SiO_2 on a Si wafer in wet ambient at 1000 °C for 2 hours. A 30 nm thick nickel (Ni) seed layer was deposited on the substrate by sputtering. The suspension for EPD was prepared by mixing 1 mg/mL of SWCNT and 1 wt % of the sodium dodecyl sulfate (SDS) surfactant in deionized (DI) water. The SDS surfactant was used to impede SWCNT agglomeration in suspension. The mixture was sonicated for one hour and centrifuged at 3500 RPM for one hour. Next, the EPD process was run to deposit the SWCNT film with a constant 30V of deposition potential and various deposition times. Figure 2.13 (a) shows an SEM image of a SWCNT film deposited in this manner.

After EPD, we used $FeCl_3$ to remove the Ni seed layer and transfer the detached SWCNT film to the tungsten metal plate. The metal plate has a thickness of 1 mm and an array of holes with various diameters ranging from 180 um to 500 um. This transfer technique is similar to the Langmuir-Blodgett method (Figure 3.9 (a)). The transferred SWCNT films were dried in clean room conditions for 1 hour. Figure 3.9 (b) shows a microscopic image of a transferred film, similar to other free-standing films [163].

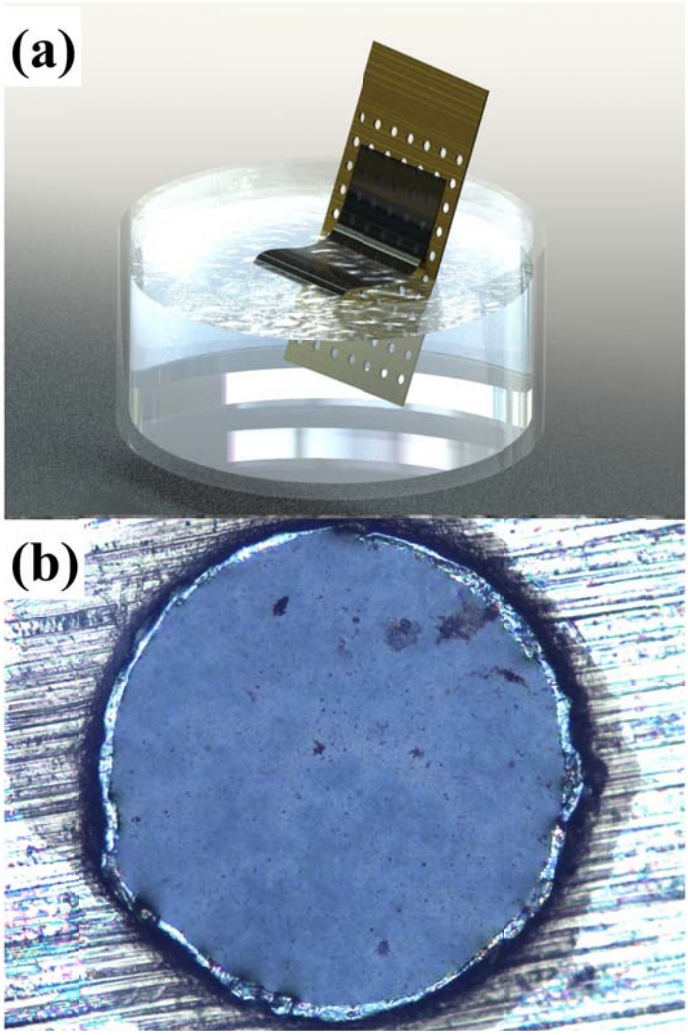

Figure 3.9 (a) Schematic image of the process of transferring a CNT film to the metal plate using a modified Langmuir-Blodgett method (b) Microscopic image of transferred film on the metal hole; Reproduced from [3]

3.4.2.3. Characterization of elastic modulus[6]

We used the nonlinear membrane model for a circular free-standing film and a point load [142] for nanoindentation characterization. Figure 3.10 (a) is a schematic

[6] Results in Section 3.4.2 are taken from [3] ibid.

illustration of the membrane deflection experiment, where a, w and P are the circular radii, the deflection, and the applied load, respectively. The model is suitable for very thin films, and we used CNT films with thicknesses from 60 to 130 nm. To calculate the mechanical properties of the SWCNT film, we approximated it as an isotropic elastic media clamped at the edge. This boundary condition is easily realized experimentally [164]. The blue line on Figure 3.10 (b) shows the measured load-displacement plot. The data revealed that the measured point load-displacement data was proportional to the cube root of load [149] as expected. The red line in Figure 3.10 (b) indicates the calculated load-displacement predicted by Equation 3.11 assuming E = 5.6 GPa. The measurement is in reasonably good agreement with the predicted curve.

We then calculate the Young's modulus of CNT film with different thickness (Figure 3.10 (c)). The Young's modulus of the CNT films is found to be 4.6 to 6.5 GPa for films in the range of 60 to 135 nm. These results are in good agreement with the reports of Yang *et al.,* [136] who deposited SWCNT films with 9 to 57 GPa of elastic modulus (depending on the diameter of CNTs) in the radial direction. The EPD process in this experiment makes randomly oriented CNT film, while Yang group used aligned-SWCNT films. Also, this work used SDS surfactant to stabilize the suspension for the EPD process. It is likely that some of these surfactants remain between CNTs after deposition.

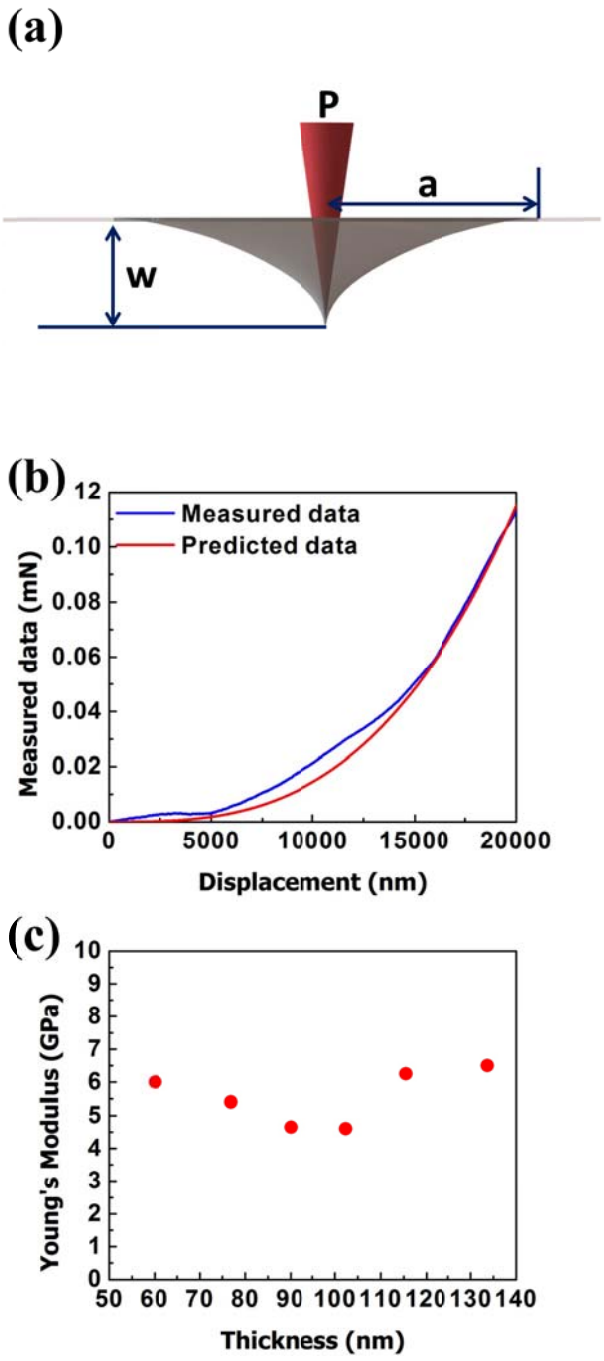

Figure 3.10 (a) Schematic illustration of the thin circular film subjected to a point load (b) Measured and predicted (with E=5.7GPa) load-displacement plots of free-standing CNT film (c) Calculated Young's modulus of CNT film by thickness; Reproduced from [3]

The SDS surfactants are adsorbed to the CNTs with a weak non-covalent bonding [138]. Therefore, the weak bonding energy might degrade the film's mechanical properties.

3.5. Improvement of SWCNT film properties[7]

With electrophoretic deposited SWCNT film, we created free-standing fixed-fixed beam structures by etching the Ni seed layer and a-Si sacrificial layer as illustrated in figure 2.13 (b). As a device application of these structures, an electrostatically controlled switch was developed with 97% device yield. The pull-in voltage was found to be in good agreement with theoretical predictions. However, the release process which removes sacrificial layer was found to increase the resistivity of the CNT layer by a factor of fifteen as shown in Figure 3.11 (a). Radical attack or physical bombardment during the etch may introduce defects in the CNTs. SF_6 molecules decompose to fluorine radicals and ions in the plasma, and exposure to these fluorides are known to increase the resistance of SWCNT films [165]. It is also possible that SF_6 plasma exposure is changing the resistance of the CNT to CNT charge transfer process by changing the surface species on the CNTs or introducing a surface charge.

To attempt to resolve this problem, we tried treating the SWCNT film in two ways: HNO_3 exposure to volatize the remaining surfactant and annealing to enhance chemical bonding and perhaps further remove residual surfactant [65, 166]. In the acid treatment method, we dipped the deposited substrate in HNO_3 (60 %) for 1 hour, soaked in DI water for 30 minutes, and then dried in air. For annealing process, we placed the

[7] Results in Section 3.5 are taken from [8] J. Lim, M. Jalali, and S. A. Campbell, "Properties of electrophoretically deposited single wall carbon nanotube films," *Thin Solid Films,* vol. 589, pp. 278-285, 8/31/ 2015.

sample in a H_2/N_2 gas flow at 400 ^oC for 2 hours [166-168]. Both the resistivity and the Young's modulus of SWCNT films improved somewhat after the acid treatment of a pristine film as shown in Figure 3.11 (a) and (b), respectively. The annealing process, however, increased resistivity by a factor of 15 and had no effect on the Young's modulus. The release process has about the same impact on resistivity. When the HNO_3

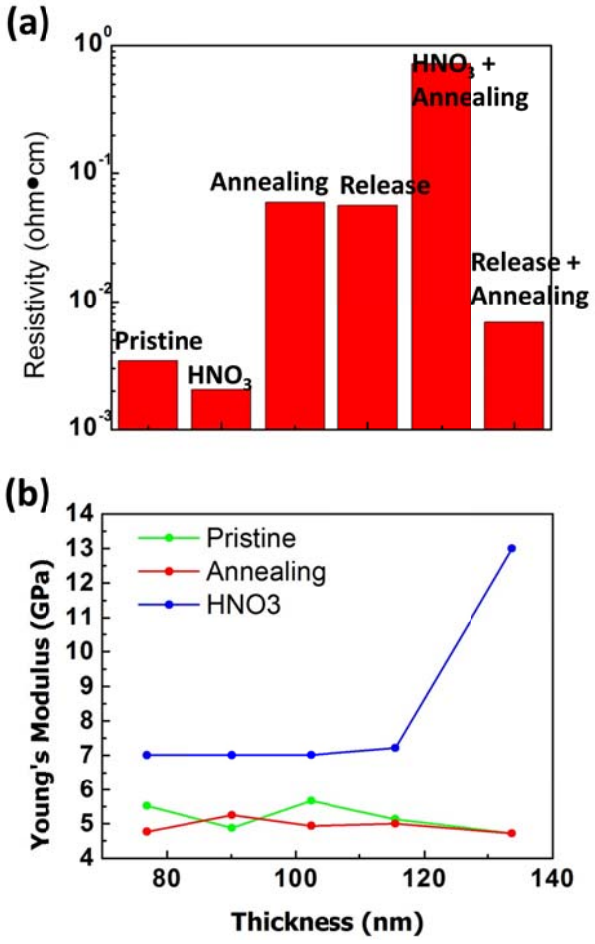

Figure 3.11 (a) Resistivity variation due to the acid treatment, annealing, and release process (b) Young's modulus with HNO_3 treatment and annealing; Reproduced from [8]

treatment is used on the released film, it deteriorates the resistivity by another order of magnitude, resulting in a resistivity that is 200 times higher than that of the pristine film. However, the anneal process reduces the resistivity of the released film dramatically, bringing it back to within a factor of two of the pristine film. Thus it seems likely that the SF_6 plasma used in the release process leaves residual fluorine on the surface which degrades conduction and that the anneal volatizes these adsorbed species, bring the electrical properties back to a condition close to those of the original film.

3.6. Summary

The density of electrophoretically deposited SWCNT film was calculated with measured RBS data. The film mass density was dependent on deposited film thickness. Electrical and optical properties were measured with fabricated samples. Conductivity is linearly dependent on the film thickness. Transmittance decreases exponentially with density. The Young's modulus of SWCNT films was measured with two different methods: straightforward for film and model-based extraction of the measured deflection of a free-standing film. We also used the deposited SWCNT film on the substrate for the former straightforward method. In the later method, we developed the fabrication process for free-standing film on pre-holed metal substrate using a modified Langmuir–Blodgett method. The mechanical property of CNT film was determined with the load-displacement results of nanoindentation. The characterized elastic moduli which are independent of the thickness show similar results in both measurement methods.

Chapter 4.

Fabrication of Electromechanical Switches Using Electrophoretically Deposited of SWCNT Films

4.1. Overview

This chapter discusses the electromechanical switch made with electrophoretically deposited single walled carbon nanotube films. It will especially focus on fabricating the low power and high frequency electromechanical MEMS/NEMS actuator mentioned in Chapter 1. The theoretical models of the electromechanical switches are first introduced. Next, the overall fabrication process of an electromechanical switch using the electrophoretically deposited SWCNT film demonstrated in Chapter 2 is described. The 'On' and 'Off' operation of switches is then characterized using electrical measurement. We then show the comparison between the measured pull-in voltage of several devices with different air-gaps and the calculated pull-in based on device geometry and the Young's modulus from Chapter 3. We also calculate the resonant frequency of the device using the fabricated device geometry and characterized film properties. Finally, expected MEMS logic problems are predicted based on the characterized MEMS device results.

4.2. Background of electromechanical device

The operation of MEMS switches is driven by force applied between a suspended beam or diaphragm and a fixed electrode. Types of forces can be categorized into repulsive and attractive. The latter includes electrostatic force due to an applied voltage, van der Waals (vdW) force and other short range forces. The repulsive force in our devices is mechanical. The free-standing beam moves to the electrode when, at every displacement of the beam, the attractive forces are larger than the repulsive force. When the attractive forces become smaller than the repulsive force, the beam is restored to the original position. The mechanical (elastic) force is determined by beam geometry and characteristics of beam. Here, short range forces are discussed. Finally, a model of the MEMS switch is described.

4.2.1. Short range forces: vdW force and Casmir force

There are two short range forces that cause adhesion in the MEMS devices: van der Waals (vdW) force and Casimir force. The vdW force is inversely proportional to the third power of the air gap [169]. It arises from a dipole-dipole interaction, including induced (i.e. image charge) dipoles and dipoles created by temporal fluctuations in the electron charge density. The magnitude of the vdW force is expressed as [170]

$$\frac{F_{VdW}}{\text{Unit area}} = \frac{A_H}{6\pi}\frac{1}{d^3} \tag{4.1}$$

where A_H is the Hamaker constant of the molecule and d is the separation between the electrode and beam. The Hamaker constant of non-polar molecules lies in the range of 0.4 to 4.0 × 10^{-19} J [171].

The Casimir effect is an attractive force between two electrically neutral and parallel conducting plates in a vacuum environment, arising from quantum fluctuations of the electromagnetic field [172-176]. Zero point vacuum fluctuations of the fields contribute to the energy in quantum theory, when there are no photons in the field. The electromagnetic field should satisfy the boundary conditions in perfectly conductive parallel plates. Then, the energy density of the field between the plates is lower than the energy density of the outer area of the plates. Therefore, there is a net attractive force, given by [172]

$$F_{Casmir}(d) = \frac{\hbar c \pi^2 A}{240 d^4} \tag{4.2}$$

where ħ is Plank constant/2π, c is the speed of light and d is the distance or gap between the plates. When the separation decreases, the Casimir force increases rapidly due to the fourth power dependence on the air-gap.

There are several reasons to neglect the Casimir force for applications of SWCNT films. First, the Equation 4.2 assumes perfectly flat plates. However, the beam bends into a curved shape, when it moves toward the bottom electrode as shown in Figure 4.1. Furthermore, a CNT beam is most certainly not flat. Instead it is made up of a collection of small diameter cylinders. Even a thin film, like those used for the fixed electrode is not perfectly flat. Groups that study the Casimir experimentally often use spherical shapes to avoid the difficulty of reliably producing flat geometries. In that case the Casimir force is inversely proportional to the third order of separation similar to the vdW force [177, 178].

Moreover, metal plates are assumed to be perfectly conductive to reflect at all frequencies. However, the finite conductivity of real metal films limits the effect at high frequency. In the free electron model, perfectly conducting metals are transparent above the plasma frequency, but the optical absorption is different in a metal with a finite conductivity. For example, gold has a 50% reflectance drop at 500 nm. Therefore even gold is not a perfect metal in electromagnetic modes at short wavelengths [179].

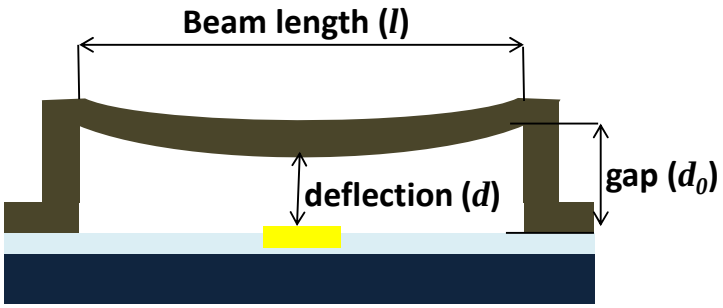

Figure 4.1 Cross section of a MEMS membrane strip

Lifshitz modified the Casimir force Equation 4.2 for a finite conducting metal plate with a frequency dependence of the dielectric function [180, 181]. The reduced Casimir force is written below with a reduction factor η_F [16]

$$F_R(d) = \eta_F F_{Casimir}(d) \tag{4.3}$$

The reduction factor is calculated using by Liftshitz expression and Drude model as shown in Figure 4.2 [16]. The result shows that the effect depends on the ratio d/λ_P, where λ_P is the plasma wavelength. The graph indicates that the Equation 4.2 is valid at

large separations (η_F=1 when d >> λ_P). However, a significant reduction factor is obtained when the gap is smaller than the plasma wavelength as [16]

$$\eta_F = 1.193\frac{d}{\lambda_P} \text{ (at } d << \lambda_P) \tag{4.4}$$

$$\lambda_P = \frac{2\pi c}{\omega_P} \tag{4.5}$$

where c is the speed of light ($3x10^8$ m/s) and ω_P is plasma frequency.

The plasma frequency is written as [29]

$$\omega_P = \sqrt{\frac{ne^2}{k\epsilon_0 m^*}} \tag{4.6}$$

where n is the electron density, k is the dielectric constant, and m* is the effective mass.

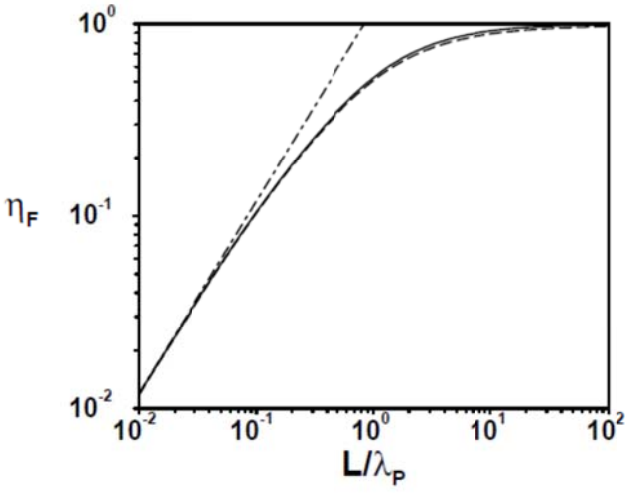

Figure 4.2 Reduction of the Casimir force compared to the force between perfect mirrors, when the finite conductivity is described by a plasma model (solid line) or a Drude model (dashed line) with a ratio d/ λ_P. The dotted-dashed line corresponds to the short distance asymptotic behavior; Reproduced from [16]

A SWCNT film deposited by EPD consists of metallic and semiconducting carbon nanotubes. The electron density of the semiconductor is much less than the conductor. Thus, SWCNT films have a much lower plasma frequency than metal films, causes the plasma wavelength to be much larger than the gap. Due to very small reduction constant, the reduced Casimir force is negligible in our MEMS/NEMS switch.

For those reasons, the Casimir force can be ignored for our electromechanical switch with SWCNT film. Figure 4.3 depicts the calculated attractive force without the Casimir force. The van der Waals force is the dominant attractive force under 10nm and is not considered for our applications because our devices have air gap over 20 nm [22].

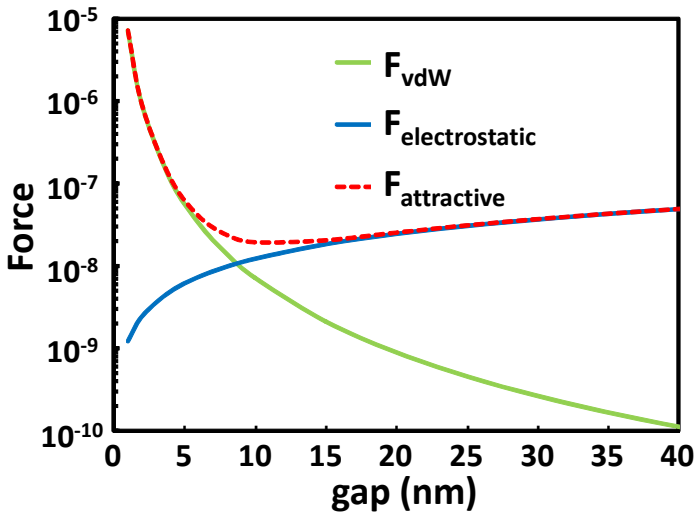

Figure 4.3 Attractive forces of MEMS switch by distance between two electrodes

4.2.2. Models of 2-terminal fixed-fixed beam structure

In the MEMS switches the repulsive force to maintain suspended beam is determined by spring constant of the free-standing beam. Thus, understanding the spring constant of cantilever beam is the basic step to design MEMS devices. The spring constant can be derived from the Young's modulus and dimensions of the free-standing beam. If the deflection of beam is enough small during operation, the external force, F (N), on the fixed-fixed beam can be calculated using $F=k\Delta y$, where k and Δy are spring constant (N/m) and beam deflection (m), respectively. In the fixed-fixed beams which are commonly used in MEMS devices, the spring constant is affected by stiffness and biaxial residual stress of the beam. The former is caused by material characteristics such as Young's modulus and the moment of inertia and the latter is decided by the fabrication process [182]. Here, we only consider the material characteristics and the beam geometry for modeling the spring constant.

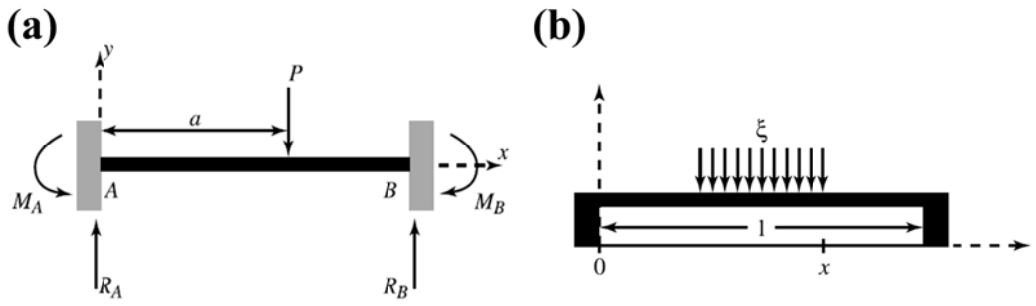

Figure 4.4 (a) Schematic of fixed–fixed beam structure (b) Schematic of fixed–fixed beam with the distributed force on the center of the beam; Reproduced from [2].

Figure 4.4 (a) shows the fixed-fixed beam structure with vertical point load. The spring constant is derived from the deflection, y, versus load position written: [2]

$$\mathrm{EI}\frac{d^2y}{dx^2} = M_A + R_A x \qquad for\ x \le a \tag{4.7}$$

$$\mathrm{y} = \frac{M_A x^2}{2EI} + \frac{R_A x^3}{6EI} \qquad for\ x \le a \tag{4.8}$$

$$M_A = -\frac{Pa}{l^2}(l-a)^2 \tag{4.9}$$

$$R_A = -\frac{P}{l^3}(l-a)^2(l+2a) \tag{4.10}$$

where E, l, M_A $(\mathrm{N}\cdot\mathrm{m})$, and R_A (N) are the Young's modulus of beam, beam length, reaction moment, and the vertical reaction at the left end, respectively. For the cuboid beam, the moment of inertia is written in below [2]

$$\mathrm{I} = \frac{\mathrm{w}t^3}{12} \tag{4.11}$$

where w and t are the width and the thickness of the beam, respectively.

It is common for MEMS devices that the load is distributed in center of the beam as shown in Figure 4.4 (b). The deflection at the center $(x = l/2)$ is expressed from Equations 4.7 to 4.11 as [2]

$$\mathrm{y} = \frac{2}{EI}\int_{\frac{l}{2}}^{l}\frac{\xi}{48}(l^3 - 6l^2a + 9la^2 - 4a^3)da \tag{4.12}$$

where ξ is the load per unit length. The spring constant for an evenly distributed load at the center of beam, $\mathrm{P} = \xi 2(\mathrm{x} - \frac{1}{2})$, is calculated from Equation 4.12 with $x = l/2$ as [2]

$$\mathrm{k} = 16\mathrm{Ew}(\frac{t}{l})^3 \tag{4.13}$$

The pull-in voltage is derived from a parallel plate capacitor structure as depicted in Figure 4.5 [183]. Electrostatic actuators have two electrodes which work like parallel conducting plates. Applying the electrostatic force induces the free-standing beam to move toward the fixed electrode. This model does not consider the fringing capacitance since for simple systems the lateral geometry is large compared to the separation. The actual capacitance can be 20-40 % larger due to fringing fields [2]. The parallel plate capacitor is [2, 183]

$$\mathrm{C} = \frac{\varepsilon_0 A}{d} = \frac{\varepsilon_0 wW}{d} \tag{4.14}$$

where ε_o, A, d, w, and W are the permittivity of free space, the overlap area of the plates, the distance between the two electrodes, and the width of the bridge beam, and the width of fixed bottom electrode, respectively. The electrostatic force is derived by considering the power delivered to a time-dependent capacitance and is expressed as [2]

$$F_{electrostatic} = \frac{1}{2}\frac{\varepsilon_0 wW}{d^2}V^2 \tag{4.15}$$

where V is the applied voltage between two electrodes. The electrostatic force is approximately assumed to be evenly distributed across the overlap area of the beam and electrode. The spring constant from Equation 4.13 is used to calculate the elastic force. The equilibrium condition is that the applied electrostatic force is equal to the mechanical restoring force as [2]

$$\frac{1}{2}\frac{\varepsilon_0 \mathrm{wWV}^2}{\mathrm{d}^2} = \mathrm{k}(\mathrm{d}_0 - \mathrm{d}) \tag{4.16}$$

where g_0 is the zero-bias gap between two electrodes.

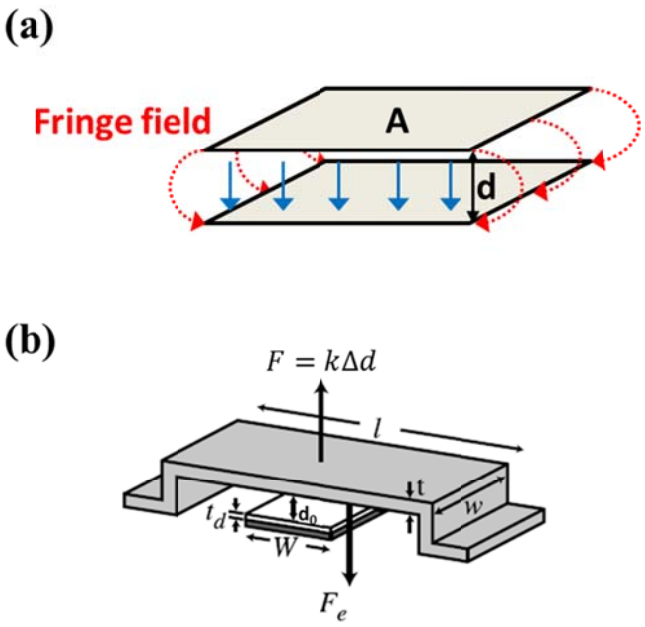

Figure 4.5 (a) Schematic of parallel plate capacitor structure (b) Schematic of fixed-fixed beam with a pull down electrode: Reproduced by [2]

The solution of Equation 4.16 is [2]

$$V = \sqrt{\frac{2k}{\varepsilon_o wW} g^2 (d_o - d)} \tag{4.17}$$

For small deflections the device has positive feedback and is stable. One can show that the pull-in voltage corresponds to a voltage needed to move the beam from initial position by about 1/3 of the original gap as illustrated in Figure 4.6. Beyond this deflection the beam becomes unstable and snaps down. The reason is that the mechanical restoring force is linearly proportional to the gap, while the electrostatic force depends on the inverse square of the gap. The beam comes into the abrupt contact with bottom

electrode once it transits into the unstable state. The pull-in voltage can be calculated with Equation 4.17 using $\mathrm{d} = \frac{2}{3} d_o$ as [2]

$$V_{PI} = \sqrt{\frac{8}{27}\frac{k}{\varepsilon_o wW}(d_o)^3} = \sqrt{\frac{128}{27}\frac{Et^3}{\varepsilon_o Wl^3}(d_o)^3} \tag{4.18}$$

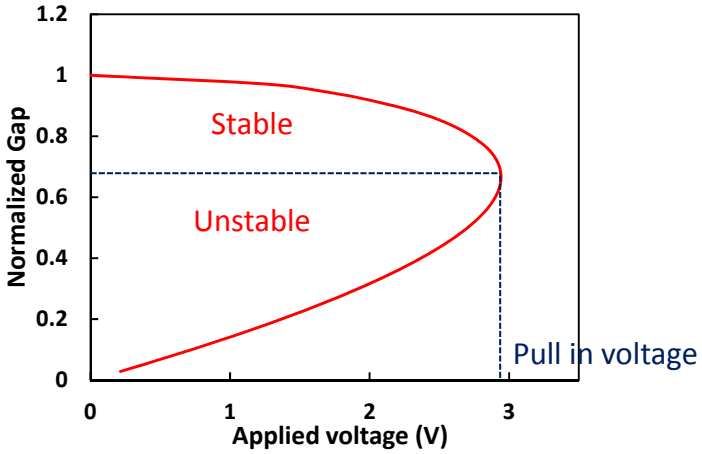

Figure 4.6 Schematic of normalized deflection by applied voltage for pull in voltage. The initial position corresponds to 1 of normalized gap.

4.3. Overall device fabrication process flow[8]

Figure 4.7 depicts the overall process steps to fabricate two-terminal switches using electrophoretic deposition of single walled carbon nanotube films. A device schematic is shown in Figure 4.8 (a). First, a 300nm thick SiO_2 layer was deposited on a 4" Si wafer. Then electrodes consisting of 70nm Pd on 10nm Cr were prepared with a

[8] These results have been accepted for publication in ref [3] S. A. C. Junyoung Lim, "Electromechanical Switches Fabricated by Electrophoretic Deposition of Single Wall Carbon Nanotube Films," *In processing,* 2015.

modified lift-off process to prevent the collapse that can occur due to sharp fences forming at the edge of a feature made by liftoff [184]. Pd was selected as fixed electrode due to the small work function difference between Pd and CNT makes an ohmic contact, reducing the contact resistance and improving the reliability [185].

Amorphous Si (a-Si) was then deposited by PECVD as a sacrificial layer for the release process. The thickness of this layer sets the actuator air gap. This film has a very large etch rate, about 3.4 um/min in a plasma with 200 sccm SF_6, 300 W power and 300 mTorr pressure formed in the STS dry etcher. As a result, we can later use a dry release step, minimizing stiction. The next step was patterning the anchor regions using photolithography and etching the a-Si using the STS dry etcher. As mentioned above, the Ni seed layer and 100nm thick SWCNT film were deposited using a sputtering system and the EPD process, respectively.

The Ni layer has to be removed since it dramatically changes the property of the suspended beam. The Ni was removed through the SWCNT film using a solution of 8 % $FeCl_3$, however the SWCNT film would peel off during this wet etching process. To hold the film in place, we used photoresist to make 2 cm by 2 cm die size openings separated by 0.5 cm stripes as shown in Figure 4.8 (b). The resist stripes anchored the CNT film during the Ni wet etch step. Once the etch process was complete, we washed the wafer with deionized water (DI) and dried it.

Next, the SWCNT beams were patterned with a photolithography and dry etching process. The SWCNT film had an etch rate of 30 nm/min in 100 sccm of O_2, 100 W rf power and 50 mTorr pressure in the STS dry etch system. Finally, the a-Si sacrificial

layer was removed using by STS dry etcher to release the suspended beam. An SEM image of a finished device is shown in Figure 4.8 (c).

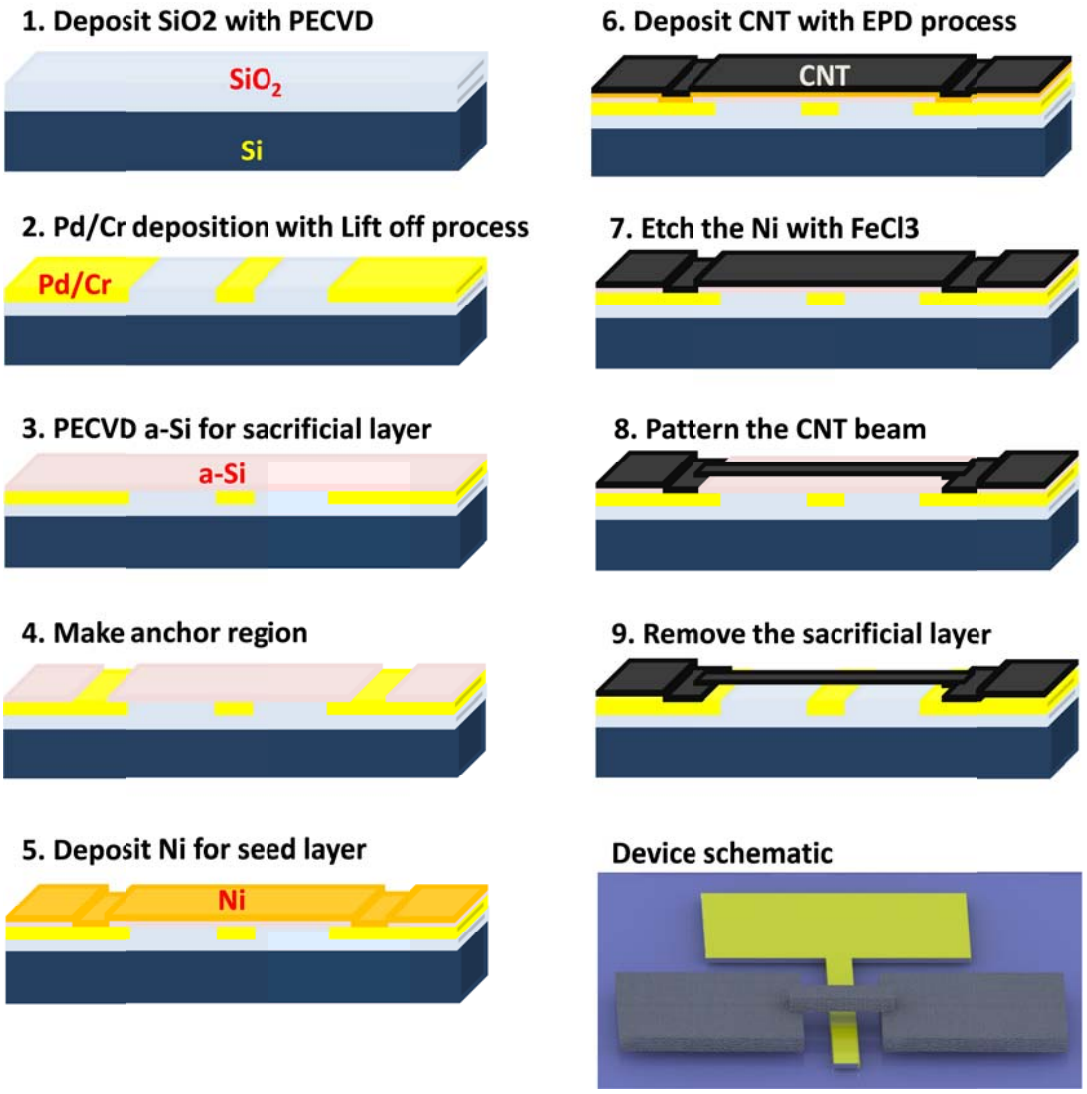

Figure 4.7 Schematic of overall fabrication process

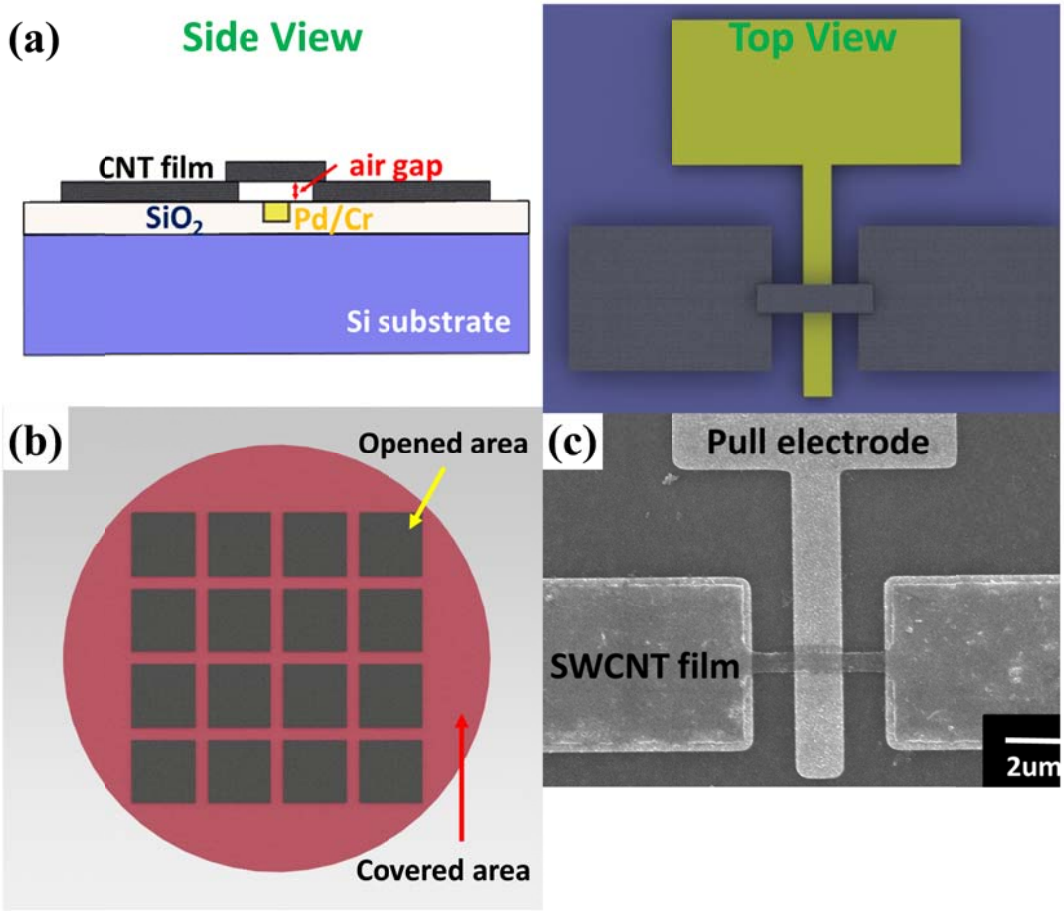

Figure 4.8 (a) Schematics of switch device: top and side view (b) Diagram for etching Ni under-layer (c) Fabricated two terminal switch; Reproduced from [3]

4.4. Device characterization and discussion

Figure 4.9 shows the I-V characteristics of a fabricated switch. The measured device has a SWCNT beam that is 100 nm thick, 1 μm wide and 3.45 μm long. The air gap is 30 nm. In the on-state the free-standing membrane is connected to the bottom electrode. This occurs when the pull-in electrode is biased to a value higher than the pull-

in voltage. In contrast, in the off-state the top membrane is not connected to the metal contact. During repeated switching events (up to 50 times), the device works with the similar performance. For voltages up to 3.2V the currents are a few pA. At this point the current rises rapidly with increasing electrode bias. We observe a four order of magnitude difference in the off and on-state currents.

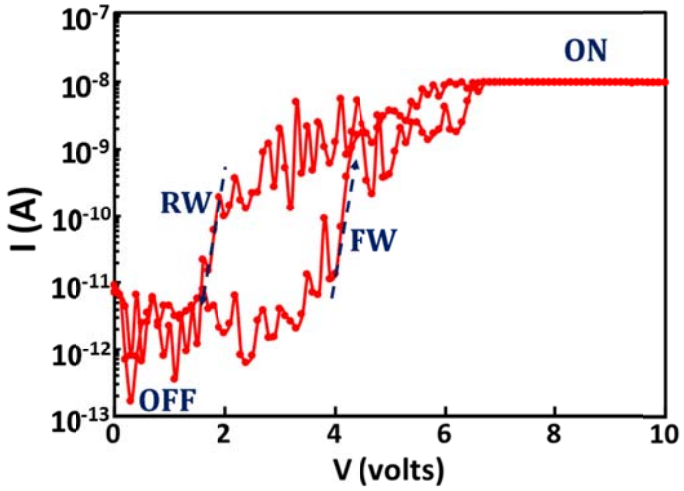

Figure 4.9 Schematic of I-V characteristics of device; Reproduced from [3]

The transition from the off-state to on-state is not abrupt. The slow turn-on is due to the high contact resistivity. There are four possible reasons for high contact resistivity. Firstly, only few CNTs may touch the bottom electrode right after pull-in voltage due to film roughness. SWCNT films deposited with an EPD method have a roughness of almost 20% of the film thickness as measured by AFM. The roughness on the bottom of the film after release is unknown, but could be comparable. Secondly, residual materials

generated during EPD process may impede current flow. Sodium dodecyl sulfate (SDS) surfactant is used to make the SWCNT suspension. It has a hydrophobic tail (blue) and hydrophilic head (red), as given Figure 2.4 (a). The SDS surfactants are adsorbed on the surface of the SWCNTs with cylindrical, hemimicellar, or random orientations as shown in Figure 2.4 (a), (b) and (c) respectively. Also, surfactants locate among the SWCNTs when the film is formed as shown in Figure 4.10. As a result, the film resistivity increases due to the surfactant effect. Thirdly, SWCNTs have either semiconducting or metallic behavior depending on chirality. Semiconducting SWCNTs may cause a higher film resistivity than metallic tubes. Finally, the contact area is extremely small and so the resistance is initially high.

There is hysteresis between the pull-in and pull-out voltages. This is common for an actuator. There are several possible reasons for hysteresis. The mechanical restoring force is linear in defection while the electrostatic force is quadratic. Thus, even in an ideal (i.e. no other forces) system the voltage required for pull-out will be less than that required for pull-in. In addition, short range forces can also contribute to hysteresis. Van der Waals and other short range surface forces are much stronger when the membrane is in the down position [22]. The effect of these forces must be balanced against the attractive electrostatic force and the mechanical restoring force. Generally the effect is more severe with smaller spring constant devices. The spring constant is proportional to the thickness, width and Young's modulus of the SWCNT films which are formed by EPD. The small spring constant of the free-standing SWCNT beam leads to a small pull-out voltage.

Hysteresis between increasing and decreasing operation voltage causes to a power consumption problem. Low actuation voltage is important for low power devices, because power is proportional to the square of actuation voltage. Hysteresis works like an offset, and the pull-in voltage is the sum of pull-out voltage and the offset. Thus, it imposes a limit on how small the pull-in voltage can be and still have a positive pull-out voltage.

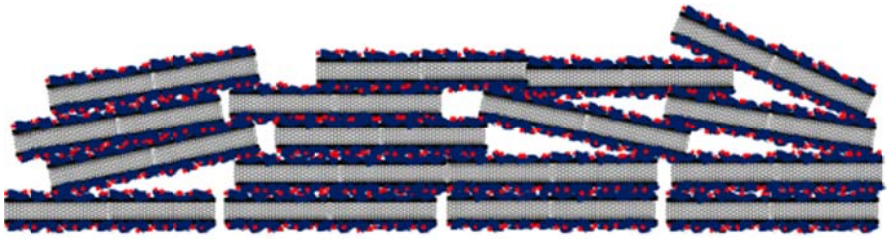

Figure 4.10 Schematic of packed SWCNTs with SDS surfactant

Figure 4.11 (a) shows I-V characteristic of another device operated over several cycles. The pull-in voltage varied upon cycling in agreement with reports of other CNT MEMS switches [184] [5] [7]. We suspect the source of this variation is the same effect that caused the gradual turn-on, the movement of individual bundles of CNTs in the air gap. These deflected bundles may not return to the perfectly same position during repeated cycles [186]. Moreover, the I-V characteristics of finished devices were measured in a conventional laboratory, so water vapor may also play a role in beam position variation during switching.

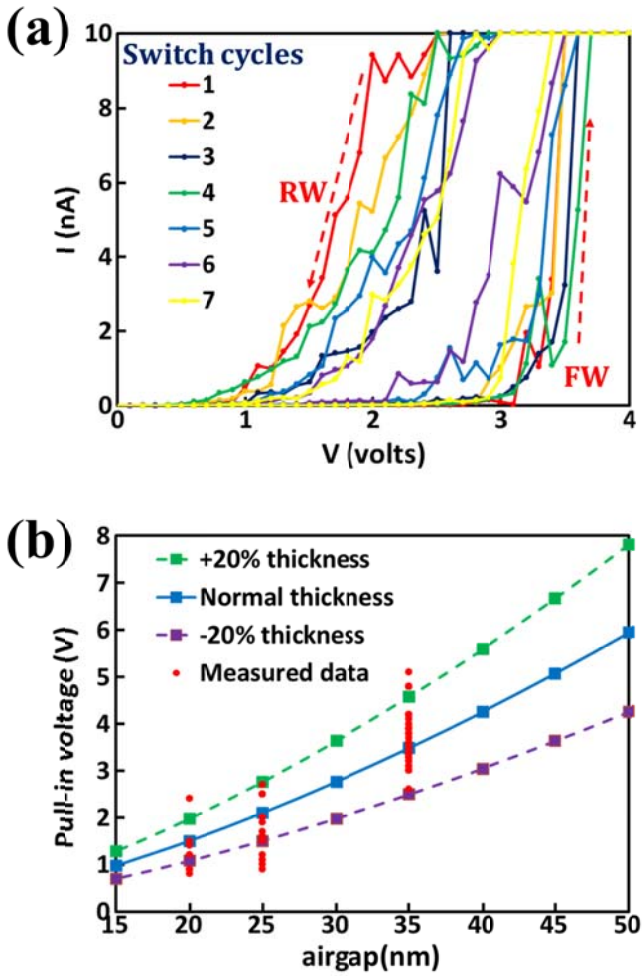

Figure 4.11 (a) I-V characteristics of device with several cycles (b) Plot of measured and calculated operation voltage (V_{PI}); Reproduced from [3]

Next, we calculate the device operation voltage to compare with the measured results and to confirm the accuracy of the Young's modulus measurements (Figure 4.11(b)). We fabricated devices with three different air-gaps: 20nm, 25nm and 35nm and measured the pull-in voltage. Red circles in graph express the measured result. The data

showed a range of values for the same nominal air gap. We calculated the pull in voltages of devices using Equation 4.18 [187, 188]. The SWCNT film thickness was measured by profilometry and AFM. Unsurprisingly, it showed a variation of almost 20% due in part to the roughness of the CNT film. To represent the effect of the thickness variation we calculated the pull-in voltage with 80nm, 100nm, and 120nm thick films. We observe that measured pull-in voltage were distributed around the nominal value for the larger gap, but tended to be somewhat lower than the nominal value for thinner gaps. We believed some SWCNT bundles, which are weakly bound in the film, deflect from the bottom of the film once the a-Si layer is removed. These nanotube whiskers pull-in at a lower voltage due to their smaller gap. This may suggest a small (~5 nm) but systematic reduction in the air gap. Causes could include the individual bundle movement described above or a small degree of zero-bias film deflection caused by stress effects in the released film.

Finally, we calculate the resonant frequency of device using

$$f_o = 1.0279\left(\frac{t}{l^2}\right)\sqrt{\frac{E}{\rho}} \tag{4.19}$$

where E, ρ, t, and l are, respectively, 5.7 GPa of Young's modulus from Chapter 3, 0.46 g/cm^3 of film density from Chapter 2, 100 nm of thickness, and 3.45 μm of beam length. Unfortunately, we cannot measure the resonance frequency results due to reliability issues. However, the calculated value is approximately 3.11 MHz at 100 nm thick SWCNT film. Representing the 20 % of film roughness as we mentioned before, the calculated frequency varied from 2.43 to 3.65 MHz depending on film thickness.

4.5. Problems of MEMS digital logic based on MEMS switches

MENS/NEMS switches that are fabricated with the CNT film turn-on much more slowly than semiconducting devices. When the MEMS switch is used as a digital logic element in a VLSI system, the gradual operation creates a large undetermined input region. Digital logic has two outputs: high '1' when $V_I > V_{IH}$ and low '0' when $V_I < V_{IL}$ as shown in Figure 4.12 (a). Gradual turn-on devices have an undefined area between V_{IH} and V_{IL}. The gradually increasing region causes noise margin issues, power consumption and propagation delays in a long logic chain.

To get a large noise margin, the output swing should be wider than the undetermined input region in multi-stage logic as shown in Figure 4.12 (b). Noise margins exist in two regions: 'high' and 'low'. The former occurs between V_{OH} of device 1 and V_{IH} of device 2. Likewise, the latter 'low' condition occurs between V_{IL} of device 1 and V_{OL} of device 2. Therefore, the output of device 1 has to swing sufficiently to correctly determine the logic state of the device 2. In other words, a low output of the first stage should be below the low input of the second stage, and the first stage of high output should be above the high input of the second stage.

In addition, the propagation delay causes dynamic transitions of the digital system. The mechanical delay particularly affects logic elements that require multiple transitions in a single clock cycle before the output settles to the correct result. For example, a NAND gate produces a 'high' when one of inputs is 'low' as depicted in Figure 4.13 (a). When

input I_1 is ‘high’ and input I_2 transitions from ‘low’ to ‘high’, the outputs Q_1, Q_2, Q_3 and Q_4 of four-stage NAND logics become ‘high’ or ‘low’ depending on the two input state

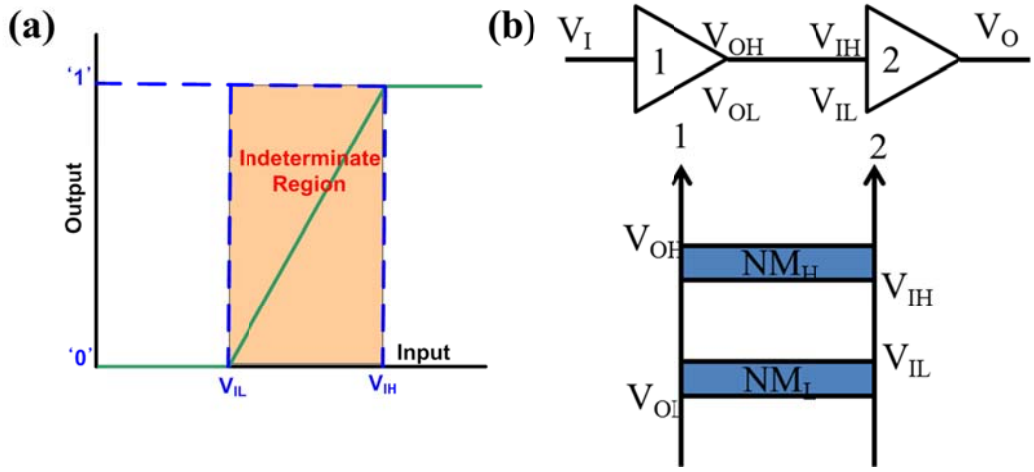

Figure 4.12 (a) Gradual turn-on device in digital logic (b) Noise margin of multi-stage logic

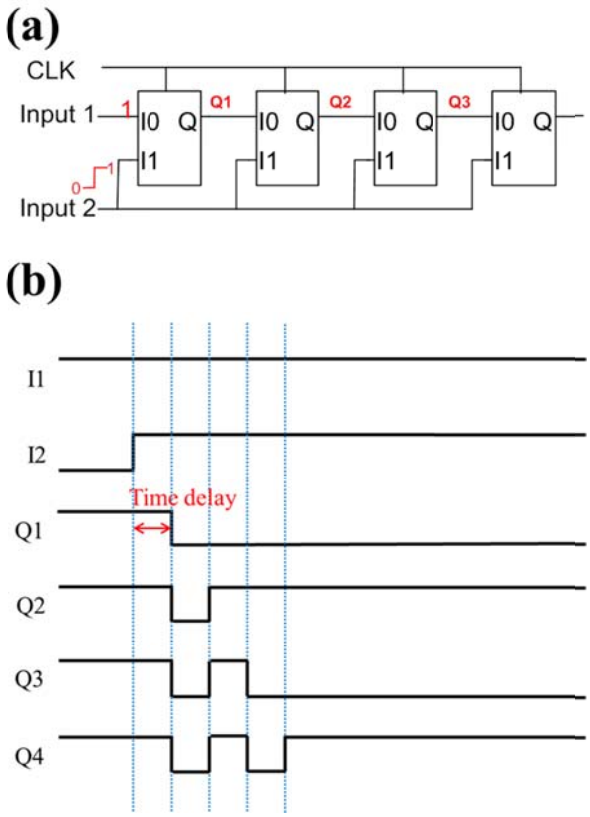

Figure 4.13 (a) Four stages of NAND logic with propagation delay (b) Timing diagram for dynamic transition

after a finite settling time as shown in Figure 4.13 (b). During this delay, some transition could occur in output Q_4 due to the wrong input. Moreover, this output glitch causes extra power consumption. Long chains of gates have higher dynamic transition power consumption than short chains [189].

4.6. Summary

In this chapter, electromechanical switch was fabricated and characterized. We produced several switches with different gaps using SWCNT films formed using the EPD

process. Pull-in voltages of device were found to be as low as 1 V by reducing the air-gap between the suspended beam and bottom electrodes. The measured device pull-in voltages were confirmed with the calculated data based on device geometry and beam characteristics. Moreover, we suggested that some reasons may contribute to gradual turn on, hysteresis in operation and the small discrepancy between the characterized and calculated pull-in voltages. Lastly, we found the resonant frequency to be approximately 2.4 to 3.5 MHz and discussed the implications of the device performance if it were implemented in digital logic applications.

Chapter 5.

Conclusions and Future Works

5.1. Conclusion

Power dissipation is a key issue of CMOS device scaling. MEMS/NEMS devices are a potential solution for standby power dissipation problems of CMOS device because of their almost ‘zero’ standby leakage. However, the MEMS/NEMS switch has an inherent tradeoff between pull-in voltage and switching speed. In other words, it is very challenging to achieve low power and high speed at the same time. To overcome this limit, nanoscale air-gap and low mass density materials are essential, because the former decreases the pull-in voltage and the latter increases the switching speed.

Single walled carbon nanotubes (SWCNTs) have low mass density and excellent electrical/mechanical properties. However, the synthesis techniques of carbon nanotubes are not compatible with a CMOS substrate due to their high temperature. Thus, continuous film deposition techniques of CNTs are suggested at low temperature (< 300 °C).

The electrophoretic deposition (EPD) at the room temperature allows the use of fabrication process including standard lithography and etch processes to produce patterns on a fully fabricated wafer. Moreover, the electrophoretically deposited SWCNT film

would be compatible with many other substrates because of the low deposition temperature.

First, we demonstrated the electrophoretic deposition of carbon nanotubes. A theoretical review of the EPD process and routes to stable suspensions including the surfactant were introduced. A detailed explanation of the electrophoretic deposition process was suggested. Experimental results showed single wall carbon nanotube films ranging from a few tens to hundreds of nm thick. The thickness depended on the deposition time and applied voltage. The experimental data showed a good agreement with the Hamaker and the exponential model if one assumes an initial offset value.

Next, the several properties of electrophoretically deposited SWCNT films were characterized. The density of the film was determined using the Rutherford backscattering spectroscopy. The mass density varied with the film thickness from 0.12 to 0.54 g/cm^3 depending on the deposited mass. Electrical and optical properties were characterized using HP 4156 and spectrometer with fabricated samples. The conductivity of the film was linearly proportional to the density and the transmittance decayed exponentially with density. The mechanical property of the film was measured with two techniques: straightforward properties of a film on a rigid substrate and by modelling the response of a suspended from to nanoindentation. For the latter method, we describe a technique for fabricating a free-standing film on pre-drilled substrate using a modified Langmuir–Blodgett method. Then we extracted the Young's modulus of the films using nonlinear model and measured load-displacement data by nanoindentation. The Young's

modulus was found to be between 4.72 and 5.67 GPa, independent of the film thickness. Also, some techniques to improve the released film properties were explored.

Finally, we fabricated two-terminal switches with a suspended SWCNT film deposited using the EPD process. Device pull-in voltages reached as low as 1 V by reducing the air-gap between the free-standing beam and bottom electrode. The characterized pull-in voltages were confirmed with the calculated data which used the extracted Young's modulus of SWCNT film and geometry of device. However, the devices have a gradual turn-on, a changing operation voltage with repeated switching, and a hysteresis problem during operation. We suggested some effects that may contribute to the above problems. Finally, we found the resonant frequency which is related to the device speed to be approximately 2.4 to 3.5 MHz.

5.2. Future work

Our ultimate goal is to demonstrate low pull in voltage (under 1V) and high frequency (over 1GHz) MEMS/NEMS switch using SWCNT films. However, we encountered many obstacles including deposited SWCNT film properties using EPD, gradual turn-on, hysteresis and reliability issues. Therefore, further work should be focused to improve the above problems.

First, the surfactants in the film should be removed to improve mechanical and electrical properties of the SWCNT films. A sodium dodecyl sulfate (SDS) surfactant was used to prepare stabilized SWCNT suspensions for electrophoretic deposition. After deposition, the adsorbed surfactants remained on the surface of CNTs. We believe that

these molecules degraded the mechanical and electrical properties of the characteristics of the films. The surfactant in the film can be removed after deposition through the use of an acid treatment and burn out [86, 88]. We reported improved resistivity of the film using an acid treatment, but there was no improvement in the Young's modulus of the film. We believe there are still remaining surfactants between the CNTs or the acid treatment degrades the CNT properties sufficiently to compensate for the surface cleaning. Therefore, research should be directed to ways to remove the surfactants completely after deposition. Alternatively, developing a new suspension without using surfactants can resolve the property degradation problem [36].

Second, preparing the suspension with only metallic SWCNTs may improve the electrical properties of the film and device performance, as well as the gradual turn-on problem which may be related to the higher resistivity of semiconducting SWCNTs. We used the mixed SWCNTs which contain under 5 % of metallic SWCNTs.

Third, released device should be kept in the vacuum condition to prevent moisture stiction problems, especially for devices with very small air gaps. Suspended SWCNT beams were collapsed within 24 hours after release process.

Finally, device reliability should be improved to measure the resonance frequency. Current devices only operated correctly for a few tens of cycles, so it was difficult to measure the operation speed with accuracy. Packaging the device and improving the mechanical properties of the beam are required to solve the issue.

Bibliography

[1] D. K. Schroder, *Semiconductor Material and Device Characterization*: Wiley, 2006.

[2] G. M. Rebeiz, *RF MEMS: Theory, Design, and Technology*: Wiley, 2004.

[3] S. A. C. Junyoung Lim, "Electromechanical Switches Fabricated by Electrophoretic Deposition of Single Wall Carbon Nanotube Films," *In processing,* 2015.

[4] P. Sarkar and P. S. Nicholson, "Electrophoretic Deposition (EPD): Mechanisms, Kinetics, and Application to Ceramics," *Journal of the American Ceramic Society,* vol. 79, pp. 1987-2002, 1996.

[5] A. B. Kaul, E. W. Wong, L. Epp, and B. D. Hunt, "Electromechanical Carbon Nanotube Switches for High-Frequency Applications," *Nano Letters,* vol. 6, pp. 942-947, 2006/05/01 2006.

[6] T. Rueckes, K. Kim, E. Joselevich, G. Y. Tseng, C.-L. Cheung, and C. M. Lieber, "Carbon Nanotube-Based Nonvolatile Random Access Memory for Molecular Computing," *Science,* vol. 289, pp. 94-97, July 7, 2000 2000.

[7] S. W. Lee, D. S. Lee, R. E. Morjan, S. H. Jhang, M. Sveningsson, O. A. Nerushev*, et al.*, "A Three-Terminal Carbon Nanorelay," *Nano Letters,* vol. 4, pp. 2027-2030, 2004/10/01 2004.

[8] J. Lim, M. Jalali, and S. A. Campbell, "Properties of electrophoretically deposited single wall carbon nanotube films," *Thin Solid Films,* vol. 589, pp. 278-285, 8/31/ 2015.

[9] J. Xue, T. Li, Y. Deng, and Z. Yu, "Full-chip leakage analysis for 65 nm CMOS technology and beyond," *Integration, the VLSI Journal,* vol. 43, pp. 353-364, 9// 2010.

[10] K. Yurekli, C. A. Mitchell, and R. Krishnamoorti, "Small-Angle Neutron Scattering from Surfactant-Assisted Aqueous Dispersions of Carbon Nanotubes," *Journal of the American Chemical Society,* vol. 126, pp. 9902-9903, 2004/08/01 2004.

[11] W. H. Duan, Q. Wang, and F. Collins, "Dispersion of carbon nanotubes with SDS surfactants: a study from a binding energy perspective," *Chemical Science,* vol. 2, pp. 1407-1413, 2011.

[12] D. Lee and T. Cui, "pH-dependent conductance behaviors of layer-by-layer self-assembled carboxylated carbon nanotube multilayer thin-film sensors," *Journal of Vacuum Science & Technology B,* vol. 27, pp. 842-848, 2009.

[13] S. N. Cha, J. E. Jang, Y. Choi, G. A. J. Amaratunga, D.-J. Kang, D. G. Hasko*, et al.*, "Fabrication of a nanoelectromechanical switch using a suspended carbon nanotube," *Applied Physics Letters,* vol. 86, p. 083105, 2005.

[14] M. Jung de Andrade, M. Dias Lima, V. Skákalová, C. Pérez Bergmann, and S. Roth, "Electrical properties of transparent carbon nanotube networks prepared through different techniques," *physica status solidi (RRL) – Rapid Research Letters,* vol. 1, pp. 178-180, 2007.

[15] M.-W. Jang, C.-L. Chen, W. E. Partlo, S. R. Patil, D. Lee, Z. Ye*, et al.*, "A pure single-walled carbon nanotube thin film based three-terminal microelectromechanical switch," *Applied Physics Letters,* vol. 98, p. 073502, 2011.

[16] A. Lambrecht and S. Reynaud, "Casimir force between metallic mirrors," *The European Physical Journal D,* vol. 8, pp. 309-318, 2000/07/01 2000.

[17] M. Kaempgen, G. S. Duesberg, and S. Roth, "Transparent carbon nanotube coatings," *Applied Surface Science,* vol. 252, pp. 425-429, 10/15/ 2005.

[18] M. T. Bohr, R. S. Chau, T. Ghani, and K. Mistry, "The High-k Solution," *Spectrum, IEEE,* vol. 44, pp. 29-35, 2007.

[19] H. Ananthan, A. Bansal, and K. Roy, "FinFET SRAM - device and circuit design considerations," in *Quality Electronic Design, 2004. Proceedings. 5th International Symposium on*, 2004, pp. 511-516.

[20] B. Swahn and S. Hassoun, "Gate sizing: finFETs vs 32nm bulk MOSFETs," in *Design Automation Conference, 2006 43rd ACM/IEEE*, 2006, pp. 528-531.

[21] E. R. Brown, "RF-MEMS switches for reconfigurable integrated circuits," *Microwave Theory and Techniques, IEEE Transactions on,* vol. 46, pp. 1868-1880, 1998.

[22] L. M. Jonsson, T. Nord, J. M. Kinaret, and S. Viefers, "Effects of surface forces and phonon dissipation in a three-terminal nanorelay," *Journal of Applied Physics,* vol. 96, pp. 629-635, 2004.

[23] S. Iijima, "Helical microtubules of graphitic carbon," *nature,* vol. 354, pp. 56-58, 1991.

[24] S. Iijima and T. Ichihashi, "Single-shell carbon nanotubes of 1-nm diameter," 1993.

[25] W. Maser, A. M. Benito, E. Muñoz, and M. T. Martínez, "Carbon nanotubes: From fundamental nanoscale objects towards functional nanocomposites and applications," in *Functionalized Nanoscale Materials, Devices and Systems*, ed: Springer, 2008, pp. 101-119.

[26] N. Saifuddin, A. Z. Raziah, and A. R. Junizah, "Carbon Nanotubes: A Review on Structure and Their Interaction with Proteins," *Journal of Chemistry,* vol. 2013, p. 18, 2013.

[27] C. Journet, W. Maser, P. Bernier, A. Loiseau, M. L. de La Chapelle, d. l. S. Lefrant*, et al.*, "Large-scale production of single-walled carbon nanotubes by the electric-arc technique," *nature,* vol. 388, pp. 756-758, 1997.

[28] T. W. Ebbesen and P. M. Ajayan, "Large-scale synthesis of carbon nanotubes," *Nature,* vol. 358, pp. 220-222, 07/16/print 1992.

[29] A. Thess, R. Lee, P. Nikolaev, H. Dai, P. Petit, J. Robert*, et al.*, "Crystalline ropes of metallic carbon nanotubes," *Science-AAAS-Weekly Paper Edition,* vol. 273, pp. 483-487, 1996.

[30] M. Su, B. Zheng, and J. Liu, "A scalable CVD method for the synthesis of single-walled carbon nanotubes with high catalyst productivity," *Chemical Physics Letters,* vol. 322, pp. 321-326, 2000.

[31] T.-J. Park, S. Banerjee, T. Hemraj-Benny, and S. S. Wong, "Purification strategies and purity visualization techniques for single-walled carbon nanotubes," *Journal of Materials Chemistry,* vol. 16, pp. 141-154, 2006.
[32] R. C. Haddon, J. Sippel, A. G. Rinzler, and F. Papadimitrakopoulos, "Purification and Separation of Carbon Nanotubes," *MRS Bulletin,* vol. 29, pp. 252-259, 2004.
[33] S. Bellucci, "Carbon nanotubes: physics and applications," *physica status solidi (c),* vol. 2, pp. 34-47, 2005.
[34] S. B. Sinnott and R. Andrews, "Carbon Nanotubes: Synthesis, Properties, and Applications," *Critical Reviews in Solid State and Materials Sciences,* vol. 26, pp. 145-249, 2001/07/01 2001.
[35] T. Dürkop, S. A. Getty, E. Cobas, and M. S. Fuhrer, "Extraordinary Mobility in Semiconducting Carbon Nanotubes," *Nano Letters,* vol. 4, pp. 35-39, 2004/01/01 2003.
[36] B. Q. Wei, R. Vajtai, and P. M. Ajayan, "Reliability and current carrying capacity of carbon nanotubes," *Applied Physics Letters,* vol. 79, pp. 1172-1174, 2001.
[37] H. G. Chae, Y. H. Choi, M. L. Minus, and S. Kumar, "Carbon nanotube reinforced small diameter polyacrylonitrile based carbon fiber," *Composites Science and Technology,* vol. 69, pp. 406-413, 2009.
[38] J. N. Coleman, U. Khan, W. J. Blau, and Y. K. Gun'ko, "Small but strong: a review of the mechanical properties of carbon nanotube–polymer composites," *Carbon,* vol. 44, pp. 1624-1652, 2006.
[39] J. Suhr, N. Koratkar, P. Keblinski, and P. Ajayan, "Viscoelasticity in carbon nanotube composites," *Nature Materials,* vol. 4, pp. 134-137, 2005.
[40] T.-W. Chou, L. Gao, E. T. Thostenson, Z. Zhang, and J.-H. Byun, "An assessment of the science and technology of carbon nanotube-based fibers and composites," *Composites Science and Technology,* vol. 70, pp. 1-19, 2010.
[41] S. De and J. N. Coleman, "The effects of percolation in nanostructured transparent conductors," *Mrs Bulletin,* vol. 36, pp. 774-781, 2011.
[42] Z. Wu, Z. Chen, X. Du, J. M. Logan, J. Sippel, M. Nikolou*, et al.*, "Transparent, Conductive Carbon Nanotube Films," *Science,* vol. 305, pp. 1273-1276, August 27, 2004 2004.
[43] Q. Cao, H.-s. Kim, N. Pimparkar, J. P. Kulkarni, C. Wang, M. Shim*, et al.*, "Medium-scale carbon nanotube thin-film integrated circuits on flexible plastic substrates," *Nature,* vol. 454, pp. 495-500, 2008.
[44] H. Park, A. Afzali, S.-J. Han, G. S. Tulevski, A. D. Franklin, J. Tersoff*, et al.*, "High-density integration of carbon nanotubes via chemical self-assembly," *Nature nanotechnology,* vol. 7, pp. 787-791, 2012.
[45] A. D. Franklin, M. Luisier, S.-J. Han, G. Tulevski, C. M. Breslin, L. Gignac*, et al.*, "Sub-10 nm carbon nanotube transistor," *Nano letters,* vol. 12, pp. 758-762, 2012.
[46] K. Jensen, J. Weldon, H. Garcia, and A. Zettl, "Nanotube radio," *Nano letters,* vol. 7, pp. 3508-3511, 2007.
[47] J. Appenzeller, Y.-M. Lin, J. Knoch, and P. Avouris, "Band-to-band tunneling in carbon nanotube field-effect transistors," *Physical Review Letters,* vol. 93, p. 196805, 2004.

[48] S. J. Tans, A. R. Verschueren, and C. Dekker, "Room-temperature transistor based on a single carbon nanotube," *Nature,* vol. 393, pp. 49-52, 1998.
[49] A. M. Ionescu and H. Riel, "Tunnel field-effect transistors as energy-efficient electronic switches," *Nature,* vol. 479, pp. 329-337, 2011.
[50] A. Izadi-Najafabadi, S. Yasuda, K. Kobashi, T. Yamada, D. N. Futaba, H. Hatori*, et al.*, "Extracting the Full Potential of Single-Walled Carbon Nanotubes as Durable Supercapacitor Electrodes Operable at 4 V with High Power and Energy Density," *Advanced Materials,* vol. 22, pp. E235-E241, 2010.
[51] C. Sotowa, G. Origi, M. Takeuchi, Y. Nishimura, K. Takeuchi, I. Y. Jang*, et al.*, "The Reinforcing Effect of Combined Carbon Nanotubes and Acetylene Blacks on the Positive Electrode of Lithium-Ion Batteries," *ChemSusChem,* vol. 1, pp. 911-915, 2008.
[52] A. R. Köhler, C. Som, A. Helland, and F. Gottschalk, "Studying the potential release of carbon nanotubes throughout the application life cycle," *Journal of Cleaner Production,* vol. 16, pp. 927-937, 2008.
[53] L. Dai, D. W. Chang, J. B. Baek, and W. Lu, "Carbon nanomaterials for advanced energy conversion and storage," *Small,* vol. 8, pp. 1130-1166, 2012.
[54] G. Gao and C. D. Vecitis, "Electrochemical carbon nanotube filter oxidative performance as a function of surface chemistry," *Environmental science & technology,* vol. 45, pp. 9726-9734, 2011.
[55] M. S. Rahaman, C. D. Vecitis, and M. Elimelech, "Electrochemical carbon-nanotube filter performance toward virus removal and inactivation in the presence of natural organic matter," *Environmental science & technology,* vol. 46, pp. 1556-1564, 2012.
[56] B. Corry, "Designing carbon nanotube membranes for efficient water desalination," *The Journal of Physical Chemistry B,* vol. 112, pp. 1427-1434, 2008.
[57] C. A. Poland, R. Duffin, I. Kinloch, A. Maynard, W. A. Wallace, A. Seaton*, et al.*, "Carbon nanotubes introduced into the abdominal cavity of mice show asbestos-like pathogenicity in a pilot study," *Nature nanotechnology,* vol. 3, pp. 423-428, 2008.
[58] A. Bianco, K. Kostarelos, and M. Prato, "Making carbon nanotubes biocompatible and biodegradable," *Chem. Commun.,* vol. 47, pp. 10182-10188, 2011.
[59] Z. Liu, X. Sun, N. Nakayama-Ratchford, and H. Dai, "Supramolecular chemistry on water-soluble carbon nanotubes for drug loading and delivery," *ACS nano,* vol. 1, pp. 50-56, 2007.
[60] D. A. Heller, H. Jin, B. M. Martinez, D. Patel, B. M. Miller, T.-K. Yeung*, et al.*, "Multimodal optical sensing and analyte specificity using single-walled carbon nanotubes," *Nature Nanotechnology,* vol. 4, pp. 114-120, 2009.
[61] T. Kurkina, A. Vlandas, A. Ahmad, K. Kern, and K. Balasubramanian, "Label-Free Detection of Few Copies of DNA with Carbon Nanotube Impedance Biosensors," *Angewandte Chemie International Edition,* vol. 50, pp. 3710-3714, 2011.

[62] H. Ko and V. V. Tsukruk, "Liquid-crystalline processing of highly oriented carbon nanotube arrays for thin-film transistors," *Nano letters,* vol. 6, pp. 1443-1448, 2006.
[63] C. Luo, X. Zuo, L. Wang, E. Wang, S. Song, J. Wang*, et al.*, "Flexible carbon nanotube− polymer composite films with high conductivity and superhydrophobicity made by solution process," *Nano letters,* vol. 8, pp. 4454-4458, 2008.
[64] T. Sreekumar, T. Liu, S. Kumar, L. M. Ericson, R. H. Hauge, and R. E. Smalley, "Single-wall carbon nanotube films," *Chemistry of Materials,* vol. 15, pp. 175-178, 2003.
[65] J. W. Jo, J. W. Jung, J. U. Lee, and W. H. Jo, "Fabrication of highly conductive and transparent thin films from single-walled carbon nanotubes using a new non-ionic surfactant via spin coating," *ACS nano,* vol. 4, pp. 5382-5388, 2010.
[66] M. C. LeMieux, S. Sok, M. E. Roberts, J. P. Opatkiewicz, D. Liu, S. N. Barman*, et al.*, "Solution assembly of organized carbon nanotube networks for thin-film transistors," *ACS nano,* vol. 3, pp. 4089-4097, 2009.
[67] J. E. Trancik, S. C. Barton, and J. Hone, "Transparent and catalytic carbon nanotube films," *Nano letters,* vol. 8, pp. 982-987, 2008.
[68] M. D. Lay, J. P. Novak, and E. S. Snow, "Simple route to large-scale ordered arrays of liquid-deposited carbon nanotubes," *Nano Letters,* vol. 4, pp. 603-606, 2004.
[69] B. Dan, G. C. Irvin, and M. Pasquali, "Continuous and scalable fabrication of transparent conducting carbon nanotube films," *ACS nano,* vol. 3, pp. 835-843, 2009.
[70] R. Iler, "Multilayers of colloidal particles," *Journal of Colloid and Interface Science,* vol. 21, pp. 569-594, 1966.
[71] J. Cho, K. Konopka, K. Rożniatowski, E. García-Lecina, M. S. P. Shaffer, and A. R. Boccaccini, "Characterisation of carbon nanotube films deposited by electrophoretic deposition," *Carbon,* vol. 47, pp. 58-67, 1// 2009.
[72] A. R. Boccaccini, J. Cho, J. A. Roether, B. J. C. Thomas, E. Jane Minay, and M. S. P. Shaffer, "Electrophoretic deposition of carbon nanotubes," *Carbon,* vol. 44, pp. 3149-3160, 12// 2006.
[73] M.-W. Jang, C.-L. Chen, W. E. Partlo, S. R. Patil, D. Lee, Z. Ye*, et al.*, "A pure single-walled carbon nanotube thin film based three-terminal microelectromechanical switch," *Applied Physics Letters,* vol. 98, pp. 073502-073502-3, 2011.
[74] L. Dongjin, Y. Zhijiang, S. A. Campbell, and T. Cui, "Suspended carbon nanotube thin film structures with high degree of alignment for NEMS switch applications," in *Solid-State Sensors, Actuators and Microsystems Conference (TRANSDUCERS), 2011 16th International*, 2011, pp. 625-628.
[75] A. Boccaccini, C. Kaya, and M. P. Shaffer, "Electrophoretic Deposition of Carbon Nanotubes (CNTs) and CNT/Nanoparticle Composites," in *Electrophoretic Deposition of Nanomaterials*, J. H. Dickerson and A. R. Boccaccini, Eds., ed: Springer New York, 2012, pp. 157-179.

[76] H. C. Hamaker, "Formation of a deposit by electrophoresis," *Transactions of the Faraday Society,* vol. 35, pp. 279-287, 1940.
[77] L. Besra and M. Liu, "A review on fundamentals and applications of electrophoretic deposition (EPD)," *Progress in materials science,* vol. 52, pp. 1-61, 2007.
[78] I. Corni, M. P. Ryan, and A. R. Boccaccini, "Electrophoretic deposition: From traditional ceramics to nanotechnology," *Journal of the European Ceramic Society,* vol. 28, pp. 1353-1367, // 2008.
[79] O. O. Van der Biest and L. J. Vandeperre, "ELECTROPHORETIC DEPOSITION OF MATERIALS," *Annual Review of Materials Science,* vol. 29, pp. 327-352, 1999.
[80] L. Besra, C. Compson, and M. Liu, "Electrophoretic Deposition of YSZ Particles on Non-Conducting Porous NiO–YSZ Substrates for Solid Oxide Fuel Cell Applications," *Journal of the American Ceramic Society,* vol. 89, pp. 3003-3009, 2006.
[81] G. Cao and Y. Wang, *Nanostructures and Nanomaterials: Synthesis, Properties, and Applications*: World Scientific, 2011.
[82] L. L. Schramm, *Emulsions, Foams, and Suspensions: Fundamentals and Applications*: Wiley, 2006.
[83] H. C. Hamaker and E. J. W. Verwey, "Part II.-(C) Colloid stability. The role of the forces between the particles in electrodeposition and other phenomena," *Transactions of the Faraday Society,* vol. 35, pp. 180-185, 1940.
[84] F. Grillon, D. Fayeulle, and M. Jeandin, "Quantitative image analysis of electrophoretic coatings," *Journal of Materials Science Letters,* vol. 11, pp. 272-275, 1992/01/01 1992.
[85] H. Koelmans and J. T. G. Overbeek, "Stability and electrophoretic deposition of suspensions in non-aqueous media," *Discussions of the Faraday Society,* vol. 18, pp. 52-63, 1954.
[86] J. Wang, X. Sun, X. Cai, Y. Lei, L. Song, and S. Xie, "Nonenzymatic Glucose Sensor Using Freestanding Single-Wall Carbon Nanotube Films," *Electrochemical and Solid-State Letters,* vol. 10, pp. J58-J60, May 1, 2007 2007.
[87] R. A. DiLeo, S. Frisco, M. J. Ganter, R. E. Rogers, R. P. Raffaelle, and B. J. Landi, "Hybrid Germanium Nanoparticle–Single-Wall Carbon Nanotube Free-Standing Anodes for Lithium Ion Batteries," *The Journal of Physical Chemistry C,* vol. 115, pp. 22609-22614, 2011/11/17 2011.
[88] Y. H. Kim, L. Müller-Meskamp, A. A. Zakhidov, C. Sachse, J. Meiss, J. Bikova, *et al.*, "Semi-transparent small molecule organic solar cells with laminated free-standing carbon nanotube top electrodes," *Solar Energy Materials and Solar Cells,* vol. 96, pp. 244-250, 1// 2012.
[89] R. Andrews, D. Jacques, D. Qian, and T. Rantell, "Multiwall Carbon Nanotubes: Synthesis and Application," *Accounts of Chemical Research,* vol. 35, pp. 1008-1017, 2002/12/01 2002.

[90] C. Singh, M. S. P. Shaffer, and A. H. Windle, "Production of controlled architectures of aligned carbon nanotubes by an injection chemical vapour deposition method," *Carbon,* vol. 41, pp. 359-368, 2// 2003.
[91] T. Guo, P. Nikolaev, A. Thess, D. T. Colbert, and R. E. Smalley, "Catalytic growth of single-walled manotubes by laser vaporization," *Chemical Physics Letters,* vol. 243, pp. 49-54, 9/8/ 1995.
[92] C. Du, J. Yeh, and N. Pan, "Carbon nanotube thin films with ordered structures," *Journal of Materials Chemistry,* vol. 15, pp. 548-550, 2005.
[93] C. Du, D. Heldbrant, and N. Pan, "Preparation and preliminary property study of carbon nanotubes films by electrophoretic deposition," *Materials Letters,* vol. 57, pp. 434-438, 12// 2002.
[94] S.-K. Kim and H. Lee, "Fabrication of patterned single-walled carbon nanotube films using electrophoretic deposition," *Ultramicroscopy,* vol. 108, pp. 1005-1008, 9// 2008.
[95] P. Songfeng, D. Jinhong, Z. You, L. Chang, and C. Hui-Ming, "The fabrication of a carbon nanotube transparent conductive film by electrophoretic deposition and hot-pressing transfer," *Nanotechnology,* vol. 20, p. 235707, 2009.
[96] S. M. Jung, J. Hahn, H. Y. Jung, and J. S. Suh, "Clean Carbon Nanotube Field Emitters Aligned Horizontally," *Nano Letters,* vol. 6, pp. 1569-1573, 2006/07/01 2006.
[97] M. D. Lima, M. J. de Andrade, C. P. Bergmann, and S. Roth, "Thin, conductive, carbon nanotube networks over transparent substrates by electrophoretic deposition," *Journal of Materials Chemistry,* vol. 18, pp. 776-779, 2008.
[98] J. L. Rigueur, S. A. Hasan, S. V. Mahajan, and J. H. Dickerson, "Buckypaper fabrication by liberation of electrophoretically deposited carbon nanotubes," *Carbon,* vol. 48, pp. 4090-4099, 11// 2010.
[99] B. J. C. Thomas, A. R. Boccaccini, and M. S. P. Shaffer, "Multi-Walled Carbon Nanotube Coatings Using Electrophoretic Deposition (EPD)," *Journal of the American Ceramic Society,* vol. 88, pp. 980-982, 2005.
[100] Y. Nakayama and S. Akita, "Field-emission device with carbon nanotubes for a flat panel display," *Synthetic Metals,* vol. 117, pp. 207-210, 2/15/ 2001.
[101] G. Girishkumar, M. Rettker, R. Underhile, D. Binz, K. Vinodgopal, P. McGinn*, et al.*, "Single-Wall Carbon Nanotube-Based Proton Exchange Membrane Assembly for Hydrogen Fuel Cells," *Langmuir,* vol. 21, pp. 8487-8494, 2005/08/01 2005.
[102] C. Du, D. Heldebrant, and N. Pan, "Preparation of carbon nanotubes composite sheet using electrophoretic deposition process," *Journal of Materials Science Letters,* vol. 21, pp. 565-568, 2002/04/01 2002.
[103] J. C. Bae, Y. J. Yoon, S.-J. Lee, and H. K. Baik, "Field emission properties of carbon nanotubes deposited by electrophoresis," *Physica B: Condensed Matter,* vol. 323, pp. 168-170, 10// 2002.
[104] D. A. Kurnosov, A. S. Baturin, A. S. Bugaev, K. N. Nikolski, R. G. Tchesov, and E. P. Sheshin, "Influence of the interelectrode distance in electrophoretic cold cathode fabrication on the emission uniformity," *Applied Surface Science,* vol. 215, pp. 232-236, 6/15/ 2003.

[105] H. Zhao, H. Song, Z. Li, G. Yuan, and Y. Jin, "Electrophoretic deposition and field emission properties of patterned carbon nanotubes," *Applied Surface Science,* vol. 251, pp. 242-244, 9/15/ 2005.
[106] Y. W. Jin, J. E. Jung, Y. J. Park, J. H. Choi, D. S. Jung, H. W. Lee*, et al.*, "Triode-type field emission array using carbon nanotubes and a conducting polymer composite prepared by electrochemical polymerization," *Journal of Applied Physics,* vol. 92, pp. 1065-1068, 2002.
[107] S. J. Oh, J. Zhang, Y. Cheng, H. Shimoda, and O. Zhou, "Liquid-phase fabrication of patterned carbon nanotube field emission cathodes," *Applied Physics Letters,* vol. 84, pp. 3738-3740, 2004.
[108] S. Barazzouk, S. Hotchandani, K. Vinodgopal, and P. V. Kamat, "Single-Wall Carbon Nanotube Films for Photocurrent Generation. A Prompt Response to Visible-Light Irradiation," *The Journal of Physical Chemistry B,* vol. 108, pp. 17015-17018, 2004/11/01 2004.
[109] P. V. Kamat, K. G. Thomas, S. Barazzouk, G. Girishkumar, K. Vinodgopal, and D. Meisel, "Self-Assembled Linear Bundles of Single Wall Carbon Nanotubes and Their Alignment and Deposition as a Film in a dc Field," *Journal of the American Chemical Society,* vol. 126, pp. 10757-10762, 2004/09/01 2004.
[110] H. Ma, L. Zhang, J. Zhang, L. Zhang, N. Yao, and B. Zhang, "Electron field emission properties of carbon nanotubes-deposited flexible film," *Applied Surface Science,* vol. 251, pp. 258-261, 9/15/ 2005.
[111] B. Gao, G. Z. Yue, Q. Qiu, Y. Cheng, H. Shimoda, L. Fleming*, et al.*, "Fabrication and Electron Field Emission Properties of Carbon Nanotube Films by Electrophoretic Deposition," *Advanced Materials,* vol. 13, pp. 1770-1773, 2001.
[112] W. B. Choi, Y. W. Jin, H. Y. Kim, S. J. Lee, M. J. Yun, J. H. Kang*, et al.*, "Electrophoresis deposition of carbon nanotubes for triode-type field emission display," *Applied Physics Letters,* vol. 78, pp. 1547-1549, 2001.
[113] C. Y. Lee, H. M. Tsai, H. J. Chuang, S. Y. Li, P. Lin, and T. Y. Tseng, "Characteristics and Electrochemical Performance of Supercapacitors with Manganese Oxide-Carbon Nanotube Nanocomposite Electrodes," *Journal of The Electrochemical Society,* vol. 152, pp. A716-A720, April 1, 2005 2005.
[114] M. S. P. Shaffer, X. Fan, and A. H. Windle, "Dispersion and packing of carbon nanotubes," *Carbon,* vol. 36, pp. 1603-1612, 11// 1998.
[115] Z. Sun, V. Nicolosi, D. Rickard, S. D. Bergin, D. Aherne, and J. N. Coleman, "Quantitative Evaluation of Surfactant-stabilized Single-walled Carbon Nanotubes: Dispersion Quality and Its Correlation with Zeta Potential," *The Journal of Physical Chemistry C,* vol. 112, pp. 10692-10699, 2008/07/01 2008.
[116] H. Wang, "Dispersing carbon nanotubes using surfactants," *Current Opinion in Colloid & Interface Science,* vol. 14, pp. 364-371, 10// 2009.
[117] M. J. O'Connell, S. M. Bachilo, C. B. Huffman, V. C. Moore, M. S. Strano, E. H. Haroz*, et al.*, "Band Gap Fluorescence from Individual Single-Walled Carbon Nanotubes," *Science,* vol. 297, pp. 593-596, July 26, 2002 2002.

[118] M. S. Amer, *Raman Spectroscopy, Fullerenes and Nanotechnology*: Royal Society of Chemistry, 2010.
[119] Q. Zhang, *Carbon Nanotubes and Their Applications*: Pan Stanford, 2012.
[120] Wang, H. Shan, R. H. Hauge, M. Pasquali, and R. E. Smalley, "A Highly Selective, One-Pot Purification Method for Single-Walled Carbon Nanotubes," *The Journal of Physical Chemistry B,* vol. 111, pp. 1249-1252, 2007/02/01 2007.
[121] C. Y. Liao and J. K. Wu, "Chemical machining of nickel in ferric chloride solution," *Journal of Materials Science Letters,* vol. 11, pp. 689-691, 1992/01/01 1992.
[122] F. Bouyer and A. Foissy, "Electrophoretic Deposition of Silicon Carbide," *Journal of the American Ceramic Society,* vol. 82, pp. 2001-2010, 1999.
[123] M. Ammam, "Electrophoretic deposition under modulated electric fields: a review," *RSC Advances,* vol. 2, pp. 7633-7646, 2012.
[124] I. Chowdhury, M. C. Duch, C. C. Gits, M. C. Hersam, and S. L. Walker, "Impact of Synthesis Methods on the Transport of Single Walled Carbon Nanotubes in the Aquatic Environment," *Environmental Science & Technology,* vol. 46, pp. 11752-11760, 2012/11/06 2012.
[125] C. Liu, *Foundations of MEMS*: Prentice Hall Press, 2011.
[126] G. Boudreault, C. Jeynes, E. Wendler, A. Nejim, R. P. Webb, and U. Wätjen, "Accurate RBS measurement of ion implant doses in silicon," *Surface and Interface Analysis,* vol. 33, pp. 478-486, 2002.
[127] W. S. R. Nass, H. Schmidt, "Electrophoretic deposition of alumina from non-aqueous dispersions," *Ceram. Powder Process. Sci.: Proc. Second Int. Confer,* pp. 625-632, 1988.
[128] X. Lu and Z. Chen, "Curved Pi-Conjugation, Aromaticity, and the Related Chemistry of Small Fullerenes (<C60) and Single-Walled Carbon Nanotubes," *Chemical Reviews,* vol. 105, pp. 3643-3696, 2005/10/01 2005.
[129] S. Hong and S. Myung, "Nanotube Electronics: A flexible approach to mobility," *Nat Nano,* vol. 2, pp. 207-208, 04//print 2007.
[130] H. Xu, L. Chen, L. Hu, and N. Zhitenev, "Contact resistance of flexible, transparent carbon nanotube films with metals," *Applied Physics Letters,* vol. 97, pp. -, 2010.
[131] A. D. Pasquier, H. E. Unalan, A. Kanwal, S. Miller, and M. Chhowalla, "Conducting and transparent single-wall carbon nanotube electrodes for polymer-fullerene solar cells," *Applied Physics Letters,* vol. 87, pp. -, 2005.
[132] B. Ashrafi, K. Das, R. Le Faive, P. Hubert, and S. Vengallatore, "Measuring the Elastic Properties of Freestanding Thick Films Using a Nanoindenter-Based Bending Test," *Experimental Mechanics,* vol. 52, pp. 371-378, 2012/04/01 2012.
[133] A. C. Fischer-Cripps, *Nanoindentation*: Springer, 2011.
[134] M. Wang, K. M. Liechti, J. M. White, and R. M. Winter, "Nanoindentation of polymeric thin films with an interfacial force microscope," *Journal of the Mechanics and Physics of Solids,* vol. 52, pp. 2329-2354, 10// 2004.

[135] L. Vaisman, H. D. Wagner, and G. Marom, "The role of surfactants in dispersion of carbon nanotubes," *Advances in Colloid and Interface Science,* vol. 128–130, pp. 37-46, 12/21/ 2006.
[136] Y. H. Yang and W. Z. Li, "Radial elasticity of single-walled carbon nanotube measured by atomic force microscopy," *Applied Physics Letters,* vol. 98, p. 041901, 2011.
[137] E. F. Morgan, H. H. Bayraktar, and T. M. Keaveny, "Trabecular bone modulus–density relationships depend on anatomic site," *Journal of Biomechanics,* vol. 36, pp. 897-904, 7// 2003.
[138] M. D. A. Sayeed, Y. H. Kim, Y. Park, A. I. Gopalan, K.-P. Lee, and S.-J. Choi, "Non-Covalent Bonding Interaction of Surfactants with Functionalized Carbon Nanotubes in Proton Exchange Membranes for Fuel Cell Applications," *Journal of Nanoscience and Nanotechnology,* vol. 13, pp. 7424-7429, // 2013.
[139] H. D. Espinosa, B. C. Prorok, and M. Fischer, "A methodology for determining mechanical properties of freestanding thin films and MEMS materials," *Journal of the Mechanics and Physics of Solids,* vol. 51, pp. 47-67, 1// 2003.
[140] S. Timoshenko and S. Woinowsky-Krieger, *Theory of plates and shells*: McGraw-Hill, 1959.
[141] K. M. Mushtari and K. Z. Galimov, *Non-linear theory of thin elastic shells*: Academy of Sciences, U.S.S.R. Kazan' Branch, 1957.
[142] U. Komaragiri, M. R. Begley, and J. G. Simmonds, "The Mechanical Response of Freestanding Circular Elastic Films Under Point and Pressure Loads," *Journal of Applied Mechanics,* vol. 72, pp. 203-212, 2005.
[143] S. Hong, T. P. Weihs, J. C. Bravman, and W. D. Nix, "Measuring stiffnesses and residual stresses of silicon nitride thin films," *Journal of Electronic Materials,* vol. 19, pp. 903-909, 1990/09/01 1990.
[144] K.-T. Wan, S. Guo, and D. A. Dillard, "A theoretical and numerical study of a thin clamped circular film under an external load in the presence of a tensile residual stress," *Thin Solid Films,* vol. 425, pp. 150-162, 2/3/ 2003.
[145] B. F. Ju, K.-K. Liu, S.-F. Ling, and W. Hong Ng, "A novel technique for characterizing elastic properties of thin biological membrane," *Mechanics of Materials,* vol. 34, pp. 749-754, 11// 2002.
[146] O. R. Shojaei and A. Karimi, "Comparison of mechanical properties of TiN thin films using nanoindentation and bulge test," *Thin Solid Films,* vol. 332, pp. 202-208, 11/2/ 1998.
[147] A. Karimi, O. R. Shojaei, T. Kruml, and J. L. Martin, "Characterisation of TiN thin films using the bulge test and the nanoindentation technique," *Thin Solid Films,* vol. 308–309, pp. 334-339, 10/31/ 1997.
[148] J. P. Frakes and J. G. Simmonds, "Asymptotic Solutions of the Von Karman Equations for a Circular Plate Under a Concentrated Load," *Journal of Applied Mechanics,* vol. 52, pp. 326-330, 1985.
[149] C. Poilane, P. Delobelle, C. Lexcellent, S. Hayashi, and H. Tobushi, "Analysis of the mechanical behavior of shape memory polymer membranes by

nanoindentation, bulging and point membrane deflection tests," *Thin Solid Films,* vol. 379, pp. 156-165, 12/8/ 2000.
[150] E. Schwerin, "Über Spannungen und Formänderungen kreisringförmiger Membranen," *ZAMM - Journal of Applied Mathematics and Mechanics / Zeitschrift für Angewandte Mathematik und Mechanik,* vol. 9, pp. 482-483, 1929.
[151] T. Tsakalakos, "The bulge test: A comparison of the theory and experiment for isotropic and anisotropic films," *Thin Solid Films,* vol. 75, pp. 293-305, 1/16/ 1981.
[152] Y. Von Kaenel, J. C. Giachetto, J. Stiegler, J. M. Drezet, and E. Blank, "A new interpretation of bulge test measurements using numerical simulation," *Diamond and Related Materials,* vol. 5, pp. 635-639, 5// 1996.
[153] M. Sheploak and J. Dugundji, "Large Deflections of Clamped Circular Plates Under Initial Tension and Transitions to Membrane Behavior," *Journal of Applied Mechanics,* vol. 65, pp. 107-115, 1998.
[154] J. A. Voorthuyzen and P. Bergveld, "The influence of tensile forces on the deflection of circular diaphragms in pressure sensors," *Sensors and Actuators,* vol. 6, pp. 201-213, 11// 1984.
[155] M. Ahmed and M. S. J. Hashmi, "Finite-element analysis of bulge forming applying pressure and in-plane compressive load," *Journal of Materials Processing Technology,* vol. 77, pp. 95-102, 5/1/ 1998.
[156] M. K. Small and W. D. Nix, "Analysis of the accuracy of the bulge test in determining the mechanical properties of thin films," *Journal of Materials Research,* vol. 7, pp. 1553-1563, 1992.
[157] J. J. Vlassak and W. D. Nix, "A new bulge test technique for the determination of Young's modulus and Poisson's ratio of thin films," *Journal of Materials Research,* vol. 7, pp. 3242-3249, 1992.
[158] O. Tabata, K. Kawahata, S. Sugiyama, and I. Igarashi, "Mechanical property measurements of thin films using load-deflection of composite rectangular membranes," *Sensors and Actuators,* vol. 20, pp. 135-141, 11/15/ 1989.
[159] V. Ziebart, O. Paul, U. Munch, J. Schwizer, and H. Baltes, "Mechanical properties of thin films from the load deflection of long clamped plates," *Microelectromechanical Systems, Journal of,* vol. 7, pp. 320-328, 1998.
[160] J. Yang and O. Paul, "Fracture properties of LPCVD silicon nitride thin films from the load–deflection of long membranes," *Sensors and Actuators A: Physical,* vol. 97–98, pp. 520-526, 4/1/ 2002.
[161] S. Jayaraman, R. L. Edwards, and K. J. Hemker, "Relating mechanical testing and microstructural features of polysilicon thin films," *Journal of Materials Research,* vol. 14, pp. 688-697, 1999.
[162] E. Bonnotte, P. Delobelle, L. Bornier, B. Trolard, and G. Tribillon, "Two interferometric methods for the mechanical characterization of thin films by bulging tests. Application to single crystal of silicon," *Journal of Materials Research,* vol. 12, pp. 2234-2248, 1997.

[163] Z. C. Leseman and U. o. I. a. Urbana-Champaign, *A Novel Method for Testing Freestanding Nanofilms Using a Custom MEMS Load Cell*: University of Illinois at Urbana-Champaign, 2006.
[164] K. C. Maner, M. R. Begley, and W. C. Oliver, "Nanomechanical testing of circular freestanding polymer films with sub-micron thickness," *Acta Materialia,* vol. 52, pp. 5451-5460, 11/8/ 2004.
[165] E. T. Mickelson, C. B. Huffman, A. G. Rinzler, R. E. Smalley, R. H. Hauge, and J. L. Margrave, "Fluorination of single-wall carbon nanotubes," *Chemical Physics Letters,* vol. 296, pp. 188-194, 10/30/ 1998.
[166] B. Scheibe, M. Rümmeli, E. Borowiak-Palen, and R. Kalenczuk, "Separation of surfactant functionalized single-walled carbon nanotubes via free solution electrophoresis method," *Central European Journal of Physics,* vol. 9, pp. 325-329, 2011/04/01 2011.
[167] B.-M. Wang, Z. Yuan, Z.-Q. Guo, H.-N. Ma, and C. Lai, "Controlling the optimum surfactants concentrations for dispersing carbon nanofibers in aqueous solution," *Russian Journal of Physical Chemistry A,* vol. 87, pp. 2253-2259, 2013/12/01 2013.
[168] F. Reiter, "Carbon based nanomaterials as transparent conductive electrodes," *Georgia Institute of Technology,* 2011.
[169] S. Chakraborty, A. Bhattacharya, and T. K. Bhattacharyya, "Experimental analysis of pull-out voltage of electrostatically actuated microcantilever beam based on contact-stiction model," *Micro & Nano Letters, IET,* vol. 6, pp. 43-47, 2011.
[170] W. M. v. Spengen, P. Robert, and W. Ingrid De, "A physical model to predict stiction in MEMS," *Journal of Micromechanics and Microengineering,* vol. 12, p. 702, 2002.
[171] T. Niels, S. Tonny, J. Henri, L. Rob, and E. Miko, "Stiction in surface micromachining," *Journal of Micromechanics and Microengineering,* vol. 6, p. 385, 1996.
[172] H. B. G. Casimir, "On the Attraction Between Two Perfectly Conducting Plates," *Indag.Math.,* vol. 10, pp. 261-263, 1948.
[173] E. Elizalde and A. Romeo, "Essentials of the Casimir effect and its computation," *American Journal of Physics,* vol. 59, pp. 711-719, 1991.
[174] P. W. Milonni and M.-L. Shih, "Casimir forces," *Contemporary Physics,* vol. 33, pp. 313-322, 1992/09/01 1992.
[175] L. Spruch, "Long-Range (Casimir) Interactions," *Science,* vol. 272, pp. 1452-1455, June 7, 1996 1996.
[176] M. Schaden and L. Spruch, "Focusing Virtual Photons: Casimir Energies for Some Pairs of Conductors," *Physical Review Letters,* vol. 84, pp. 459-462, 01/17/ 2000.
[177] S. K. Lamoreaux, "Demonstration of the Casimir Force in the 0.6 to $6\ensuremath{\mu}m$ Range," *Physical Review Letters,* vol. 78, pp. 5-8, 01/06/ 1997.

[178] J. Błocki, J. Randrup, W. J. Świątecki, and C. F. Tsang, "Proximity forces," *Annals of Physics,* vol. 105, pp. 427-462, 6// 1977.
[179] E. D. Palik, *Handbook of Optical Constants of Solids*: Elsevier Science, 1998.
[180] E. M. Lifshitz, "THE THEORY OF MOLECULAR ATTRACTIVE FORCES BETWEEN SOLIDS," *Journal Name: Soviet Phys. JETP; Journal Volume: Vol: 2; Other Information: Zhur. Eksptl.' i Teoret. Fiz. 29, 94-110(1955) July. (In Russian). Orig. Receipt Date: 31-DEC-56,* pp. Medium: X; Size: Pages: 73-83, 1956.
[181] K. L. Steven, "The Casimir force: background, experiments, and applications," *Reports on Progress in Physics,* vol. 68, p. 201, 2005.
[182] C. Hamaguchi, *Basic Semiconductor Physics*: Springer Berlin Heidelberg, 2009.
[183] C. Liu, *Foundations of MEMS*: Pearson Prentice Hall, 2006.
[184] M.-W. Jang, C.-L. Chen, W. E. Partlo, S. R. Patil, D. Lee, Z. Ye*, et al.*, "A pure single-walled carbon nanotube thin film based three-terminal microelectromechanical switch," *Applied Physics Letters,* vol. 98, pp. -, 2011.
[185] A. Javey, J. Guo, Q. Wang, M. Lundstrom, and H. Dai, "Ballistic carbon nanotube field-effect transistors," *Nature,* vol. 424, pp. 654-657, 08/07/print 2003.
[186] V. T. Srikar and S. M. Spearing, "Materials selection for microfabricated electrostatic actuators," *Sensors and Actuators A: Physical,* vol. 102, pp. 279-285, 1/1/ 2003.
[187] D. Marc, S. V. Rotkin, and N. R. Aluru, "Calculation of pull-in voltages for carbon-nanotube-based nanoelectromechanical switches," *Nanotechnology,* vol. 13, p. 120, 2002.
[188] G. M. Rebeiz, *RF MEMS: Theory, Design, and Technology*: John Wiley \& Sons, Inc., 2003.
[189] J. M. Rabaey, A. P. Chandrakasan, and B. Nikolić, *Digital Integrated Circuits, 2/e*: Pearson Education, 2003.